2010-02-15

# Optical Depolarization from Turbulent Convective Flow: A Laboratory Study

Sarah F. Woods
*University of Miami*, swoods@rsmas.miami.edu

UNIVERSITY OF MIAMI

# OPTICAL DEPOLARIZATION FROM TURBULENT CONVECTIVE FLOW: A LABORATORY STUDY

By

Sarah F. Woods

A DISSERTATION

Submitted to the Faculty
of the University of Miami
in partial fulfillment of the requirements for
the degree of Doctor of Philosophy

Coral Gables, Florida

May 2010

UNIVERSITY OF MIAMI

A dissertation submitted in partial fulfillment of
the requirements for the degree of
Doctor of Philosophy

# OPTICAL DEPOLARIZATION FROM TURBULENT CONVECTIVE FLOW: A LABORATORY STUDY

Sarah F. Woods

Approved:

| | |
|---|---|
| _____ | _____ |
| Darek J. Bogucki, Ph.D.<br>Professor of Applied Marine Physics | Terri A. Scandura, Ph.D.<br>Dean of the Graduate School |
| _____ | _____ |
| William M. Drennan, Ph.D.<br>Professor of Applied Marine Physics | Brian K. Haus, Ph.D.<br>Associate Professor of Applied Marine Physics |
| _____ | _____ |
| Peter J. Minnett, Ph.D.<br>Professor of Meteorology and Physical Oceanography | Kenneth J. Voss, Ph.D.<br>Professor of Physics |

WOODS, SARAH (Ph.D., Applied Marine Physics)
Optical Depolarization from (May 2010)
Turbulent Convective Flow: a Laboratory Study

Abstract of a dissertation at the University of Miami.

Dissertation supervised by Professor Darek Bogucki.
No. of pages in text. (87)

In an effort to investigate the role of turbulence in near-forward scattering, laboratory measurements of scattering on turbulent flow were carried out in a Rayleigh-Bénard convective tank. Particle Image Velocimetry and profiling thermistor temperature measurements are used to characterize the turbulent flow through determination of the large scale flow features, turbulent kinetic energy dissipation rates, and thermal dissipation rates. Polarized diffractometer measurements allow for determination of the turbulence-induced depolarization rate, which is comparable to that observed with polarimetric lidar. Measurements were made over a range of turbulent strengths, with Rayleigh number between $10^8$ and $3*10^9$, and with turbulent parameters corresponding to those characteristic of the oceanic mixed layer. Results show that the turbulence-induced depolarization rate is indirectly proportional to the strength of the turbulent flow, suggesting that light beam depolarization from turbulent flow may contain useful information regarding the smallest length scales of turbulent flow.

**Acknowledgements**

I would like to thank my advisor, Dr. Darek Bogucki for his guidance and support during my tenure at the University of Miami. I would also like to thank my additional committee members, Drs. William Drennan, Peter Minnett, Brian Haus, and Kenneth Voss, for their support, commitment, and guidance, not only in relation to my dissertation work, but also in relation to ongoing research projects to which they provided me ample opportunity for participation and contribution. I am also indebted to Tom Snowdon, Wlodzimierz Freda, and many additional fellow students, professors, and staff of the Rosenstiel School of Marine and Atmospheric Science, particularly to those of the divisions of Applied Marine Physics and Meteorology and Physical Oceanography, as well as many family members and friends for their support and encouragement. I would also like to acknowledge that this work was supported by ONR and NASA.

This work is dedicated to my loving and devoted family, Harry, Rose Marie, Matthew, Zachary, and Jacob Woods, and also to Tufan Aydogdu, for their never-ending love, support, and encouragement.

**TABLE OF CONTENTS**

**List of Figures**

**List of Abbreviations and Symbols**

| | |
|---|---|
| $\alpha$ | Light beam attenuation |
| $\alpha_T$ | Thermal expansion coefficient of water at 20 $^{o}$C ~ 2.1*10$^{-4}$ $^{o}$C$^{-1}$ |
| $\beta(\theta)$ | Volume Scattering Function |
| $\gamma$ | Depolarization rate |
| $\Delta T$ | Temperature difference across Rayleigh-Bénard convective tank |
| $\varepsilon$ | Turbulent kinetic energy dissipation (TKED) rate |
| $\eta_B$ | Batchelor length scale |
| $\kappa$ | Thermal conductivity of water at 20 $^{o}$C ~ 0.58 Wm$^{-1}$$^{o}$C$^{-1}$ |
| $\nu$ | Kinematic viscosity of water at 20 $^{o}$C ~ 1.005*10$^{-6}$ m$^{2}$s$^{-1}$ |
| $\chi_\theta$ | Turbulent thermal dissipation (TD) rate |
| $A$ | Constant ~ 1.6 |
| $b$ | Total scattering coefficient |
| $B$ | Constant ~ 1.6 |
| CCD | Charge Coupled Device |
| $d$ | Depth of Rayleigh-Bénard convective tank |
| $dI(\theta)$ | Scattered radiant intensity |

| | |
|---|---|
| $dv$ | Scattering unit volume |
| $D_T$ | Thermal diffusivity of water at 20 $^oC \sim 1.42*10^{-7}$ $m^2s^{-1}$ |
| $E_\theta(k)$ | Measured one-dimensional thermal gradient spectrum |
| $E_o$ | Incident irradiance |
| $g$ | Gravitational constant ~ 9.8 $ms^{-2}$ |
| $k$ | Wavenumber |
| $k_B$ | Batchelor wavenumber |
| $k_L$ | Lowest wavenumber used in fitting Batchelor spectra |
| $k_N$ | Highest wavenumber used in fitting Batchelor spectra |
| $K$ | Non-dimensional wavenumber |
| $L$ | Integral length scale |
| $Nu$ | Nusselt number |
| $P_C$ | Power in co-polarized state of light beam |
| $P_{CO}$ | Initial power in co-polarized state of light beam |
| PIV | Particle Image Velocimetry |
| $Pr$ | Prandtl Number |
| $P_X$ | Power in orthogonally polarized state of light beam |

| | |
|---|---|
| $P_{XO}$ | Initial power in orthogonally polarized state of light beam |
| $q$ | Constant ~ $2(3^{1/2})$ |
| $Ra$ | Rayleigh number |
| $S(k)$ | One-dimensional Batchelor spectrum |
| $S_N(\alpha)$ | Normalized one-dimensional Batchelor spectrum |
| $T$ | Temperature |
| TD | Turbulent thermal dissipation rate |
| TKED | Turbulent kinetic energy dissipation rate |
| VSF | Volume Scattering Function |

# Chapter 1: Introduction

## 1.1 Introduction and Motivation

### *1.1.1 Oceanic Turbulence*

Turbulence is far more common in nature than most would realize. To name a few examples, turbulent flow is found in the earth's atmospheric boundary layer, jet streams, cumulous clouds, the photosphere of the sun and similar stars, smoke stack plumes, air flow around ships, airplanes, and automobiles, in rivers, and in oceanic flows (Tennekes and Lumley 1972). What makes all of these flows turbulent? Since it is difficult to give a formal definition of turbulence, the common practice is to list its characterizing attributes. Turbulent flow is characterized by irregularity, diffusivity, vorticity, and dissipation (Tennekes and Lumley 1972, Kundu and Cohen 1987). The irregularity is essentially the randomness of the flow. Diffusivity is the mechanism for spreading velocity fluctuations through the flow, or increased rates of mixing, momentum, heat, and mass transfer. Turbulence is characterized by high fluctuations in vorticity, which is the three-dimensional rotational nature of the flow. This three-dimensional rotational nature is associated with eddies of varying sizes within the flow. The largest contain most of the energy of the flow and have a size on the order of the width of the flow. The energy contained in the largest eddies cascades down into smaller eddies through nonlinear interactions. In the smallest eddies, the energy is finally dissipated by viscous forces. Dissipation is the deformation work performed by viscous shear stresses that cascades energy and vorticity to the smaller scales of the flow. Turbulence, by its very nature, is difficult to characterize and predict, as observations are

sparse and turbulence theory remains one of the last major unsolved problems in classical physics.

In the ocean, turbulence plays an important role in processes near the surface, such as air-sea gas transfer, distribution and mixing of nutrients, resuspension of sediment in shallow waters, and light propagation. Thus, characterization and understanding of turbulence is important to those studying the air-sea interface, near surface ocean processes, the coastal ocean, and optical oceanography. Most investigations of oceanic turbulence are conducted through observation of the associated turbulent fluctuations of passive scalars such as temperature or salinity. Variations in these passive scalars cause variations in the density of the water, and these variations in density cause variations in the refractive index of the medium (Mobley 1994, Bogucki *et al*. 2004), hence it is also plausible to investigate these turbulent processes through the use of optics.

Along these lines, work has been conducted to investigate the scattering of light by oceanic turbulence (Bogucki *et al*. 1998, Bogucki *et al*. 2004, Bogucki *et al*. 2007, Bogucki *et al*. 2007). These works show that through changes in the index of refraction, turbulent variations in the fluid scatter light into near-forward angles. This observation is akin to the apparent twinkling of stars in the night sky: atmospheric turbulence results in near-forward scattering of the starlight, producing the twinkling effect. The Volume Scattering Coefficient and total scattering coefficient are used to quantify this scattering, and will be discussed later in the chapter, but first, let us more formally define this interaction of light with the propagation medium.

### *1.1.2 Radiative Transfer*

Radiative transfer is a theory for describing the propagation of light through a medium. As the light wave propagates, it will interact with the propagation medium through both scattering and absorption. The current work assumes negligible absorption, as all measurements are made in purified drinking water, over a 27cm pathlength. As mentioned earlier, scattering is induced by changes in the index of refraction encountered along the propagation path. As light impinges upon a particle suspended in the water, for example, it encounters a difference between the index of refraction in the propagation medium (water in the present case) and the suspended particle. This change in index of refraction will change the speed of the light as it propagates through the particle, and upon exiting the particle and reentering the water, the speed of the light will return to its original speed. Thus the interaction of the light with the suspended particle changes the direction of propagation of the light, scattering the light at a particular angle relative to its original direction.

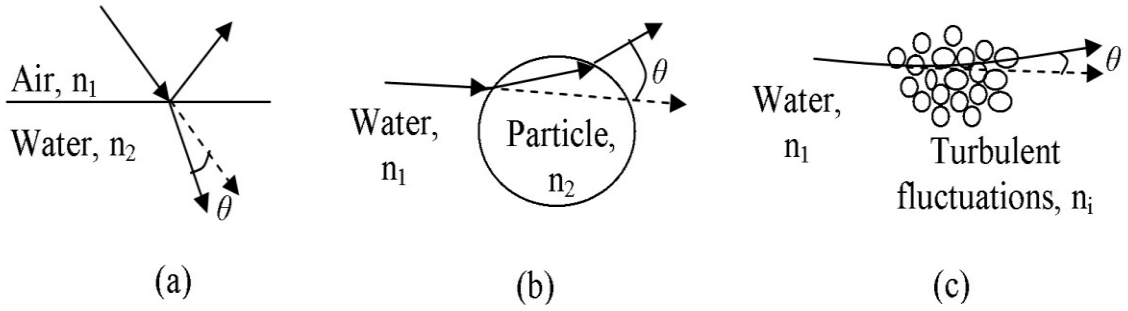


**Figure 1.1.** Three cases of scattering in the ocean showing (a) reflection and refraction from an idealized planar air-sea interface, (b) scattering from a suspended particle, and (c) scattering from turbulent fluctuations. *n* is the real index of refraction of the propagation medium, and $\theta$ the resulting scattering angle between the incident and transmitted light beams.

This effective bending of the light beam is depicted in Figure 1.1 for three cases of interaction: (a) light incident at the air-sea interface, (b) light incident upon a suspended particle, (c) light incident upon turbulent fluctuations, which may be visualized as light incident upon several blobs of varying indices of refraction, resembling several suspended particles.

### *1.1.3 Volume Scattering Function*

The Volume Scattering Function (VSF), $\beta$, describes the angular distribution of the scattered radiation ($m^{-1}sr^{-1}$):

$$\beta(\theta) = \frac{dI(\theta)}{E_O dv}, \tag{1.1}$$

where $\theta$ is the scattering angle, $dI(\theta)$ is the scattered radiant intensity ($Wm^{-1}sr^{-1}$) at angle $\theta$, $E_O$ is the incident irradiance ($Wm^{-3}$), and $dv$ is the unit volume from which $dI(\theta)$ is scattered. This geometry is depicted in Figure 1.2. The largest contribution to the volume scattering function comes from forward scattering, or scattering at an angle $\theta$ less than $90^o$ (Jerlov 1968). The VSF is useful for diagnosing the composition of a particular body of water, as different constituents will contribute to the VSF at different angles and different magnitudes. For example, the VSF for coastal water, in comparison to that of pure seawater, has a much higher magnitude of the VSF over the forward scattering angles (Petzold 1972). The presence of particulates in the coastal water significantly increases the VSF in the forward direction, with larger particles dominating at the near-forward angles, and small particles dominating at the intermediate angles (larger than approximately 10 degrees) (Mobley 1994). The effect of turbulence on the near-forward

VSF, however, has not yet been well defined. It has been suggested that turbulent scattering dominates the VSF in the very near-forward, reserving the intermediate near-forward angles for particulates (Bogucki *et al.* 1998).

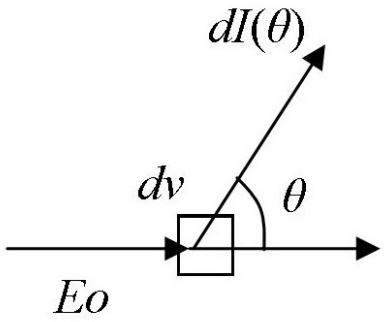


**Figure 1.2.** Geometry of light scattering used to define the Volume Scattering Function (VSF). *Eo* is the incident irradiance, *dv* the scattering volume, *dI*($\theta$) the scattered radiant intensity, and $\theta$ the scattering angle.

### *1.1.4 Total Scattering Coefficient*

When the VSF is integrated over all scattering angles, the total scattering coefficient, *b*, is determined. The total scattering coefficient describes how much light has been scattered out of the incident light beam, and is given by

$$b = 2\pi \int_0^{\pi} \beta(\theta) \sin(\theta) d\theta . \tag{1.2}$$

Typical values of *b*, due primarily to scattering from oceanic particles and pure water, vary from less than 0.05 $m^{-1}$ in the deep ocean to > 1 $m^{-1}$ in the coastal ocean (Jaffe 1995). Recent *in situ* wavefront sensor measurements of the turbulent scattering coefficient, $b_{turbulence}$, demonstrate that scattering from turbulence can vary from less than 0.1 $m^{-1}$ in the deep ocean to as much as 10 $m^{-1}$ near the surface (Bogucki *et al*. 2007).

### *1.1.5 Polarization*

Polarization is another important parameter for studying light propagation in the ocean, as it gives additional information about the propagation medium. The polarization of a light beam refers to the orientation of the electric field making up the light beam. In the case of linearly polarized light, as is commonly used in remote sensing and will be the focus of the present work, the electric field may vary in magnitude, but the orientation of the field is constant, having a constant plane-of-vibration in which the electric field vector oscillates. This constant orientation of the field may be broken down into its orthogonal components in the Cartesian coordinates, so that a wave propagating along the z-axis will have two components along the x- and y-axis: $\vec{E}(z,t) = \vec{E}_X(z,t) + \vec{E}_Y(z,t)$. In the remainder of the work, these orthogonal components of the polarized beam will be referred to as the co-polarized and cross-polarized components, where the co-polarized component shares the same polarization as the light source, assumed to be initially polarized. The depolarization of this initially polarized beam as it propagates through the water column will be discussed further in Chapter 5.

## 1.2 Light Scattering and Depolarization from Oceanic Turbulence

In the ocean, the near-forward part of the oceanic volume scattering function (VSF) is determined by light interactions with turbulent inhomogeneities of the refractive index field (Bogucki *et al.* 1998), mostly due to temperature fluctuations. These turbulent-induced inhomogeneities scatter light at near-forward angles. Both experimental studies of small-angle scattering and measurements of the oceanic VSF in

the range of $10^{-7}$ to $10^{-3}$ rad demonstrate that the total scattering coefficient, $b$, due solely to oceanic turbulence, can be on the order of 10 $m^{-1}$ (Bogucki *et al*. 2004). Thus, the small-angle scattering function due to turbulence can be significantly larger than typical values due to the combined contribution of oceanic particles and the 'pure water' scattering function, which is typically less than 0.25 $m^{-1}$ and 0.05 $m^{-1}$ in coastal and deep ocean waters, respectively (Jaffe 1995, Bogucki *et al*. 1998). The large value of the turbulent scattering coefficient (Bogucki *et al*. 2004), $b_{turbulence} >> 1$ $m^{-1}$, implies that the photon mean path length, given by $l_{phot} \sim 1/b << 1$ m, is short (Bogucki *et al*. 2007). Consequently, most remotely sensed photons emerging from any pathlength > 1 m will undergo multiple forward scattering events in turbulent flow, but very few scattering events on oceanic particulates in comparison, before reaching a remote detector.

In the case of oceanic lidar, for example, as the light propagates through the water column it undergoes multiple near-forward scattering events from turbulent inhomogeneities until it encounters a particle inducing a single backscattering event close to $180^o$, as depicted in Figure 1.3. As the light then propagates upward through the water column, it again undergoes multiple near-forward scattering events from turbulent inhomogeneities before leaving the water. Thus, the scattering processes that contribute to the lidar return signal from the water are small-angle multiple-scattering events in the near-forward, and a single particle backscattering event close to $180^o$. The effect of multiple forward scattering from turbulent inhomogeneities is therefore of importance for analyzing the return signals of remote sensing instruments. These effects are of particular importance in the case of polarimetric remote sensing, where these multiple forward

scattering events can also induce depolarization of the polarized incident beam (Strohbehn and Clifford 1967).

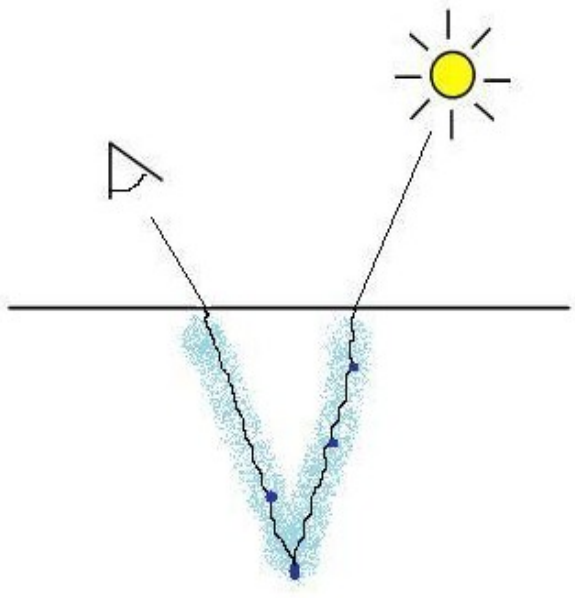

**Figure 1.3.** Sketch of the oceanic scattering processes contributing to a remote sensing signal: multiple-forward scattering in the near-forward, single-scattering from particles, and a single backscattering event near $180^{o}$.

The primary reason for the effectiveness of polarimetric remote sensing of oceanic waters is its greater signal sensitivity to changes in refractive index than is the case for non-polarimetric intensity measurements (Churnside 2008). Thus, the use of polarization in lidar systems is being actively pursued as a means of enhancing the sensitivity of those systems to characteristics of seawater and its constituents. This is motivated by the fact that the intensity and polarization properties of scattered light contain important retrievable information about the scattering particles: quantity, shape, etc. (for example, Yang *et al*. 2003, Hu *et al*. 1987, Spinrad and Brown 1993, Asano and Sato 1980, and Hielscher *et al*. 1997).

Much like the absorption, scattering, and attenuation coefficients used in optics to quantify the changes in intensity of a propagating light beam, the depolarization rate, $\gamma$, is used to quantify changes in the polarization state of the propagating light beam. With sufficient a priori knowledge of what physical mechanisms absorb, scatter, or attenuate light, investigators utilize measurement of light absorption, scattering, and attenuation to infer the constituents and physical processes present in the propagation medium. Similarly, if more is known regarding the behavior of the depolarization rate and what causes changes in the depolarization rate, this property will prove another useful tool to infer information about a medium from optical measurements.

**1.3 Objectives**

While it has been acknowledged that turbulence plays a significant role in near-forward scattering, the effects of this scattering on oceanic optical measurements are not well understood. In particular, little is known about the depolarization magnitude of near-forward scattered light from oceanic turbulence. Knowledge of the depolarizing effects of turbulence is important for better understanding of the return signal from polarimetric measurements in ocean optics. Just as in measurements of scattering or absorption it is important to understand how the light interacts with the water column in order to better interpret the scattering or absorption signal, and so infer information such as the concentration, size, and shape of particles, so too it is important to understand what interactions are affecting the polarimetric signal, allowing for better interpretation of the

information carried by the signal. Although turbulent interaction with the light is only a piece of the resulting signal, it is nonetheless important to understand its contribution.

Thus, the present work aims to quantify the effects of turbulence on scattering and depolarization in the near-forward by measuring the depolarization of a linearly polarized beam, resulting from multiple near-forward scattering from turbulence. The focus will be on turbulent inhomogeneities induced by thermal fluctuations, and thus pure water will be used in the experiments. Light depolarization will be observed over a range of strengths of convective turbulent flow in a laboratory setting, with turbulent parameters corresponding to those characteristic of the oceanic mixed layer. Conducting these measurements in a laboratory setting allows for the measurements to be made on controlled turbulent flow. In order to achieve this aim, the first part of the work will focus on characterizing the flow features and turbulent parameters within the convective tank. With the turbulent flow characterized, the second part of the work will focus on characterizing the depolarization from the turbulent flow.

### 1.4 Overview of Work

The experimental setup, consisting of a Rayleigh-Bénard convective tank, a Particle Image Velocimetry (PIV) System, profiling thermistors, and a polarized diffractometer, will be described in Chapter 2. The non-dimensional parameters and flow characteristics of Rayleigh-Bénard convection will also be discussed in Chapter 2.

Chapter 3 will present the first turbulent parameter used to characterize the flow, the Turbulent Kinetic Energy Dissipation (TKED) rate. The chapter will begin with an

introduction to the TKED rate and how it is obtained from PIV measurements. The method and calibration for obtaining PIV measurements will then be presented, before detailing the large scale velocities and characteristics of the flow. The chapter will conclude with measurement results of the TKED rates over a range of turbulent strengths.

Chapter 4 will then present the second turbulent parameter used to characterize the flow, the Turbulent Thermal Dissipation (TD) rate. The chapter will also begin with an introduction, detailing the TD rate and how it may be obtained from horizontal temperature profiles and one-dimensional thermal gradient spectra across the tank, obtained with a set of profiling thermistors. Measurement method, calibration, and results will then be presented.

A formal definition of the depolarization rate will be introduced in Chapter 5 along with the measurement method using a polarized diffractometer. Calibration, noise removal of the images, and associated errors will then be discussed before presenting the measured depolarization rates for a range of turbulent strengths. A summary of the work will then be presented in Chapter 6 along with a discussion of the conclusions and applicability of the presented results. Finally, the chapter will conclude with a discussion of future directions of such work.

## Chapter 2: Experimental Setup

As discussed in Chapter 1, the primary aim of the present work is to assess the importance of turbulence on near-forward scattering through characterization of the near-forward depolarization rate, $\gamma$, for a range of turbulent strengths, in a controlled laboratory setting. Thus, measurements were made upon a Rayleigh-Bénard convective cell, depicted in Figure 2.1, which was used to produce controlled turbulent convective flow. The first objective of the experiments presented here is to characterize the turbulent flow within the convective cell by measuring the non-dimensional parameters (Rayleigh and Nusselt numbers) describing the flow, large scale flow structure, and the dissipation rates (Turbulent Kinetic Energy Dissipation rate, $\varepsilon$, and Thermal Dissipation rate, $\chi_\theta$). A Particle Image Velocimetry (PIV) system and a set of profiling thermistors were used for this objective.

With the turbulent flow characterized by measurements from the PIV and thermistors, the second objective was to characterize the optical properties of the flow, focusing on the depolarization rate, $\gamma$. A polarized diffractometer setup was thus used to measure the depolarization from the flow. Through these objectives, this work will shed light on the importance of turbulence on oceanic optical measurements. While the methodology and results of these measurements will be presented in Chapters 3, 4, and 5, the instrumentation and acquisition used for the measurements will be discussed here.

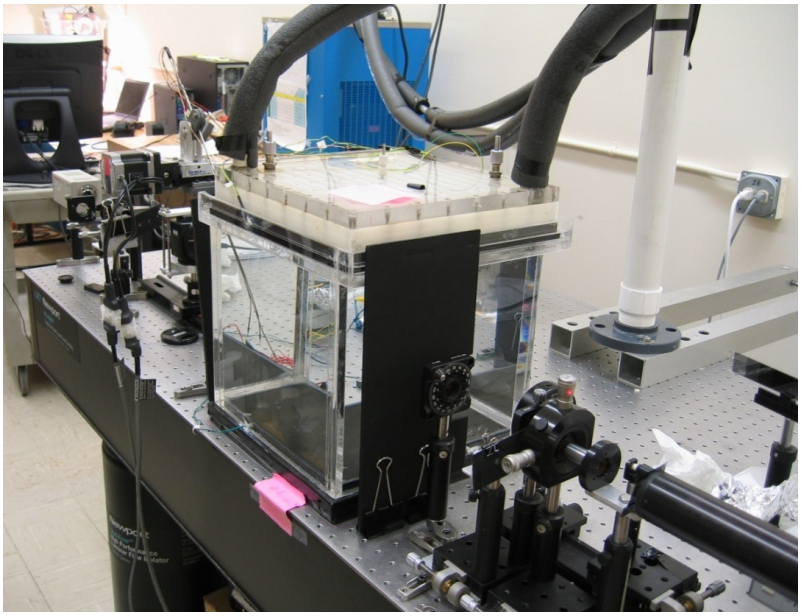

**Figure 2.1.** Photograph showing the convective tank and instrumentation used for turbulent and optical measurements, discussed and depicted in more detail below.

## 2.1 Background

Investigating turbulent thermal convection in the laboratory is not a new concept, but a useful one for studying turbulence in a controlled state. Many works have detailed various aspects of the thermal convective flow within tanks of varying sizes and geometries in air (Deardorff and Willis 1966), and in water (Nikolaenko and Ahlers 2003, Grossman and Loehse 2001, Xia *et al.* 2003, Wang and Xia 2003, Zhou *et al.* 2008, Daya and Ecke 2001, Xi and Xia 2008). These works have sought to characterize the non-dimensional parameters of the flow (Nikolaenko and Ahlers 2003, Grossman and Loehse 2001); the velocity field, temperature field, statistical quantities, and spatial variations of such quantities of the flow (Xia *et al.* 2003, Wang and Xia 2003, Zhou *et al.* 2008); and the influence of the container geometry upon the flow and associated properties (Daya and Ecke 2001, Xi and Xia 2008).

Rayleigh-Bénard convective flow in the laboratory is typically produced by cooling the top of the observation tank and heating the tank bottom, creating an inverse temperature gradient vertically across the tank. By maintaining this cooling/heating of the respective parts of the tank, a buoyancy-driven large-scale circulation is induced. The large scale flow is driven by the thermal plumes rising and falling from the top and bottom plates, which sets up a circulatory flow in one direction, occasionally exhibiting a momentary flow reversal. The circulatory flow is concentrated near the boundaries of the convection cell, surrounding a central region that is usually weaker in shear than the boundaries. The quieter flow in the central part of the cell, being far from the energetic plumes near the sidewalls, may typically be described as approximately homogeneous and isotropic (Zhou *et al.* 2008), and is thus a useful region for examining the small-scale turbulent properties of the flow. The magnitude of a velocity flow field, averaged over a twelve minute time series obtained from PIV measurements of a vertical transect of the tank, is shown in Figure 2.2. The method for obtaining this image and results for different turbulent strengths will be presented in Chapter 3. Edge contamination in the PIV processing produced the discontinuity around the edge of the image. The dark region extending from the top into the central region is the shadow of a thermistor. Both the thermistor and discontinuity near the edges were masked out for calculations.

The flow field characteristics and non-dimensional parameters of the flow vary with the tank size and geometry (Daya and Ecke 2001), however, thus thorough measurements are still needed to characterize the turbulent flow within the convective tank for the current setup.

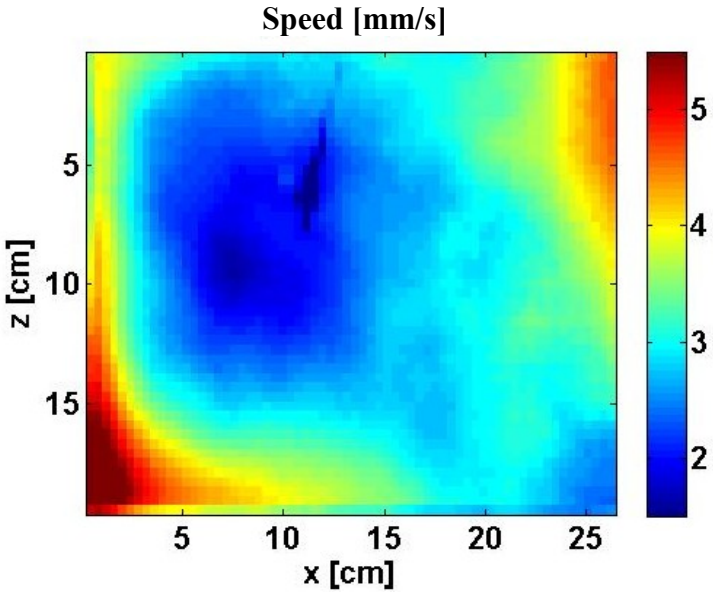


**Figure 2.2.** A cross section of the tank showing the time averaged speed flow field, averaged over a twelve minute time series, showing the flow structure of the convective cell: a quieter low velocity core surrounded by a higher velocity rotational flow. The dark region extending from the top into the central region is the shadow of a thermistor. Edge contamination in the PIV processing produced the discontinuity around the edge of the image. The thermistor and discontinuity near the edges were masked out for calculations.

## 2.2 Rayleigh-Bénard Convective Turbulence

### *2.2.1 Rayleigh-Bénard Convective Tank*

Turbulence measurements were made on a Rayleigh-Bénard convective tank of cubic geometry, depicted in Figure 2.3. The 27 x 27 x 27 cm Plexiglas tank is filled with commercially available bottled Zephyrhills drinking water, then heated by a Topward Dual-Tracking DC Power Supply (6603D) on the bottom and cooled by water from a Cole-Parmer Polystat Temperature Controller on the top. This produces a controllable temperature difference, $\Delta T$, across the tank. This temperature gradient induces in the tank a controllable, fully turbulent flow. At the tank centerline, this convective cell

provides a source of homogeneous isotropic turbulence, resembling oceanic small scale turbulent flow (Domaradzki and Metcalfe 1988). The heater and cooler are adjusted to maintain the mean temperature of the tank within 1 $^{o}$C of the ambient room temperature (approximately 20 $^{o}$C), and the temperature difference, $\Delta T$, is varied between approximately 1 and 12 $^{o}$C.

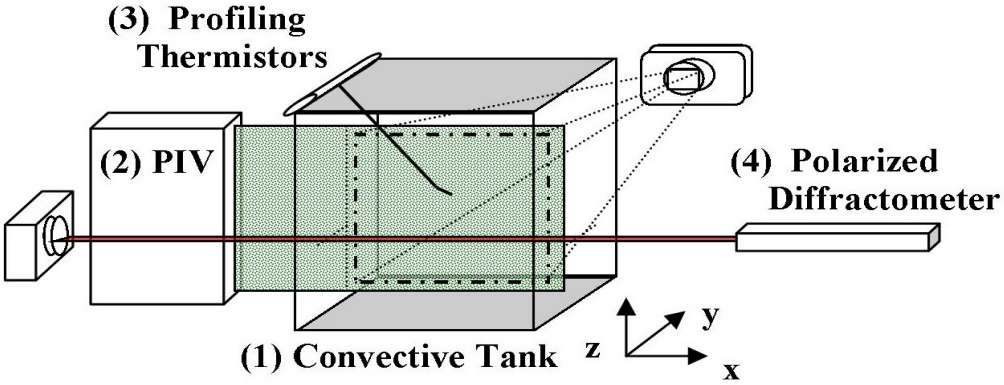


(a)

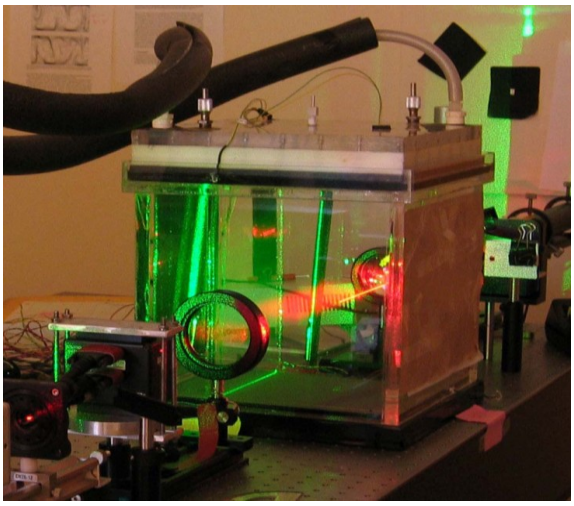

(b)

**Figure 2.3.** (a) Composite sketch showing orientation of all measurements: (1) Rayleigh-Bénard convective tank with heated bottom and cooled top plates, (2) PIV sheet cuts the tank along the x-z plane, and is imaged by a camera along the y-axis, (3) three thermistors, spaced along the x-axis, profile along the y-axis, and (4) polarized diffractometer's optical axis is along the x-axis. (b) Photograph of the tank showing relation of the optical transects of the tank.

### 2.2.2 Non-dimensional Parameters of the Flow

***Rayleigh Number***

The Rayleigh number, a non-dimensional parameter describing the strength of convective turbulence of a flow, is given by the ratio of the destabilizing buoyancy force to the stabilizing viscous force:

$$Ra = \frac{\alpha_T g d^3 \Delta T}{\nu D_T}. \tag{2.1}$$

Here, $\alpha_T$ is the coefficient of thermal expansion of water at 20 $^oC$ ($\alpha_T = 2.1*10^{-4}$ $^oC^{-1}$), $g$ the acceleration due to gravity (9.8 $ms^{-2}$), $d$ the depth of the tank (0.27 m), $\Delta T$ the temperature difference across the tank, $\nu$ the kinematic viscosity of water at 20 $^oC$ ($\nu = 1.005*10^{-6}$ $m^2s^{-1}$), and $D_T$ the thermal diffusivity of water at 20 $^oC$ ($D_T = 1.42*10^{-7}$ $m^2s^{-1}$).

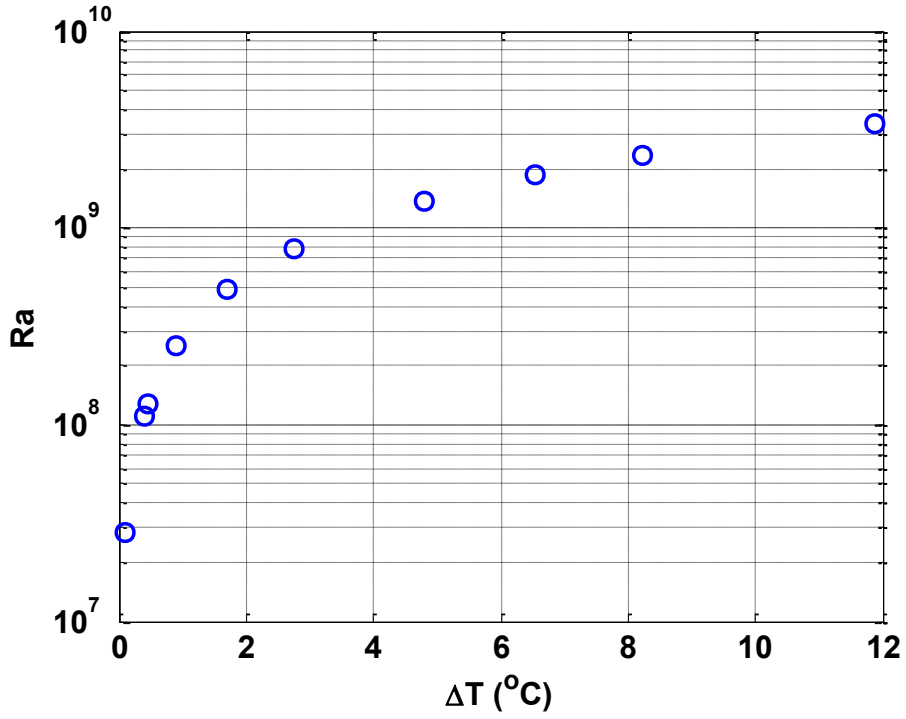


**Figure 2.4.** Non-dimensional Rayleigh number, *Ra*, plotted against $\Delta T$, the temperature difference across the convective tank, over the range covered in this set of experiments.

Lower *Ra* numbers, on the order of $10^5$ or less, are characteristic of stable flow, while higher values are characteristic of increasingly turbulent flow (Krishnamurti 1970). This work presents measurement for fully turbulent flow, with *Ra* between $3*10^7$ and $4*10^9$, corresponding to temperature differences across the tank between about 1 $^oC$ and 12 $^oC$, as shown by the data in Figure 2.4. With the mean tank temperature centered about the ambient room temperature (20 $^oC$), these measurements were made for a Prandtl number, $\Pr = \nu / D_T$, of approximately 7.

***Nusselt Number***

For convective flows, the non-dimensional Nusselt number, *Nu*, is used to quantify the heat transport of the flow, characterized by the ratio of the convective heat transfer to conductive heat transfer. As with *Ra*, lower values of *Nu* (on the order of 1) represent stable flows, while higher numbers (on the order of 10 or 100) are characteristic of turbulent flow (Tritton 1988). There are several different models relating the Nusselt number to the Rayleigh number depending upon the size of the Prandtl and Rayleigh numbers of the flow (Nikolaenko and Ahlers 2003, Grossman and Lohse 2001). Thus, under the conditions of the current setup (Pr ~7 and Ra > $10^8$), the expected Nusselt number can be expressed as $Nu = 0.05\mathrm{Ra}^{1/3}$ (Nikolaenko and Ahlers 2003, Grossman and Lohse 2001), where the coefficient has been experimentally fit to the data.

In terms of the experimental parameters, however, Nu can be expressed as

$$Nu = \frac{Hd}{\kappa \Delta T}, \tag{2.2}$$

where $H$ is the heat-current density, or heat flux, $\kappa$ the thermal conductivity of the water, and $d$ and $\Delta T$ are again the height and temperature difference across the tank, respectively (Nikolaenko and Ahlers 2003).

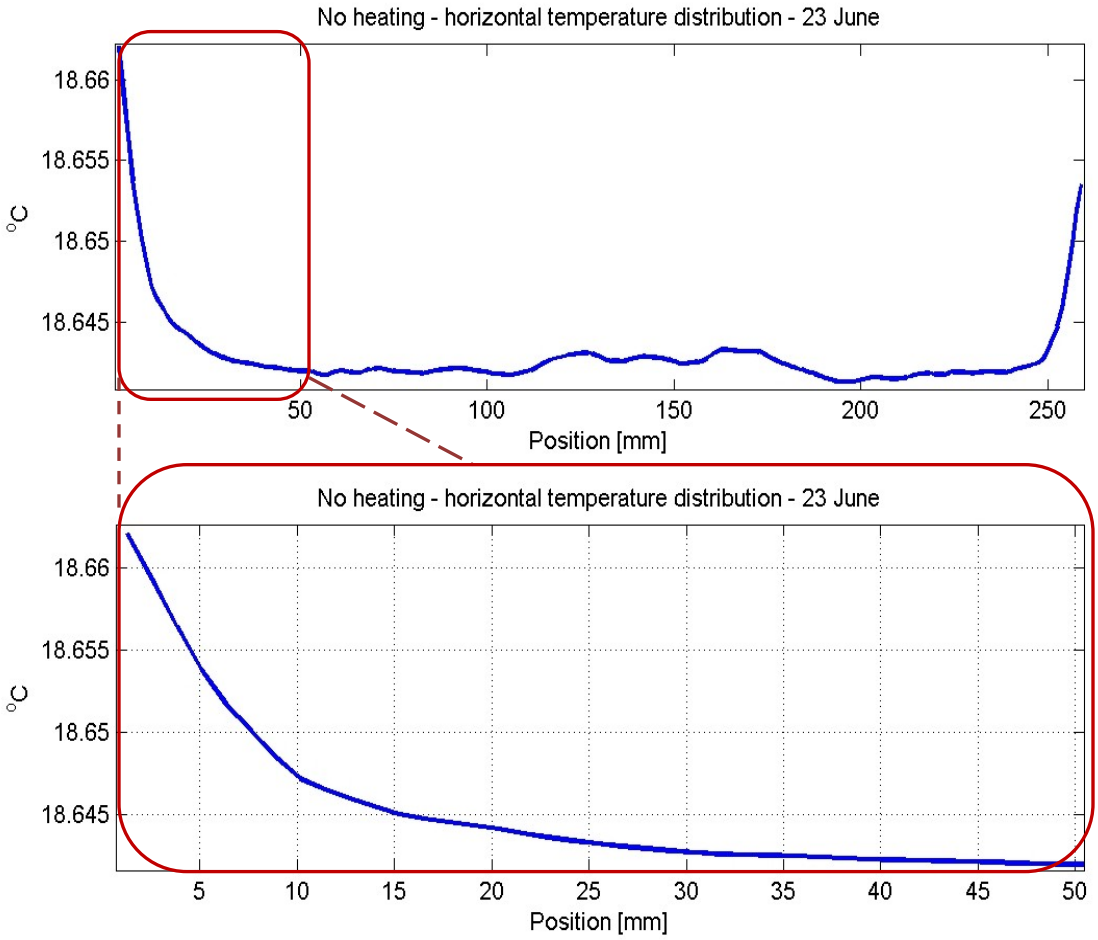


**Figure 2.5.** A temperature profile across the convective tank in the absence of heating or cooling, showing the thermal boundary layers associated with heat transfer through the sidewalls. The top plot shows the temperature profile across the entire tank, and the bottom plot shows an enlargement of the profile across one side of the tank.

In order to provide an accurate estimate of the Nusselt number characterizing the flow used in the experiment, the heat loss from the walls must also be taken into account. Thus, the tank was allowed to equilibrate with the room temperature in the absence of

heating and cooling from the top and bottom plates. With the tank in equilibrium, a temperature profile was taken across the boundary layer near the tank walls, as shown in Figure 2.5. From the thermal gradient across the boundary layer, with $\delta T$ denoting the temperature difference across the layer and $\delta x$ the width of the layer, Fourier's law of heat conduction, $h = \frac{-\kappa \delta T}{\delta x}$, was used to determine the heat transfer through the walls, which was found to be less than 0.2 W.

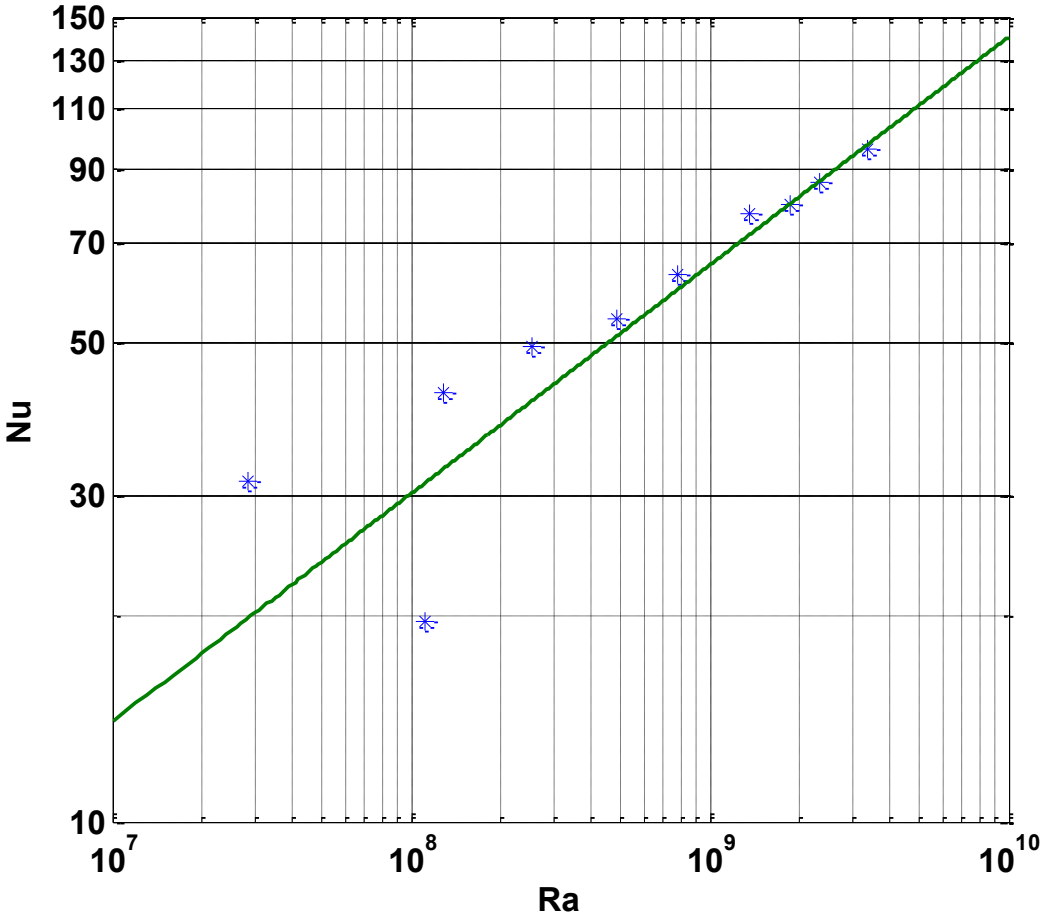


**Figure 2.6.** Non-dimensional Nusselt number, *Nu*, plotted against Rayleigh number, *Ra*, over the range of turbulent strengths measured in the current work. The blue asterisks correspond to the discrete set of measurements made in the present work. The solid line is a model for *Nu* as a function of *Ra* from Grossman and Lohse (2001).

The range of Nusselt and Rayleigh numbers over the range of $\Delta T$ covered in the experiments presented here are shown in Figure 2.6 by the asterisks. The solid line is the experimentally obtained model from Grossman and Lohse (2001): $Nu = 0.05Ra^{1/3}$. The data are well-correlated with the model (r = 0.96), but likely differ at lower *Ra* due to heightened uncertainty in temperature measurements at lower $\Delta T$.

### *2.2.3 Frequency of Core Rotation*

One other interesting characteristic of the flow is the frequency of the rotational motion depicted in Figure 2.2 above. Xia *et al.* (2003) concluded that the normalized rotational frequency, $\omega_o$, of the lower velocity core within Rayleigh-Bénard convective flow scaled with *Ra* as $\omega_o d^2 2D_T = 0.318Ra^{0.496}$, where *d* is again the depth of the tank, and $D_T$ the thermal diffusivity. The expected rotational frequencies over the range of turbulent strengths observed here are plotted in Figure 2.7. Thus, one would expect the rotational frequency of the central region to be on the order of 15 to 70 seconds depending on turbulent strength. Interestingly, the depolarization optical measurements demonstrated cyclic variations in the optical properties of the flow on the order of twenty to thirty minutes, as will be discussed in Chapter 5. This longer time-scale could be evidence of flow-reversal or the accumulation of thermal plumes, but further investigation is needed as the Particle Image Velocimetry time series were not long enough to observe this frequency, but rather the shorter frequency of the central core rotation.

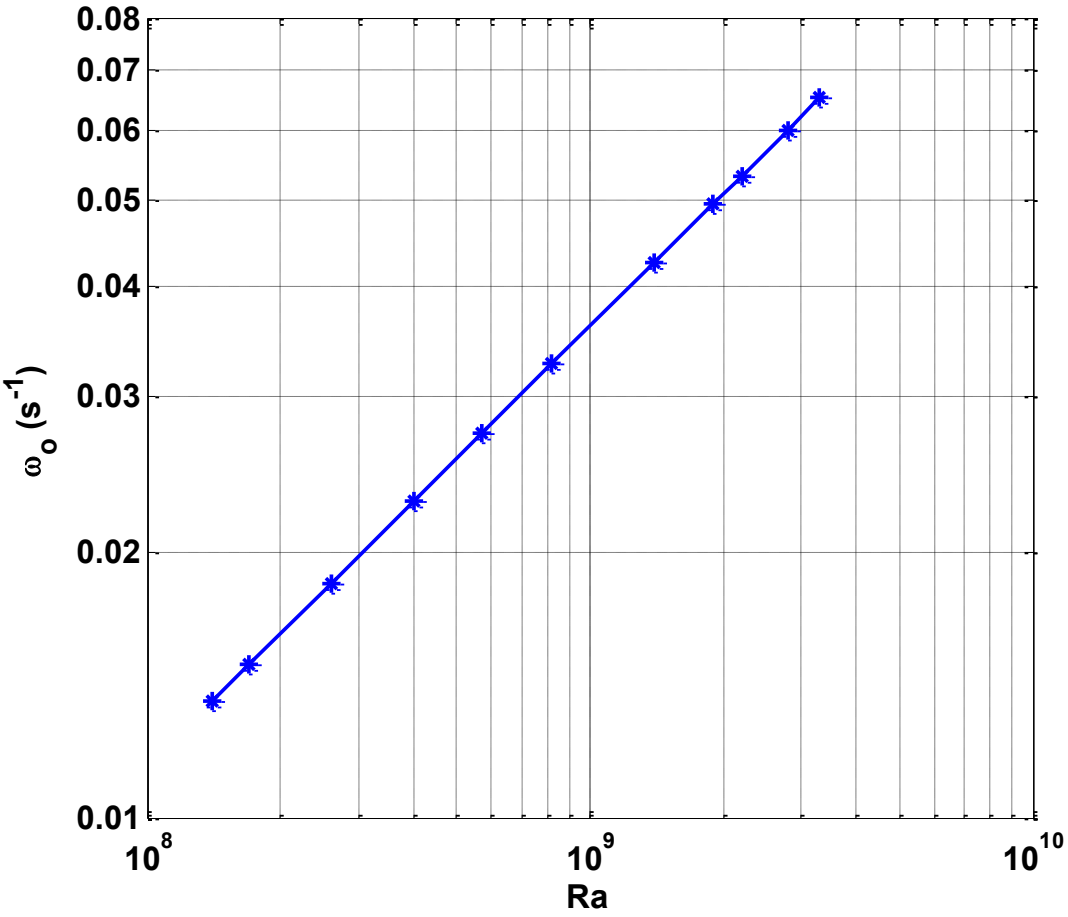


**Figure 2.7.** Expected rotational frequency of the lower velocity core as a function of *Ra* from the formulation of Xia *et al.* (2003).

### 2.3 Instrumentation for Characterizing Turbulent Flow and Optical Properties

In order to characterize the turbulent flow within the convective tank, Particle Image Velocimetry and profiling thermistors were employed to obtain the large scale flow within the tank, and the dissipation rates. To characterize the depolarizing effects of near-forward scattering from the turbulent flow within the tank, a polarized diffractometer was employed. The collective positioning of these three sets of instruments was shown in the schematic of Figure 2.3 (a). A description of the setup and

acquisition for each set of instrumentation will be described here, while further details regarding the analysis and results from these instruments are presented in Chapters 3, 4, and 5.

### *2.3.1 Particle Image Velocimetry System*

Particle Image Velocimetry (PIV) and thermistors were used to determine the relevant turbulent quantities characterizing the flow, namely the energy and temperature dissipation rates. The PIV setup consists of a pulsed, frequency-doubled Nd:YAG laser (532 nm), which illuminates a vertical sheet along the x-z plane of the tank, transecting the center of the convective cell, as seen in Figure 2.8. This sheet is then imaged by a CCD (Charge Coupled Device) camera, which records a time series of snapshots of the flow. The CCD contains 1600 x 1186 pixels, which images a 26 x 20 cm subset of the illuminated tank cross section. The flow is seeded with 10 μm spherical neutrally buoyant particles (Dantec Dynamics S-HGS) so that each pair of successive images obtained by the camera, like that shown in Figure 2.9, can be cross correlated to obtain the instantaneous velocity flow field. These velocity fields are then used to obtain the turbulent kinetic energy dissipation (TKED) rate, the method of which will be discussed in Chapter 3. Images were obtained for each discrete $\Delta T$ across the tank, at a rate of 1-4 frames per second, as was optimal for determining the velocity vector fields depending upon the turbulent strength. Software used for acquisition limited the time series to a few minutes, thus 2 to 3 minute long time series (depending on sampling frequency) were stitched together to obtain a 15 minute long time series for each $\Delta T$.

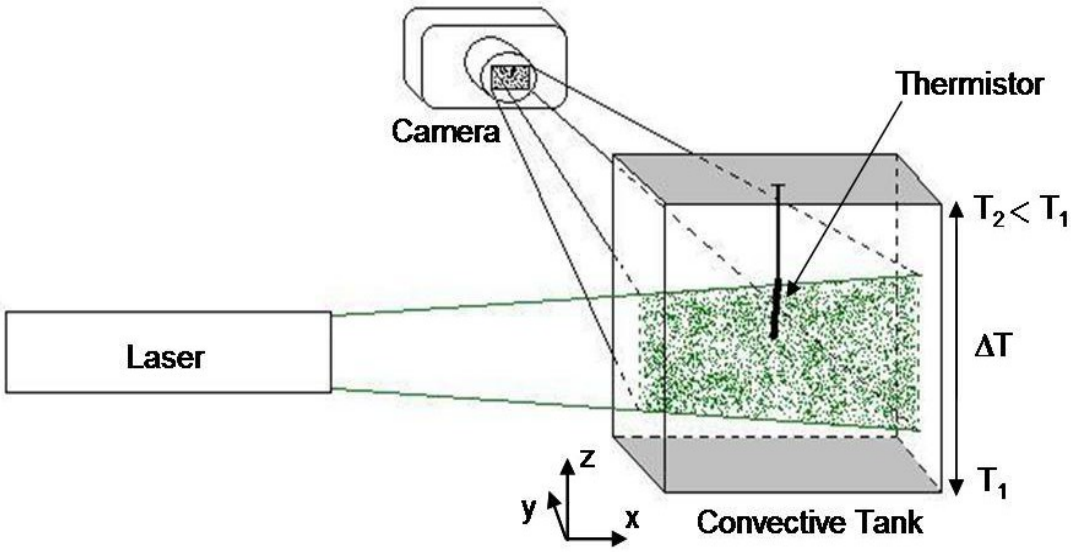


(a)

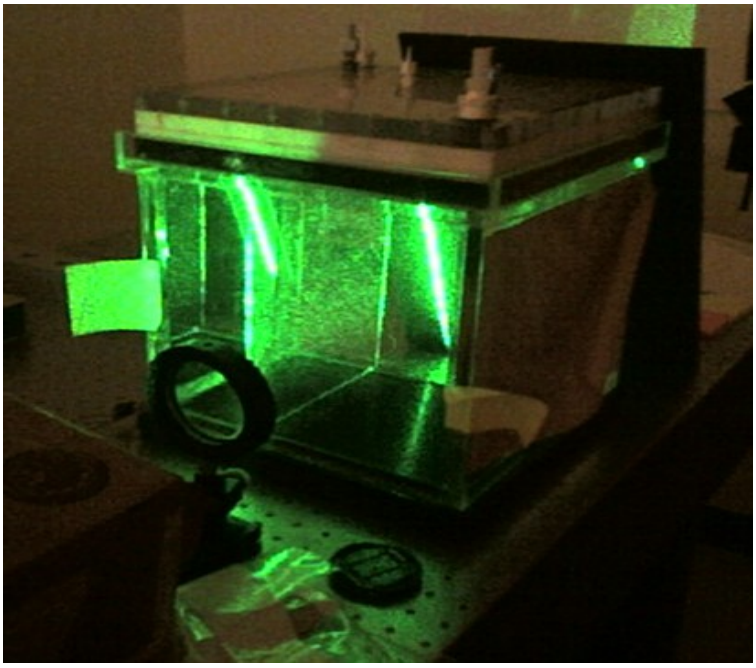

(b)

**Figure 2.8.** (a) Schematic of the Particle Image Velocimetry system showing the vertical transect of the convective tank, illuminated by the Nd:YAG laser, and imaged by the CCD Camera. (b) Photograph depicting the PIV-illuminated transect of the tank.

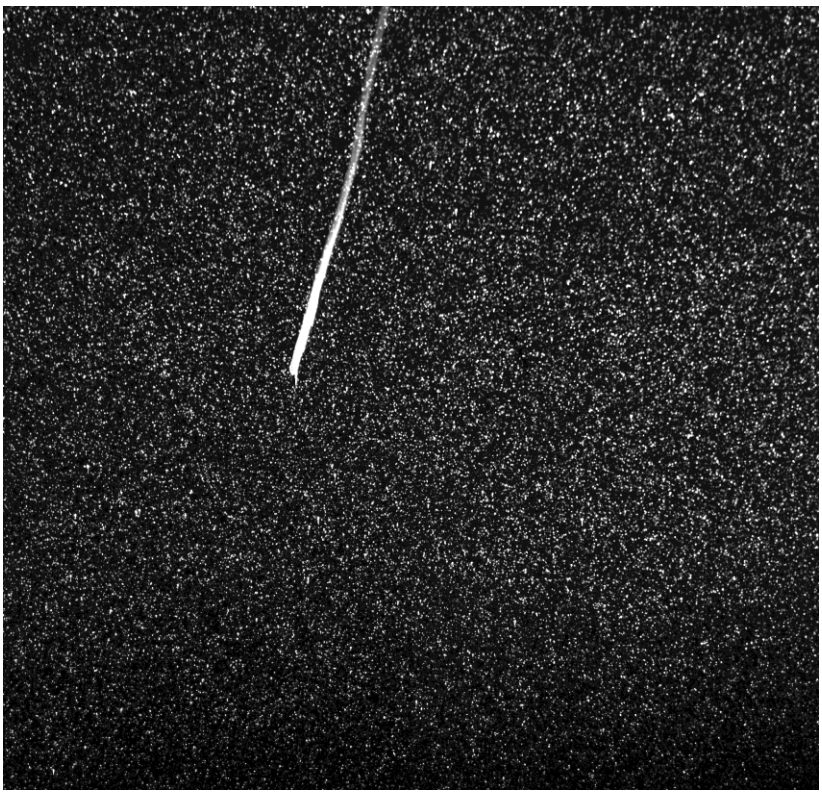

**Figure 2.9.** Sample PIV image (20 cm high by 26 cm across) showing the flow seeded with 10 μm particles. The white streak extending from the top into the center of the tank is a thermistor in the cell interior. The apparent vertical gradient in particles is an artifact due to weaker laser intensity near the bottom of the tank. Pairs of such images are cross-correlated to track movement of the particles, and so obtain velocity flow fields for the tank cross section.

### *2.3.2 Profiling Thermistors*

Spatial temperature fields were also obtained via a set of three fast thermistors (FP07) connected to a VEXTA stepping motorized stage. The thermistors, manufactured by GE Thermometics, have response time of 7 ms. The first two thermistors were spaced 3 cm apart, and the second and third were placed 5 cm apart, horizontally, along the x-axis, parallel to the PIV sheet. The thermistors then profiled a horizontal transect of the tank centerline, along the y-axis, as seen in Figure 2.10. The speed of the motor

controlling the thermistors was varied according to the strength of the turbulent flow. From these time series of spatial temperature fluctuations, the spatial temperature spectra are determined. These spectra are used to derive estimates of the temperature dissipation (TD) rate, discussed in more detail in Chapter 3.

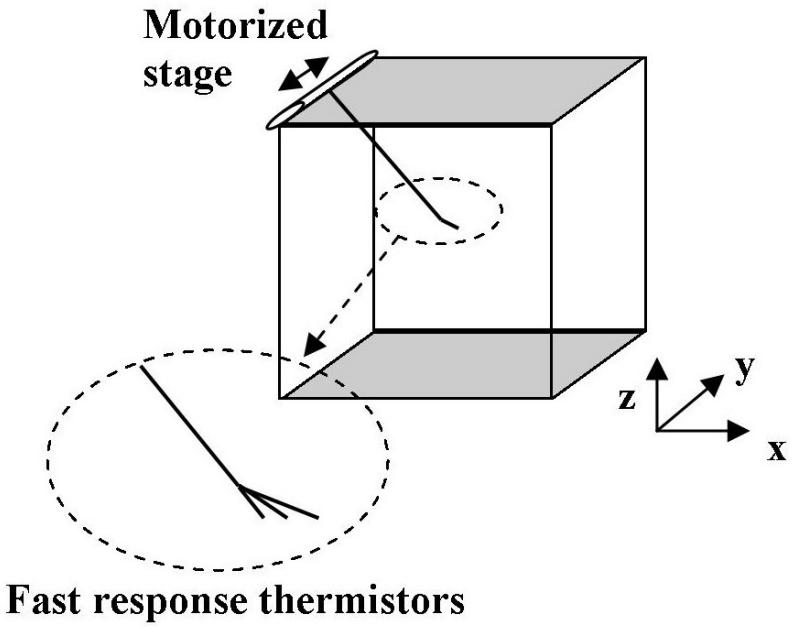


**Figure 2.10.** Schematic of profiling fast response thermistors, showing the motor movement along the y-axis, and the thermistor separation along the x-axis.

### *2.3.3 Polarized Diffractometer*

Diffractometer measurements were also obtained to characterize the depolarizing effects of scattering from turbulence. The experimental setup is shown in Figure 2.11, and consists of a 632.8 nm 35 mW JDS Uniphase Helium-Neon (HeNe) laser, which generates a linearly polarized light beam with a fixed polarization direction and a beam diameter of 0.7 mm. The polarized laser beam is cleaned and expanded by a Newport spatial filter to provide a light source with a clean Gaussian intensity distribution. The

beam then passes through a Newport linear polarizer (model 10LP-VIS-B), which is aligned with the polarization state of the laser and has an extinction ratio of about 1:4000 at the wavelength of the HeNe laser, to ensure a strong initial state of polarization. The incident beam then traverses the convective tank.

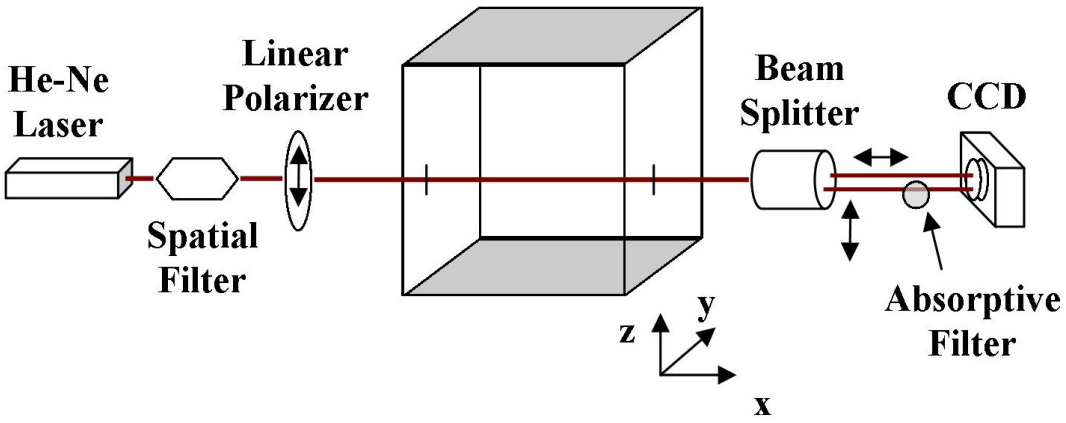


**Figure 2.11.** Schematic showing components of the polarized diffractometer setup: a Helium-Neon laser passes through a spatial filter to expand, re-collimate, and clean the beam, followed by a linear polarizer to ensure strong initial polarization of the beam, before traversing the tank. After the tank, the laser beam passes through a polarized beam splitter and absorptive filters, prior to impinging on a Hamamatsu CCD camera.

Light exiting the tank passes through a ThorLabs polarized beam-splitting calcite crystal displacer (BD40), which is aligned with the polarization direction of the incident beam, and produces two beams: one orthogonally-polarized with respect to the incident beam, $P_X$, and one co-polarized beam, $P_C$, which then passes through a ThorLabs absorptive neutral density filter. The neutral density filter allows for adjusting the intensity of both $P_C$ and $P_X$ to similar magnitude on the CCD camera. Both polarized irradiances ($P_C$ and $P_X$) are simultaneously measured with a Hamamatsu CCD camera (C8484-05G), positioned a distance of 0.67 m from the tank. This setup allows each of the beams, i.e. co- or cross-polarized, to impinge on one half of the CCD array, as shown

in Figure 2.12. The camera contains an 8.7 x 6.6 mm CCD sensor with 1024 x 1344 pixels. The size of a single pixel is 6.45 μm x 6.45 μm. For each $\Delta T$, a 20-minute time series of images was obtained at a rate of 2 frames per second (~2400 frames per time series). The intensities of these images are then summed over all pixels to obtain the total power of each polarization state, $P_C$ and $P_X$, from which the depolarization rate is calculated, as described in chapter 5.

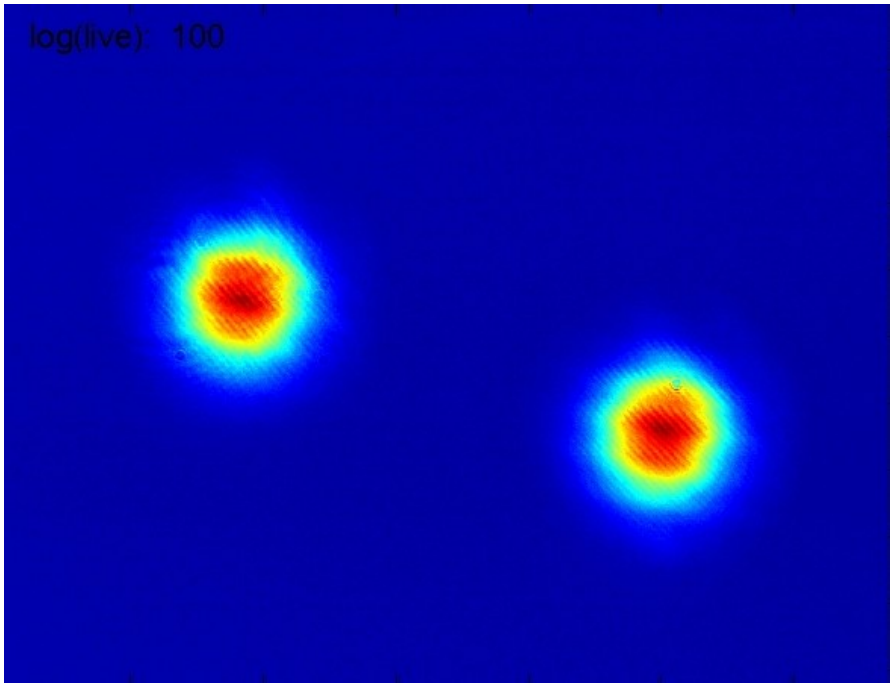


**Figure 2.12.** A five minute time-averaged image from the diffractometer CCD camera showing simultaneous measurement of both orthogonal polarization states, $P_C$ and $P_X$, of the laser beam.

## Chapter 3: Large Scale Flow and Turbulent Kinetic Energy Dissipation

### 3.1 Background

Turbulence within the oceanic water column is strong near the surface, in the mixed layer region, subsides in the mid-column depths, and increases in strength in the bottom of the water column, near the ocean floor (Anis and Moum 1995,Bogucki *et al.* 2007, Thorpe *et al*. 2003, Thorpe 2004). The oceanic mixed layer is the part of the water column just beneath the air-sea interface and that most accessible for remote sensing**.** Typically, the turbulent flow within the oceanic mixed layer is homogeneous and isotropic at the smallest turbulent scales. Homogeneous and isotropic turbulent momentum and scalar fields (within the viscous dissipation range) are characterized by two parameters: $\chi_\theta$, the temperature variance dissipation rate, which will be discussed in Chapter 4, and $\varepsilon$, the rate of turbulent kinetic energy dissipation (TKED).

The TKED rate is an indication of the diffusivity of momentum of the flow, thus providing a measure of how quickly a velocity disturbance within the flow will be dissipated. An expression for the TKED rate may be obtained by examining the instantaneous Navier-Stokes equations of motion for a fluid:

$$\frac{\partial u_i}{\partial t} + u_j \frac{\partial u_i}{\partial x_j} = -\frac{1}{\rho_o}\frac{\partial p}{\partial x_i} - g\left[1 - \alpha_T\left(T - T_o\right)\right]\delta_{i3} + \nu \frac{\partial^2 u_i}{\partial x_j \partial x_j}, \tag{3.1}$$

$$\frac{\partial u_i}{\partial x_i} = 0 \tag{3.2}$$

$$\frac{\partial T}{\partial t} + u_j \frac{\partial T}{\partial x_j} = \kappa \frac{\partial^2 T}{\partial x_f \partial x_j}. \tag{3.3}$$

Equation 3.1 is the mean momentum equation, 3.2 that of continuity, and 3.3 the mean heat equation, where $\rho$ is the fluid density, and the instantaneous velocity, $u$, is the sum of the mean, $U$, and fluctuating, $u'$, velocity parts. The pressure, $p$, and temperature, $T$, have similar Reynolds decomposition: e.g., $p = P + p'$. To look at the mean flow, the instantaneous velocity, pressure, and temperature are replaced by their Reynolds decomposition in equations 3.1 – 3.3 before taking the ensemble average of these equations. Note that for steady mean flow, the mean of the fluctuating components is zero: $\overline{u'_i} = \overline{p'} = \overline{T'} = 0$, also note that ensemble averaging commutes with differentiation: $\overline{\frac{\partial u}{\partial x}} = \frac{\partial}{\partial x}\bar{u}$. Additionally, since the instantaneous components will no longer be used, the fluctuating component will be written as $u$ instead of $u'$ from here forward. Thus, equation 3.1 becomes

$$\frac{\partial U_i}{\partial x_i} = 0 \tag{3.4}$$

for the mean flow. Subtracting equation 3.4 from 3.2 yields the continuity equation for the fluctuating velocity component:

$$\frac{\partial u_i}{\partial x_i} = 0. \tag{3.5}$$

Similarly, by substituting for the Reynolds decomposition, taking the ensemble average, and making use of the continuity equation, 3.1 becomes

$$\frac{\partial U_i}{\partial t} + U_j \frac{\partial U_i}{\partial x_j} + \frac{\partial}{\partial x_j}\left(\overline{u_i u_j}\right) = -\frac{1}{\rho_o}\frac{\partial P}{\partial x_i} - g\left[1 - \alpha_T\left(\overline{T} - T_o\right)\right]\delta_{i3} + \nu \frac{\partial^2 U_i}{\partial x_j \partial x_j}. \tag{3.6}$$

An equation for the rate of change of mean kinetic energy of a turbulent flow can then be found by multiplying 3.6 by $U_i$ and summing over $i$:

$$\frac{D}{Dt}\left(\frac{1}{2}U_i^2\right) = \frac{\partial}{\partial x_j}\left(-\frac{PU_j}{\rho_o} + 2\nu U_i E_{ij} - \overline{u_i u_j} U_i\right)$$

$$- 2\nu E_{ij}E_{ij} + \overline{u_i u_j}\frac{\partial U_i}{\partial x_j} - \frac{g}{\rho_o}\overline{\rho} U_3 \tag{3.7}$$

where $E_{ij}$ is the mean strain rate, given by

$$E_{ij} = \frac{1}{2}\left(\frac{\partial U_i}{\partial x_j} + \frac{\partial U_j}{\partial x_i}\right). \tag{3.8}$$

An equation governing the mean kinetic energy of the turbulent velocity fluctuations is similarly obtained by multiplying the Navier-Stokes equations by $u_i$, again taking the ensemble average, and subtracting the result from the equation for the mean flow given by 3.6. Thus, the governing equation for the turbulent velocity fluctuations is given by

$$\frac{D}{Dt}\overline{\left(\frac{1}{2}u_i^2\right)} = \frac{\partial}{\partial x_j}\left(-\frac{\overline{pu_j}}{\rho_o} + 2\nu\overline{u_i S_{ij}} - \frac{1}{2}\overline{u_i^2 u_j}\right) - \overline{u_i u_j}\frac{\partial U_i}{\partial x_j} + g\alpha\overline{wT} - 2\nu\overline{S_{ij}S_{ij}} \tag{3.9}$$

where $S_{ij}$ is the fluctuating rate of strain:

$$S_{ij} = \frac{1}{2}\left(\frac{\partial u_i}{\partial x_j} + \frac{\partial u_j}{\partial x_i}\right). \tag{3.10}$$

The first three terms on the right hand side of 3.9 are transport terms, thus expressing the transport of mean kinetic energy. The fourth term is the turbulence shear production term, expressing the exchange of kinetic energy between the mean flow and the turbulence. This term is usually positive in sign in (3.9) and negative in sign in (3.7),

representing a loss of mean kinetic energy corresponding to a gain in turbulent kinetic energy. The fifth term expresses the buoyant production (or destruction) of turbulent kinetic energy, as it can have either sign. The final term is the viscous dissipation term, also known as the turbulent kinetic energy dissipation rate, $\varepsilon$:

$$\varepsilon = 2\nu\overline{S_{ij}S_{ij}}\ , \tag{3.11}$$

and is positive in sign. Substituting equation 3.10 into 3.11, $\varepsilon$ is expressed as

$$\varepsilon = \frac{\nu}{2}\overline{\left[\left(\frac{\partial u_i}{\partial x_j}\right)^2 + 2\frac{\partial u_i}{\partial x_j}\frac{\partial u_j}{\partial x_i} + \left(\frac{\partial u_j}{\partial x_i}\right)^2\right]}. \tag{3.12}$$

By summing over all indices, the squared terms may be combined:

$$\varepsilon = \frac{\nu}{2}\overline{\left(\frac{\partial u_i}{\partial x_j}\right)\left(\frac{\partial u_i}{\partial x_j} + \frac{\partial u_j}{\partial x_i}\right)}. \tag{3.13}$$

Or, after expanding the summation, $\varepsilon$ may be expressed as

$$\varepsilon = \nu\left[2\overline{\left(\frac{\partial u}{\partial x}\right)^2} + \overline{\left(\frac{\partial u}{\partial y}\right)^2} + \overline{\left(\frac{\partial u}{\partial z}\right)^2} + 2\overline{\left(\frac{\partial v}{\partial y}\right)^2} + \overline{\left(\frac{\partial v}{\partial x}\right)^2} + \overline{\left(\frac{\partial v}{\partial z}\right)^2}\right]$$

$$+ 2\overline{\left(\frac{\partial w}{\partial z}\right)^2} + \overline{\left(\frac{\partial w}{\partial x}\right)^2} + \overline{\left(\frac{\partial w}{\partial y}\right)^2} + 2\overline{\frac{\partial u}{\partial y}\frac{\partial v}{\partial x}} + 2\overline{\frac{\partial u}{\partial z}\frac{\partial w}{\partial x}} + 2\overline{\frac{\partial v}{\partial y}\frac{\partial w}{\partial y}}. \tag{3.14}$$

Thus, the TKED rate may be estimated from measured spatial gradients of the velocities of the flow.

## 3.2 Velocity Fields from PIV

### *3.2.1 Method*

In order to characterize the turbulent kinetic energy dissipation rate, $\varepsilon$, of the flow within the Rayleigh-Bénard convective tank, a Particle Image Velocimetry (PIV) system was employed as described in 2.3.1 (Fincham and Spedding 1997).

### *3.2.2 Measured Velocity Fields*

Particle image velocimetry measurements of a transect of the convective tank give a measure of the two-dimensional velocity flow field. Time-averaged speed flow fields determined from PIV velocity measurements, for a filter window size of 32x32 pixels (4 mm by 4 mm), are shown in Figure 3.1 (a) - (f) for Rayleigh numbers spanning the range of the current set of experiments: $Ra = 2.6*10^8 - 3.3*10^9$. The reasoning behind the chosen window size will be discussed in Section 3.3.2. These flow fields are consistent with observations of Xia *et al.* (2003). Namely, a lower velocity core is prevalent in the center of the tank, with higher velocity regions near the tank boundaries. As *Ra* increases, the higher velocity regions become more concentrated near the tank boundaries. The darker line extending from the upper boundary into the low-velocity core in the velocity field images is the shadow of a thermistor.

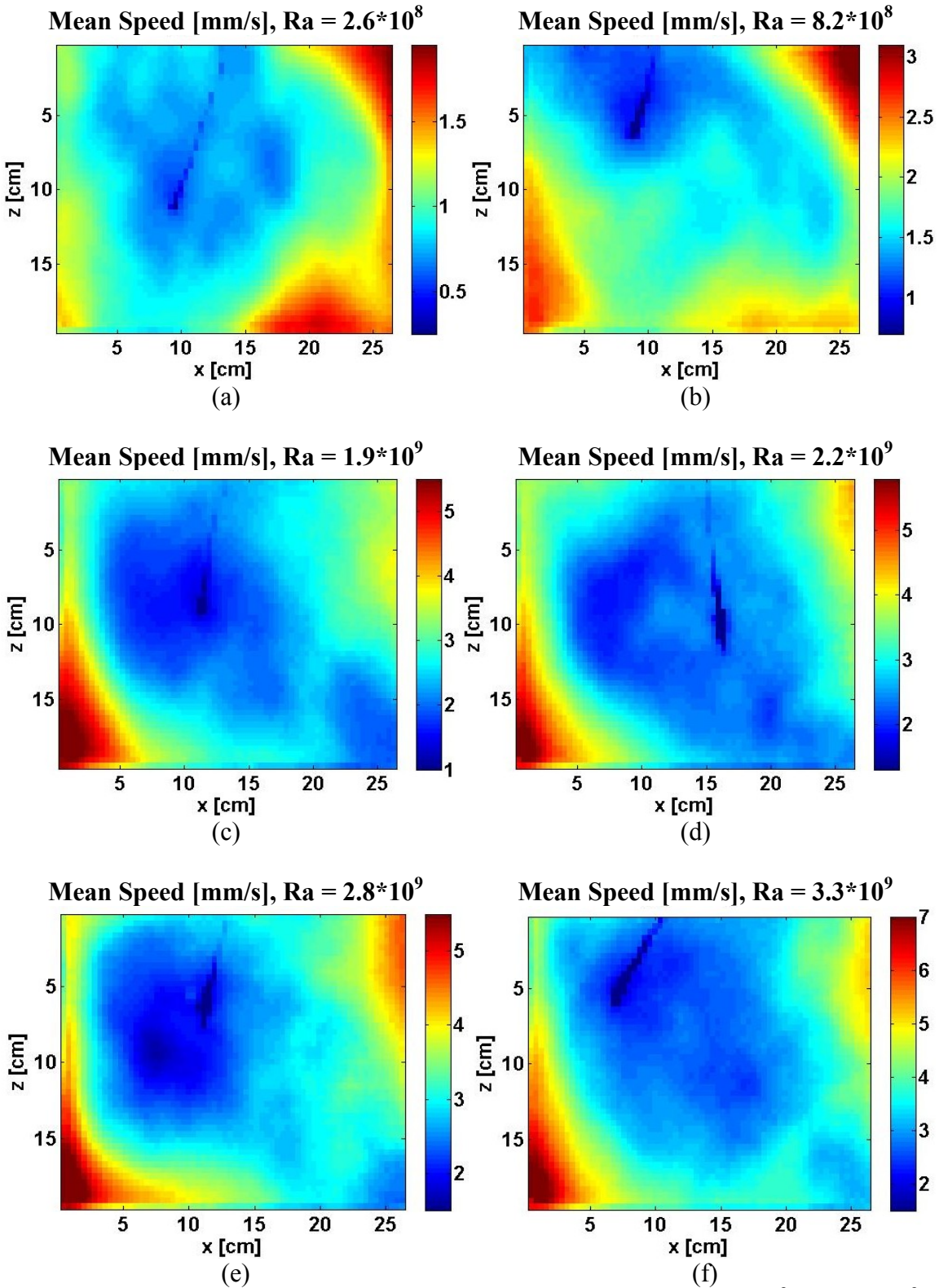


**Figure 3.1.** Time-averaged speed flow fields (mm/s) for (a) $Ra = 2.6*10^8$, (b) $8.2*10^8$, (c) $1.9*10^9$, (d) $2.2*10^9$, (e) $2.9*10^9$, and (f) $3.3*10^9$.

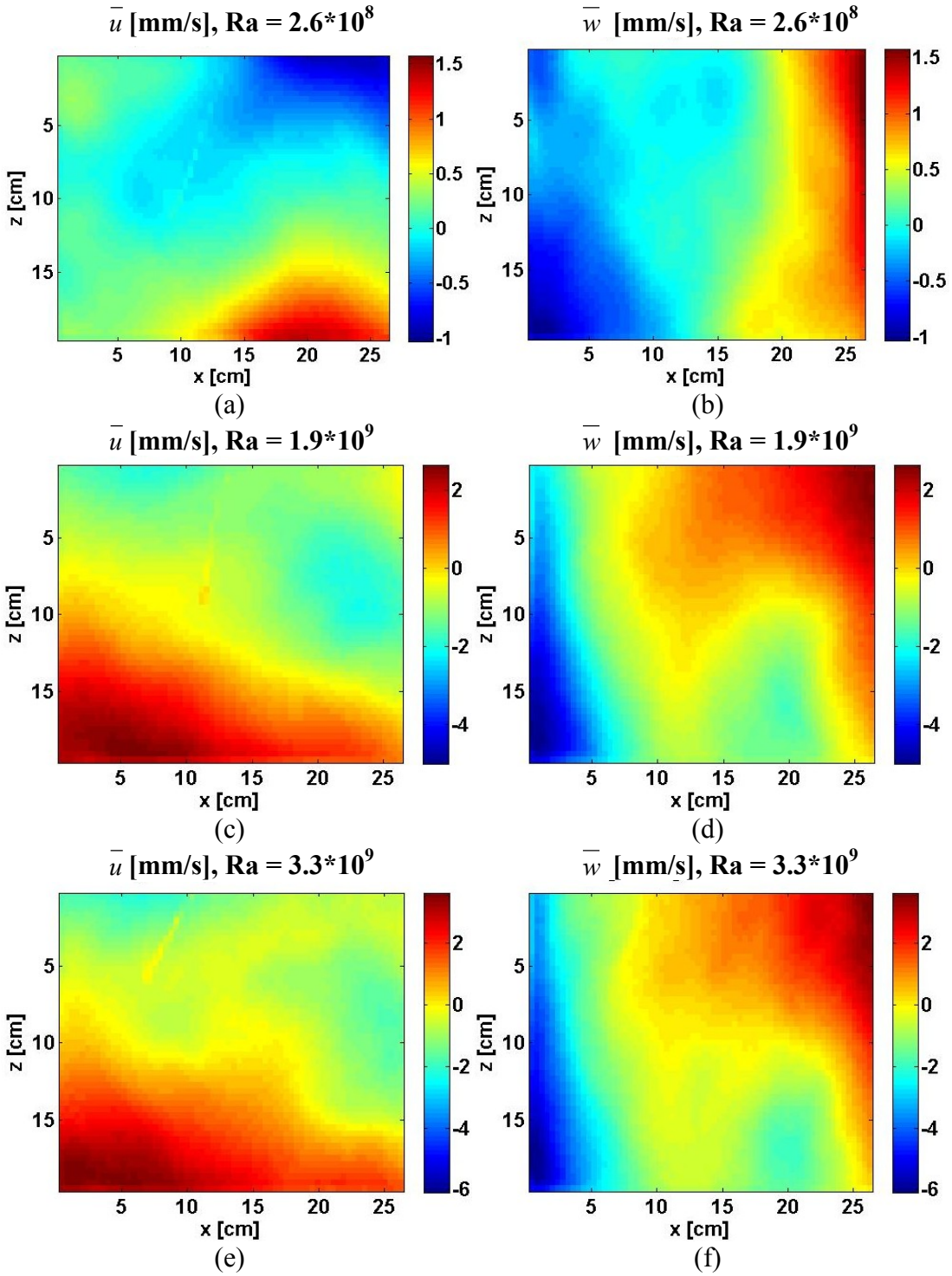


**Figure 3.2.** Time-averaged horizontal, $\bar{u}$, and vertical, $\bar{w}$, velocity flow fields (mm/s): (a) $\bar{u}$ for $Ra = 2.6*10^8$, (b) $\bar{w}$ for $Ra = 2.6*10^8$, (c) $\bar{u}$ for $Ra = 1.9*10^9$, (d) $\bar{w}$ for $Ra = 1.9*10^9$, (e) $\bar{u}$ for $Ra = 3.3*10^9$, and (f) $\bar{w}$ for $Ra = 3.3*10^9$. The linear feature visible in the top left of the plots (most notable in the $\bar{u}$ plots) is an artifact due to the thermistor.

The time-averaged horizontal, $\bar{u}$, and vertical, $\bar{w}$, velocities also demonstrate the rotational behavior of the flow, broken down into the thermal plumes which accumulate along the top and bottom plates before rising/falling along the sidewalls in the rotational flow. Figure 3.2 shows this behavior of $\bar{u}$ (left plots) and $\bar{w}$ (right plots) for progressively stronger turbulent flow.

The rms velocities were also calculated, and two vertical and horizontal transects of $u_{rms}$ (denoted by o marker) and $w_{rms}$ (denoted by x marker) through the approximate center of the PIV tank transect are shown in Figure 3.3. The top plots are for $Ra = 1.7*10^8$, and the lower plots for $Ra = 3.3*10^9$. The left-hand plots show horizontal transects near the x-axis, and the right-hand plots show vertical transects near the z-axis. The rms velocity transects are consistent with the time-averaged velocity fields, reaching a minimum near the tank center in the quieter, low-velocity core, and increasing nearer the boundaries. Locally, the rms velocities are within a factor of 3 near the boundaries, and a factor of 2 in the central region of the tank. In the central region, these rms velocities also exceed the average speeds. The flow may be considered locally isotropic when all averages related to the small scale structure of the flow are invariant to rotations or reflections of the coordinate system. Thus, while the velocities are not completely isotropic, especially near the boundaries, these observations suggest that at the small scales the flow field may be approximated as locally isotropic in the central region of the tank where the velocity fluctuations are equal within a factor of 2 and exceed the average speeds in the same region.

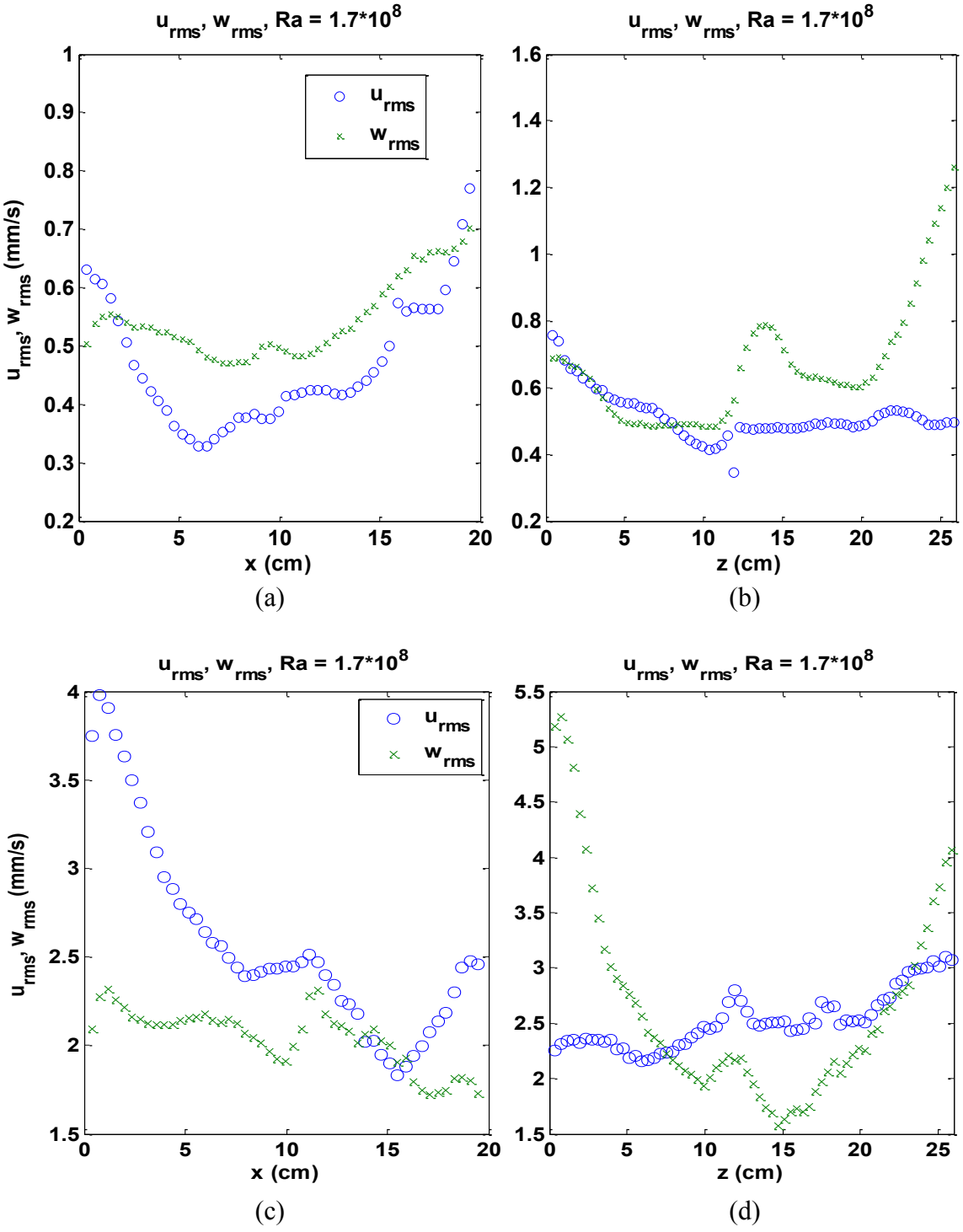


**Figure 3.3.** Vertical and horizontal transects of $u_{rms}$ (circles) and $w_{rms}$ (crosses) (mm/s) through the center of the tank for two strengths of turbulence: $Ra = 1.7*10^8$ (top panels) and $3.3*10^9$ (bottom panels). The left panels (a) and (c) are the velocity transects along the x-axis, and the right panels (b) and (d) are velocity transects along the z-axis.

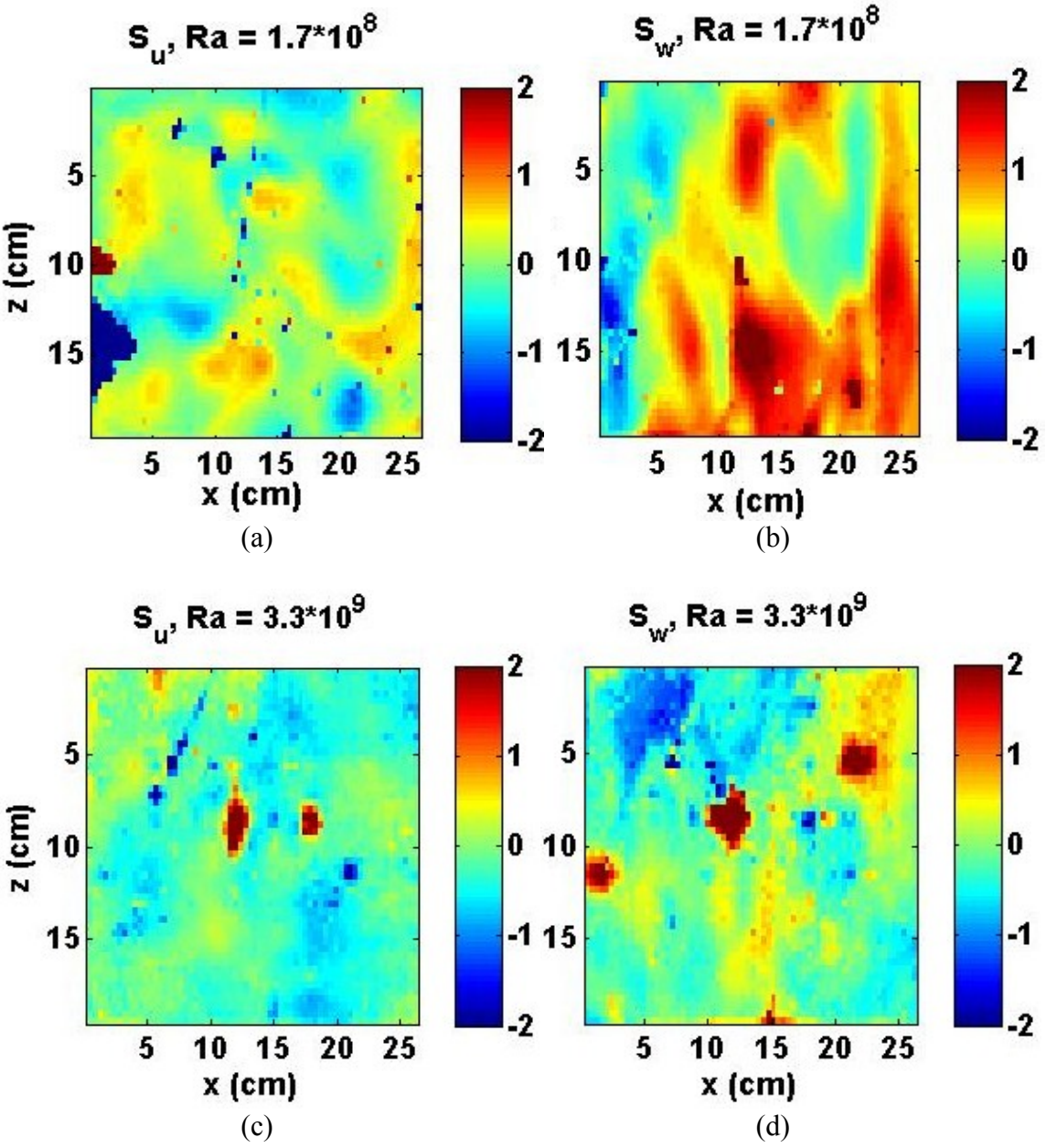


**Figure 3.4.** Velocity skewness fields for (a) horizontal velocity, $u$, and (b) vertical velocity, $w$, for $Ra = 1.7*10^8$ and (c) $u$ and (d) $w$ for $Ra = 3.3*10^9$.

The velocity flow fields have also been used to compute the velocity skewness from $S_u = \frac{\overline{u^3}}{u_{rms}^3}$ (Xia *et al.* 2003). The skewness describes the asymmetry of the velocity

fluctuations, and thus is a proxy for the homogeneity of the velocity fields. Skewness maps for $Ra = 1.7*10^8$ are shown in Figure 3.4 (a) for the horizontal velocities and (b) for the vertical velocities, and for $Ra = 3.3*10^9$ in (c) horizontal velocities and (d) vertical velocities. The regions of positive skewness indicate regions where larger positive velocities are more common than larger negative velocities, and negative skewness indicates regions where larger negative velocities are more frequent. While there is a lot of variation in the skewness at the lower turbulent strength (top panels), as *Ra* increases (lower panels), the skewness becomes somewhat less varied, and although variation is still present, the average magnitude of the skewness moves closer to zero, demonstrating increased symmetry in the magnitude of the velocity fluctuations.

## 3.3 Turbulent Kinetic Energy Dissipation Rates from PIV

### *3.3.1 Method*

With the velocity flow fields resolved by PIV, estimates of the TKED rate may then be obtained. In order to obtain the TKED rate from equation 3.14, the out of plane parameters (velocity and direction along the y-axis) must first be replaced with equivalent forms of the in-plane parameters (velocity and direction along the x-z plane). One term may be eliminated by squaring the averaged continuity equation given in 3.5, yielding:

$$\overline{\left(\frac{\partial v}{\partial y}\right)^2} = \overline{\left(\frac{\partial u}{\partial x}\right)^2} + \overline{\left(\frac{\partial w}{\partial z}\right)^2} + 2\overline{\frac{\partial u}{\partial x}\frac{\partial w}{\partial z}}. \tag{3.15}$$

In order to eliminate the additional out of plane components, local isotropy is assumed. Thus, all lateral fluctuations are taken to have similar average magnitudes:

$$\overline{\left(\frac{\partial u}{\partial y}\right)^2} = \overline{\left(\frac{\partial w}{\partial y}\right)^2} = \overline{\left(\frac{\partial v}{\partial x}\right)^2} = \overline{\left(\frac{\partial v}{\partial z}\right)^2} = \frac{1}{2}\overline{\left[\left(\frac{\partial u}{\partial z}\right)^2 + \left(\frac{\partial w}{\partial x}\right)^2\right]} \tag{3.16}$$

and

$$\overline{\left(\frac{\partial u}{\partial y}\frac{\partial v}{\partial x}\right)} = \overline{\left(\frac{\partial w}{\partial y}\frac{\partial v}{\partial z}\right)} = \overline{\left(\frac{\partial u}{\partial z}\frac{\partial w}{\partial x}\right)}. \tag{3.17}$$

Thus, substituting 3.15, 3.16, and 3.17 into 3.14 yields a form of equation 3.14 in terms of the measureable quantities *u*, *w*, *x*, and *z*.

$$\varepsilon = 3\nu\left\{\frac{4}{3}\left[\overline{\left(\frac{\partial u}{\partial x}\right)^2} + \overline{\left(\frac{\partial w}{\partial z}\right)^2} + \overline{\left(\frac{\partial u}{\partial x}\frac{\partial w}{\partial z}\right)}\right] + \overline{\left(\frac{\partial u}{\partial z}\right)^2} + \overline{\left(\frac{\partial w}{\partial x}\right)^2} + 2\overline{\left(\frac{\partial u}{\partial z}\frac{\partial w}{\partial x}\right)}\right\}. \tag{3.18}$$

Here, *v* is again the kinematic viscosity, *x* the horizontal direction along the axis of the PIV light sheet, *z* the vertical axis of the sheet, and *u* and *w* the corresponding horizontal and vertical velocities, respectively.

### *3.3.2 Turbulent Kinetic Energy Dissipation Rate Error Analysis*

#### *Window Filter Size*

In order to provide sufficient estimation of the TKED rate, care must be taken in choosing the window filter size used for cross correlation of the PIV images. Larger windows, such as 64 and 128 square pixels have sufficiently low noise levels, but poorer resolution, while smaller windows, such as 16 and 32 square pixels, provide measurement of the smaller relevant turbulent scales, but are also plagued by higher noise levels. Analysis was therefore carried out on all four window sizes to obtain the optimal TKED estimate, as described below.

The TKED rate estimate for each window size is used to compute the corresponding small scales of the flow field. Namely, $\eta$, the Kolmogorov length scale is computed from

$$\eta = \left( \frac{\nu^3}{\varepsilon} \right)^{1/4}, \tag{3.19}$$

and the corresponding Kolmogorov velocity from

$$\upsilon_k = (\nu\varepsilon)^{1/4}. \tag{3.20}$$

Following Saarenrinne *et al*. (2001), these parameters are then used to calculate the Helland and Van Atta turbulent dissipation spectrum (Helland *et al.* 1977):

$$\frac{2\nu(k\eta)^2}{\upsilon_k^3\eta^2} E(k) = \frac{2\nu(k\eta)^2}{\eta\upsilon_k} A \frac{L^{5/3}}{\eta} (kL^4)\left[1+(kL)^2\right]^{-17/6} \exp\left[ -\frac{3}{2} B(k\eta)^{4/3} \right]. \tag{3.21}$$

Here, $k$ is the range of wavenumbers resolved for a given PIV window size, $A$ and $B$ are experimentally determined parameters, with approximate values of 1.6 (Helland *et al.* 1977), and $L$ is the integral length scale, approximately half the width of the tank. The Helland and Van Atta energy spectrum is a combination of von Kármán's spectrum (Kármán 1948), describing the behavior for small to intermediate wavenumbers, and that of Pao (1965) for approximating the exponential decay of the spectrum over larger wavenumbers (Helland *et al.* 1977). The three-dimensional energy spectrum, $E(k)$ is related to the TKED rate by

$$\varepsilon = \int_0^\infty 2\nu k^2 E(k) dk \approx \int_{k\,\min}^{k\,\max} 2\nu k^2 E(k) dk \,. \tag{3.22}$$

Since the PIV window size determines the maximum and minimum resolved wavenumbers, the window size determines what portion of the spectrum is resolved,

defining the limits of the integrand in equation 3.22 for approximating the TKED rate. Thus, $k_{min}$ and $k_{max}$ should ideally span the full set of wavenumbers from zero to infinity.

A dissipation spectrum was found for each window size from equation 3.21. Each spectrum was then used to determine the percentage of total dissipation resolved by each PIV window size based on the resolved wavenumber range, and thus the resolved part of the spectrum. The dissipation spectra and corresponding cumulative distribution function, which shows what percentage of $\varepsilon$ has been resolved, are shown in Figure 3.5 by the solid and dash-dotted lines, respectively. The square and circular markers indicate the lowest and highest non-dimensional wavenumbers, respectively, resolved by each PIV window. Thus, the circular marker on the dash-dotted line, corresponding to the maximum wavenumber resolved by the PIV window size, indicates the portion of total energy dissipation resolved by that window size.

From this analysis, it was discovered that while the 128 and 64 square pixel windows (corresponding to 16 and 8 mm, respectively) had low noise levels, they resolved very small percentages of the total dissipation (21 and 48 %, respectively). A window size of 16 (2 mm), with notable noise levels in the velocity flow fields, resolved the highest percentage (95 %) of the total dissipation, but the lower noise levels of the 32 pixel (4 mm) window deemed it optimal for all PIV analysis, as it still resolved 80 % of the energy dissipation.

These observations are consistent with previous conclusions (Saarenrinne and Piirto 2000, Saarenrinne *et al.* 2001, Baldi and Yianneskis 2003) that a window size of approximately $2\eta_B$ is sufficient in resolving the small scales of the flow. After

determining the optimal window size for TKED rate estimation, the analysis was carried out for a full time series of images to yield a distribution of the temporally and spatially varying TKED rate at a discrete set of turbulent strengths.

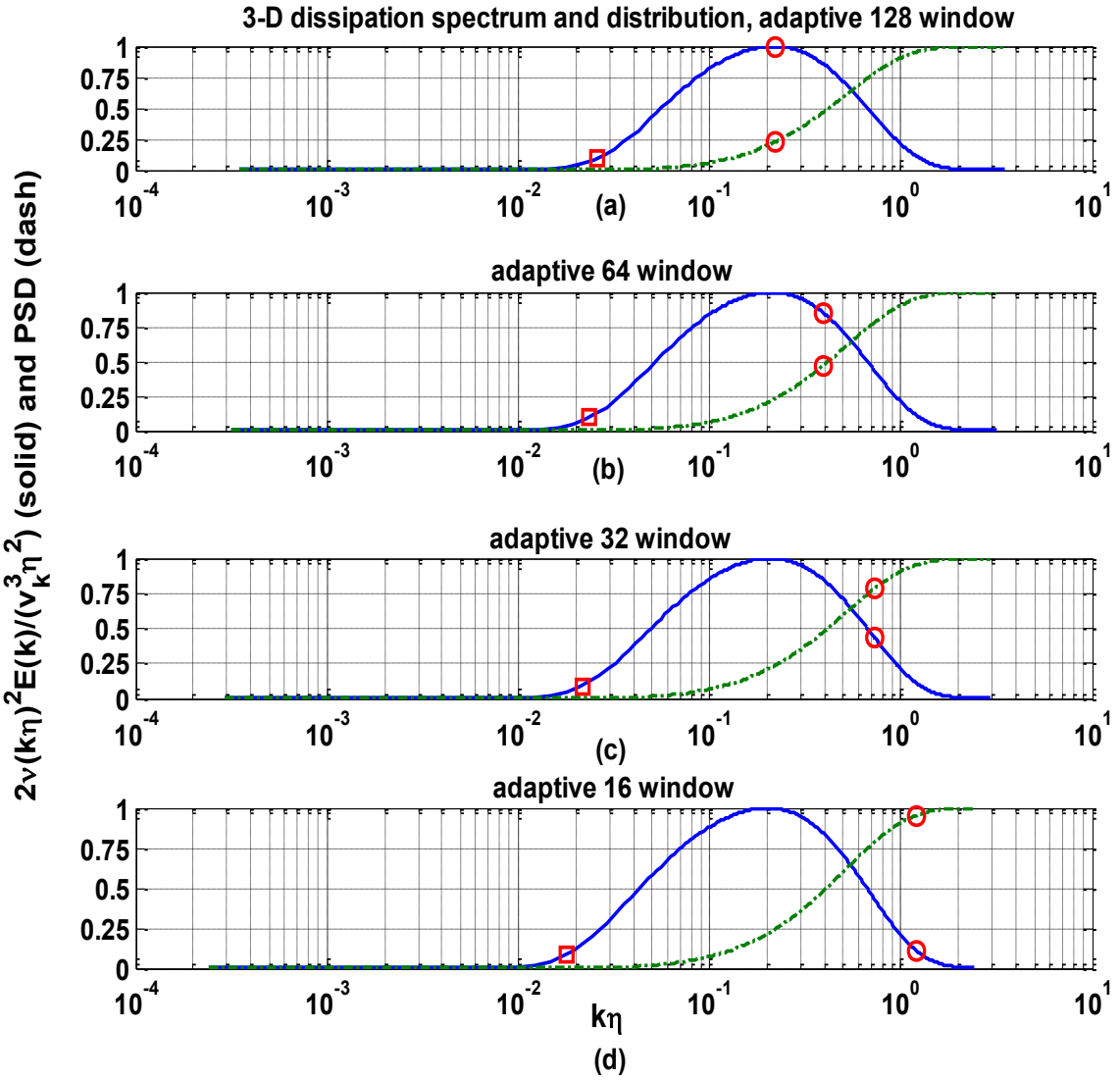


**Figure 3.5.** Normalized Helland and Van Atta turbulent dissipation spectrum (solid line) and corresponding cumulative distribution function (dash-dotted line), calculated for each PIV window size: (a) 128, (b) 64, (c) 32, and (d) 16 square pixels. The square and circular markers respectively represent the smallest and largest non-dimensional wavenumbers, $k\eta$, resolved by the given PIV window size.

## 3.4 Measured Turbulent Kinetic Energy Dissipation Rates

### *3.4.1 Temporally Averaged TKED Rates*

The characteristics of the time-averaged velocity flow behavior are mirrored in the time-averaged TKED rate fields, shown in Figure 3.6. The dissipation is weaker in the quieter core and increases near the boundaries across the higher velocity shear. Previous observations of a similar convective cell concluded that the time-averaged TKED rate has two main contributions: the thermal plumes that dominate the bulk region, and the mean temperature gradient that is concentrated in the thermal boundary layers, and which increases with increasing Rayleigh number (He *et al.* 2007). The results shown here are consistent with the first contribution. Additional experiments are needed to confirm the second contribution, however, as the thermal boundary layers near the top and bottom plates are outside the field of view of the PIV camera and thus are not apparent in the results presented here. The thermistor in the cell center and image borders have been masked for computation of the TKED rates.

Histograms of the full temporal and spatial distributions of the TKED rates shown in Figure 3.6, are plotted in Figure 3.7. These histograms were used to determine the logarithmic mean of the TKED rate as a function of turbulent strength. A summary of the TKED rates as a function of temperature difference across the tank and of Rayleigh number are shown in Figure 3.8. Thus, as the strength of turbulence in the tank increases, the rate of turbulent kinetic energy dissipation also increases. On a log-log scale, the increase in Rayleigh number of the flow is directly proportional to the increase in TKED rate.

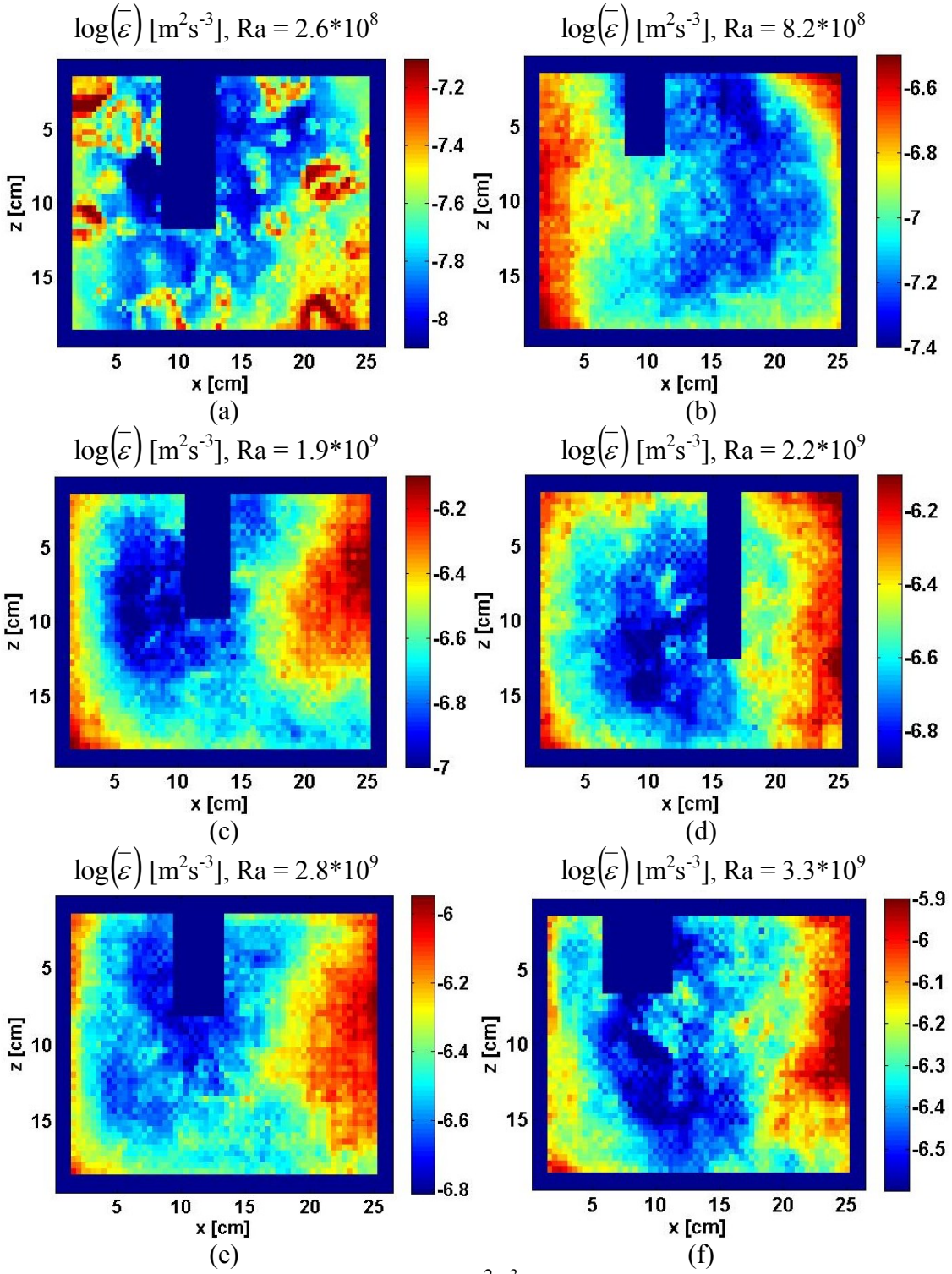


**Figure 3.6.** Time-averaged TKED rate (m$^2$s$^{-3}$) maps showing the spatial and temporal variations in $\varepsilon$ for a set of increasing turbulent strengths: (a) *Ra* = 2.6*10$^8$, (b) 8.2*10$^8$, (c) 1.9*10$^9$, (d) 2.2*10$^9$, (e) 2.9*10$^9$, and (f) 3.3*10$^9$, corresponding to the velocity flow fields shown in Figure 3.1.

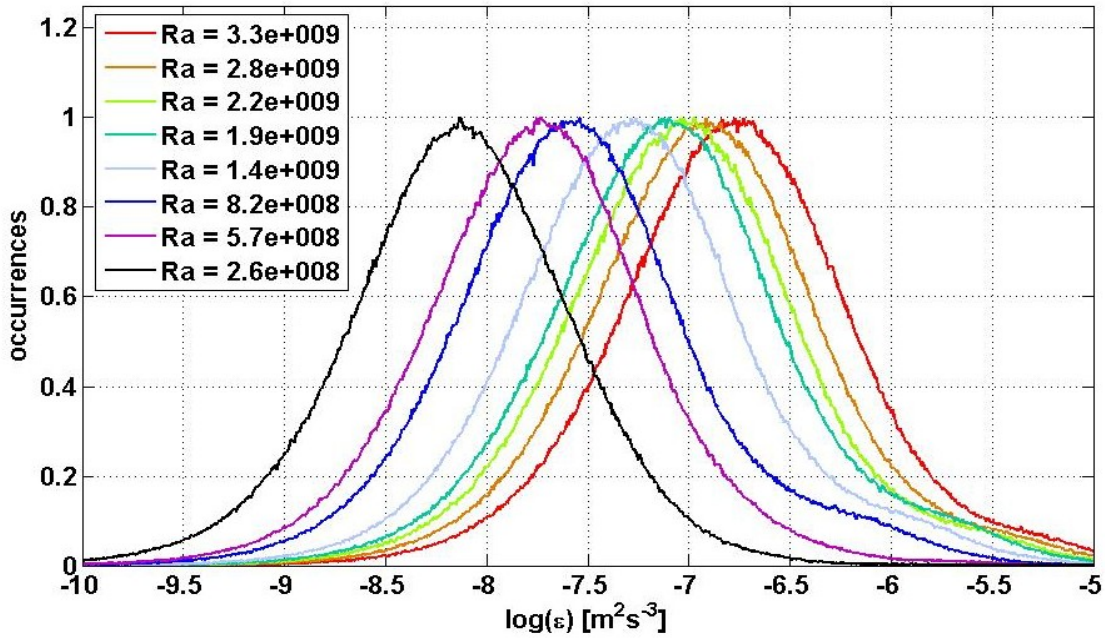


**Figure 3.7.** TKED rate histograms for a set of increasing turbulent strengths.

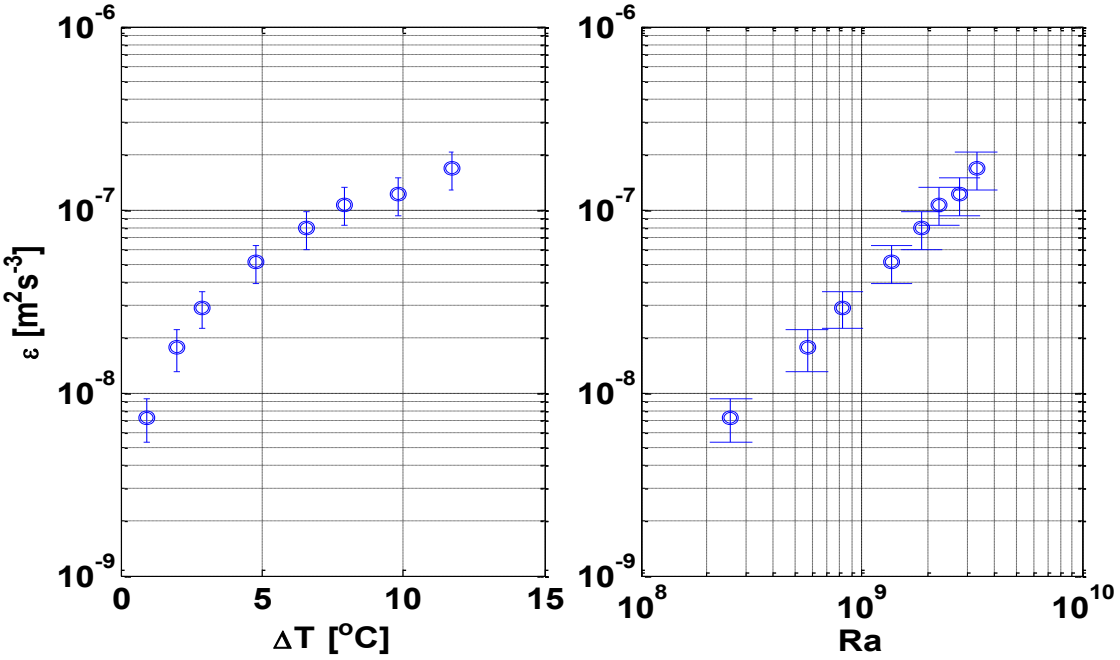


(a) (b)

**Figure 3.8.** Summary of experimental TKED rate, $\varepsilon$, obtained from PIV measurements, as a function of (a) tank temperature difference, $\Delta T$, and (b) Rayleigh number, $Ra$.

### *3.4.2 Intermittency of TKED Rates*

The velocity flow field and TKED rate field images used to compute the time-averaged images shown in Figures 3.1 and 3.6, were also put together as movies to observe the evolution of the velocity flow fields and energy dissipation rates with time. Clearly visible are the propagation of hairpin vortices and other such coherent structures of the flow (Zocchi *et al.* 1990, Hussain 1983). Also visible are bursts or strongly concentrated regions of energy dissipation. These bursts demonstrate the intermittency, or dynamic variations in time, of the turbulent flow not visible in the time-averaged flows described elsewhere (Xia *et al.* 2003). A few images showing the progression of such a burst are shown in Figure 3.9 for Ra = $2.8*10^9$.

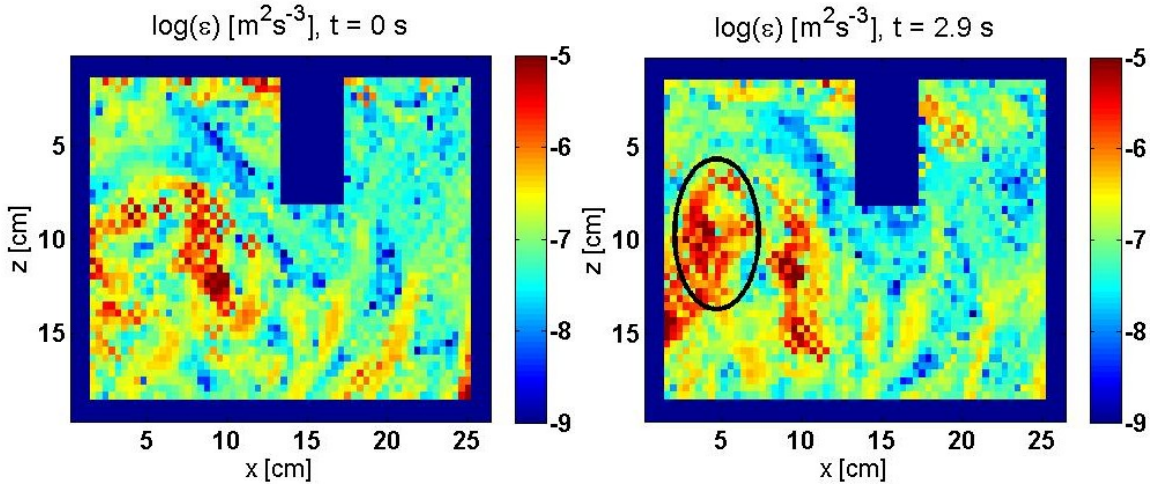


(a) (b)

**Figure 3.9** Continued on next page.

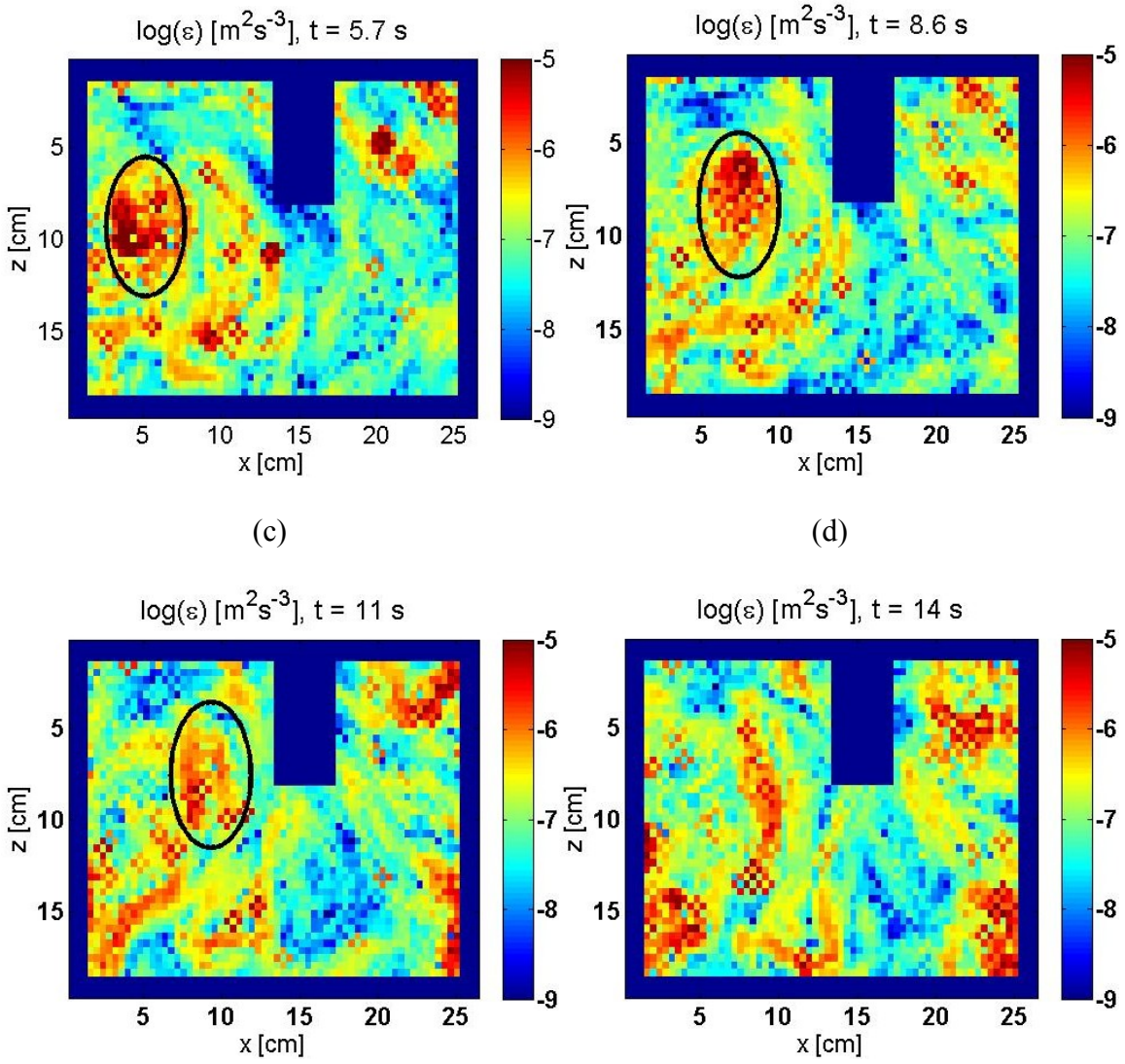


**Figure 3.9.** Temporal progression of a TKED rate burst, plotted in log($\varepsilon$) ($m^2s^{-3}$), in the PIV tank transect. (a) t = 0 s in burst progression, (b) t = 2.9 s, (c) t = 5.7 s, (d) t = 8.6 s, (e) t = 11 s, (f) t = 14 s.

## Chapter 4: Turbulent Thermal Dissipation Rate

### 4.1 Background

As mentioned previously, homogeneous and isotropic turbulent oceanic momentum and scalar fields are characterized at the smallest scales by two parameters: $\varepsilon$, the rate of dissipation of turbulent kinetic energy, which was the subject of Chapter 3, and $\chi_\theta$, the temperature variance dissipation rate, which will be the focus of the present chapter. The temperature variance dissipation rate, $\chi_\theta$, expresses the strength of the small scale temperature gradient within the flow, and thus indicates how quickly a temperature disturbance within the flow will be dissipated. Typically in oceanic measurements, $\chi_\theta$ ranges from $10^{-2}$ $^{o}C^{2}s^{-1}$ a few meters below the air-sea interface, in the more energetic part of the water column (Yang *et al.* 2003), to $10^{-10}$ $^{o}C^{2}s^{-1}$ in the more turbulently quiescent waters of the deep ocean (Hu *et al*. 1987).

In general, for homogeneous and isotropic turbulence, the temperature dissipation rate may be expressed as:

$$\chi_\theta = 6D_T\overline{\left(\frac{\partial T'}{\partial x}\right)^2} \tag{4.1a}$$

or

$$\chi_\theta = 6D_T\int_0^\infty S(k)dk\,. \tag{4.1b}$$

The overbar in equation 4.1a denotes a temporal average, $D_T$ is the thermal diffusivity, $T'$ the temperature fluctuation, $k$ the wavenumber, and $S(k)$ the theoretical one-dimensional Batchelor thermal gradient spectrum (Dillon and Caldwell 1980, Luketina and Imberger 2001). The one-dimensional Batchelor spectrum in equation (4.1b) is given by

$$S(k) = \chi_\theta \frac{\sqrt{2q}}{2k_B D_T} S_N(K). \tag{4.2}$$

Here, $q$ is a universal constant, taken to be $2(3^{1/2})$, as is commonly used in the literature (Dillon and Caldwell 1980, Luketina and Imberger 2001), $S_N(K)$ is the normalized spectrum, $K$ the dimensionless wavenumber, given by $K = \sqrt{2q}\, k/k_B$, and $k_B$ the Batchelor wavenumber, given by the inverse of the Batchelor length scale: $k_B = 1/\eta_B$.

The Batchelor length scale, $\eta_B$, represents the size of the smallest inhomogeneity of the temperature field, which is inversely proportional to the rate of dissipation of turbulent kinetic energy (TKED), $\varepsilon$:

$$\eta_B = \left( \frac{\nu D_T^2}{\varepsilon} \right)^{1/4}. \tag{4.3}$$

Here, $\nu$ is the kinematic viscosity, and $D_T$ the diffusivity of the fluid.

The normalized spectrum, $S_N(K)$ is given by

$$S_N(K) = K\left[ e^{-K^2/2} - K\int_K^\infty e^{-x^2/2} dx \right], \tag{4.4}$$

which may be approximated as (Luketina and Imberger 2001)

$$S_N(K) \approx K\left[ e^{-K^2/2} - \sqrt{2\pi} K Q(K) \right], \tag{4.5}$$

with

$$Q \approx \frac{1}{\sqrt{2\pi}} e^{-K^2/2} \left[0.319381530t - 0.356563782t^2 + 1.7814477937t^3 \right. \quad (4.6)$$

$$\left. - 1.821255978t^4 + 1.330274429t^5 \right]$$

and

$$t = \left(1 + 0.2316419K\right)^{-1}. \quad (4.7)$$

Utilizing the set of equations above, the turbulent thermal dissipation rate can be estimated from equation (4.1b).

## 4.2 Thermal Dissipation Rates from Profiling Thermistors

### *4.2.1 Method*

Utilizing a set of fast response thermistors connected to a motorized stage, as detailed in Chapter 2, spatial temperature profiles were obtained across a horizontal transect of the Rayleigh-Bénard convective cell. One hundred transects were measured for each turbulent strength. A few of the time-averaged temperature fluctuation profiles for a range of turbulent strengths between $Ra = 2.4*10^8$ and $3.4*10^9$ are plotted in Figure 4.1. These plots show the increase in magnitude of the temperature fluctuations with increasing Rayleigh number, as well as the increase in fluctuation magnitude between the quieter core and the flow nearer the boundaries of the cell.

The temperature fluctuation transects were then used to obtain the one-dimensional temperature gradient spectra. The one-dimensional thermal gradient energy spectrum, $E_\theta(k)$, is found by taking the Fourier transform of the spatial autocorrelation of the

temperature fluctuations. The dissipation spectrum, $D_\theta(k)$, is then found from $2\nu k^2 E_\theta(k)$. Sample measured spectra for $Ra = 3.3*10^9$ are shown in Figure 4.2.

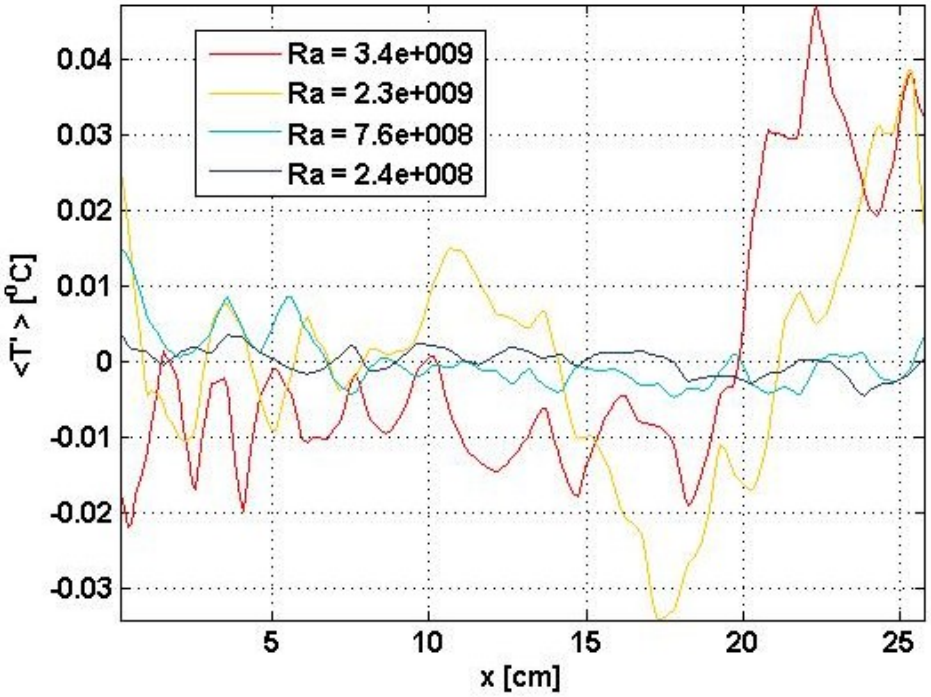


**Figure 4.1.** Time-averaged horizontal temperature profiles for a range of turbulent strengths from $Ra = 2.4*10^8$ (black line) to $3.4*10^9$ (red line).

These measured spectra were then fit with the Batchelor spectra from equation 4.2 (Luketina and Imberger 2001), which requires an initial estimate of the turbulent dissipation, $\chi_\theta$. Equation 4.1a was utilized for this initial estimate by differentiating each temperature transect, and averaging over all transects. Two sample transects of this estimate (for low and high turbulence strength), are plotted in Figure 4.3. These estimates were spatially averaged for use in calculations.

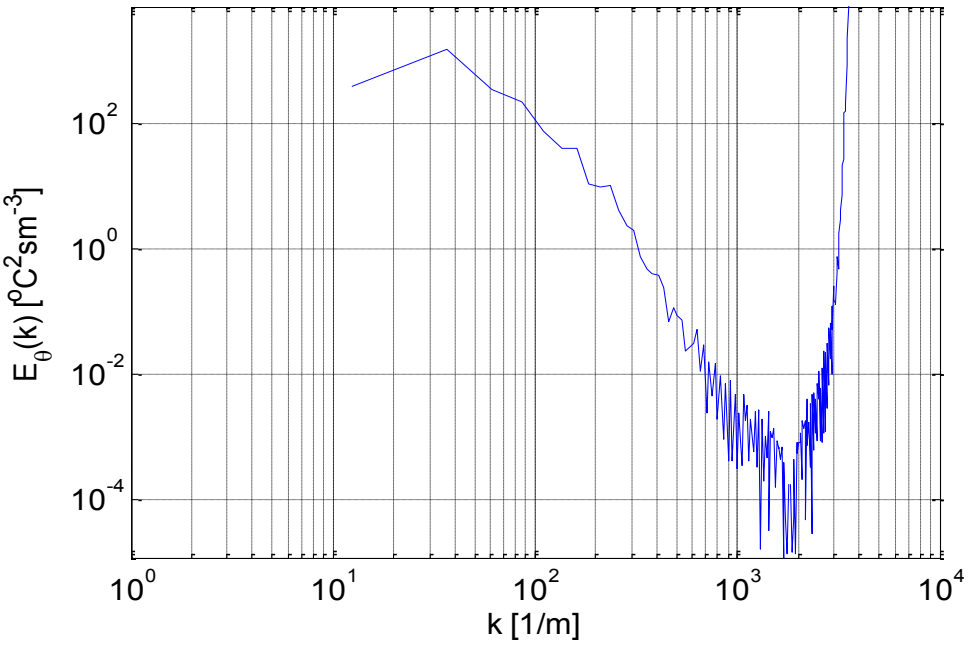


(a)

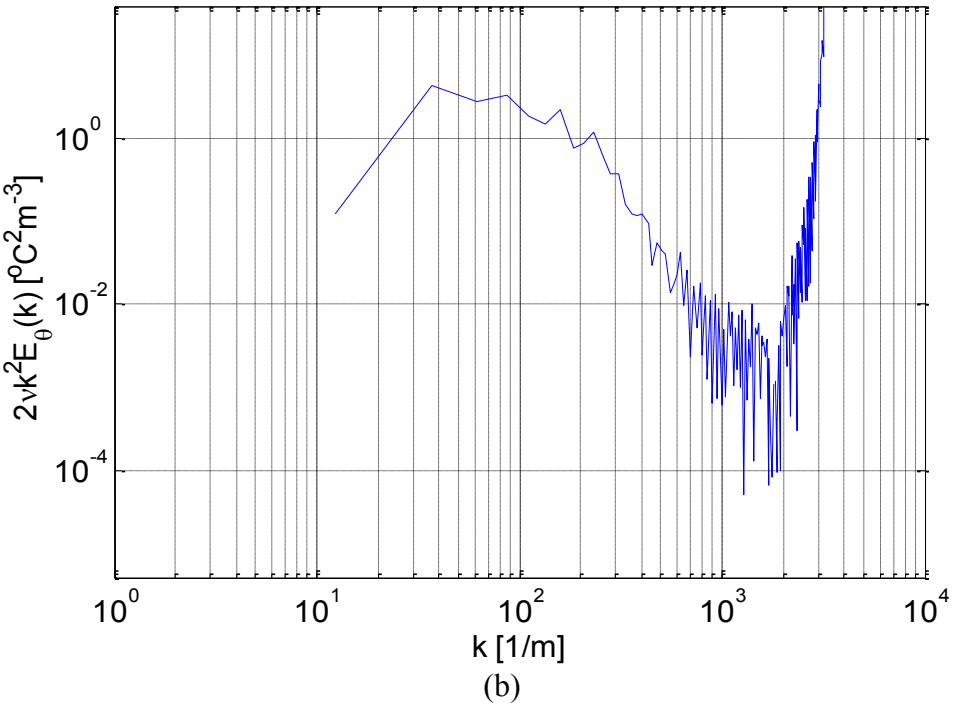


(b)

**Figure 4.2.** (a) Measured one-dimensional thermal gradient energy spectrum, $E_\theta(k)$, and (b) corresponding dissipation spectrum, $D_\theta(k) = 2\nu k^2 E_\theta(k)$ for $Ra = 3.3*10^9$.

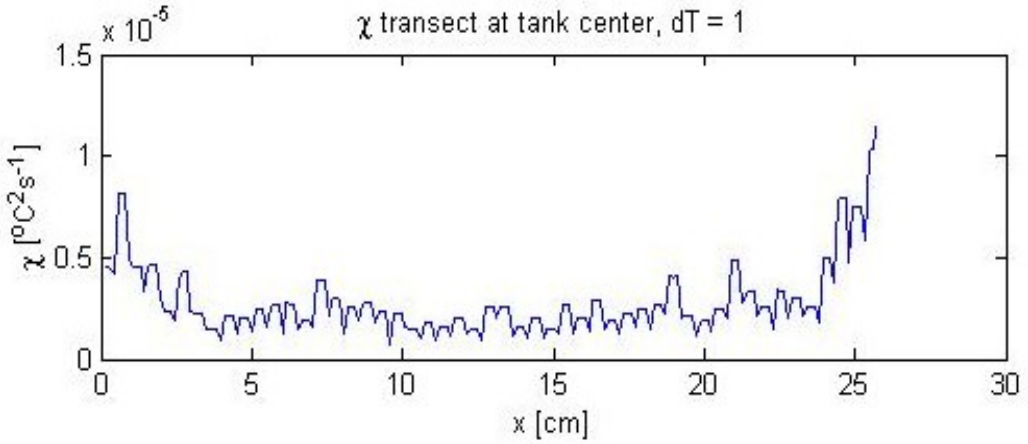


(a)

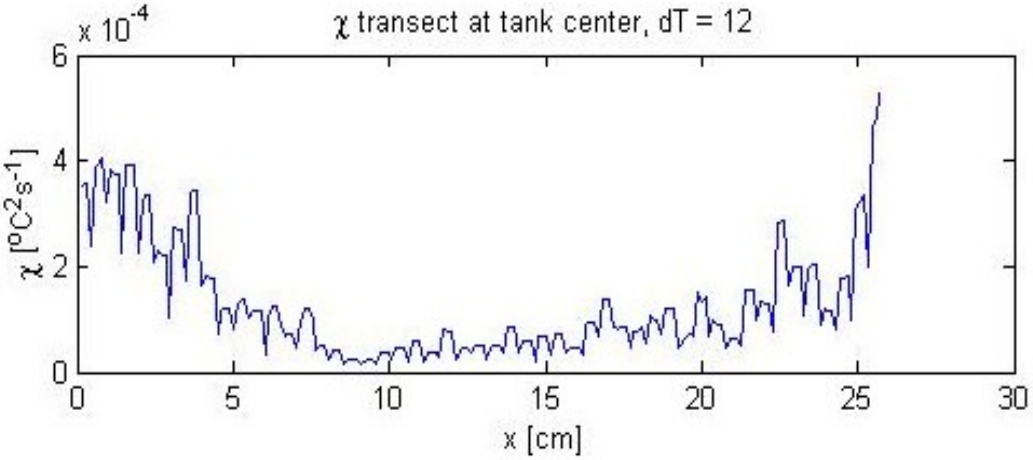


(b)

**Figure 4.3.** TD estimates from horizontal transects of temperature fluctuations for (a) $\Delta T = 1$ °C and (b) $\Delta T = 12$ °C. Note the change in vertical scale between (a) and (b).

The best fit spectrum was found by varying $k_B$, and thus varying the location of the maxima of $S(k)$, to minimize the error between the measured and theoretical spectra. Once the best fit was obtained, the spectra were averaged over all transects for a given turbulent strength. By fitting the Batchelor spectrum, $S(k)$, to the measured spectrum, equation 4.1b can be rewritten to estimate the thermal dissipation rate, $\chi_\theta$, by integrating over a combination of the measured spectrum, $D_\theta(k)$, and corresponding fit, $S(k)$:

$$\chi_\theta = 6D_T\left[\int_0^{k_L} S(k)dk + \int_{k_L}^{k_N} D_\theta(k)dk + \int_{k_N}^{\infty} S(k)dk\right], \tag{4.8}$$

where $k_L$ and $k_N$ are the lowest and highest of the range of wavenumbers over which $S(k)$ was fit to $D_\theta(k)$. The fitted spectra are provided in Section 4.3.

From the Batchelor wavenumber, used to maximize the fit between measured and theoretical spectra since $k_B$ determines the location of the maximum of $S(k)$, the turbulent kinetic energy dissipation rate may also be obtained from the fitted Batchelor spectra by replacing the Batchelor length scale with the Batchelor wavenumber $\left(\eta_B = 1/k_B\right)$ in equation (4.3) to yield the relation

$$\varepsilon = \nu D_t^2 k_B^4. \tag{4.9}$$

### *4.2.2 Thermistor Calibration and Error*

In order to provide accurate measurements of the temperature, all thermistors used in the tank setup were calibrated in a temperature stabilized waterbath against temperature measurements made from a Blackstack thermometer readout, providing accurate calibration to better than 0.001 K. uncertainty. This setup provides for accurate determination of the calibration curve of the thermistor, which determines the conversion from the resistance measured by the thermistors into the corresponding temperature, as shown in Figure 4.4.

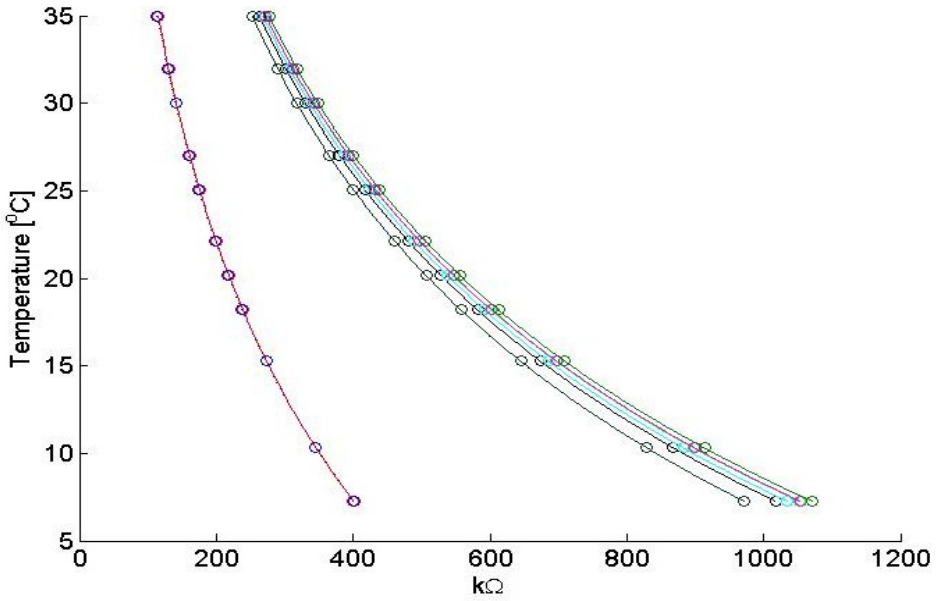


(a)

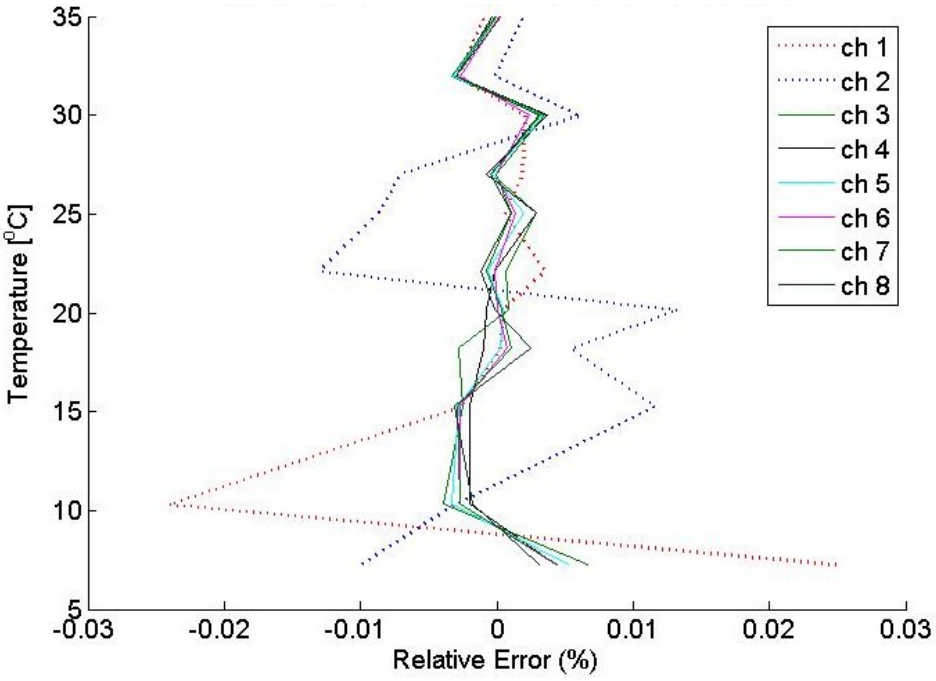


(b)

**Figure 4.4.** (a) Measured calibration curves for the fast (channels 1 and 2, dashed lines) and slow (channels 3 through 8, solid lines) thermistors used in the setup. The fast response thermistors (FP07) were used for determining the TD rate, slow thermistors were used to monitor the temperature at the top, middle, and bottom of the tank. (b) Corresponding error for each thermistor, relative to the temperature measured by the Blackstack, as a function of temperature (in K).

The two curves on the lefthand side of Figure 4.4 (a) (blue and red dashed lines) correspond to the fast response (FP07) thermistors (channels 1 and 2), and those on the righthand side of the plot to the slow thermistors (channels 3 through 8), used to monitor the temperature at the top, middle, and bottom of the convective cell. Figure 4.4 (b) shows the relative error in each thermistor measurement, compared to that of the Blackstack, as a function of temperature. Thus the error induced by the thermistor temperature measurement is very small.

### 4.3 Measured Thermal Dissipation Rates

The one-dimensional thermal gradient spectra determined from the measured temperature fluctuations (like that in Figure 4.1) and corresponding Batchelor spectra fits are presented in Figure 4.5 for several strengths of convective turbulence: (a) $Ra$ = $2.6*10^8$, (b) $8.2*10^8$, (c) $1.9*10^9$, and (d) $3.3*10^9$. The blue line is the measured dissipation spectrum, $D_\theta(k)$, the green line is the Batchelor fit, $S(k)$. The circles indicate the range of wavenumbers over which the measured spectrum has a Batchelor shape, and thus indicates the range of wavenumbers used for finding the fit.

Each dissipation spectra was used to determine the corresponding turbulent thermal dissipation rate. The TD rate was found by integrating the measured dissipation spectra over the measured wavenumber range, and using the fitted dissipation spectra to extend the integration to all wavenumbers, as expressed in equation 4.7.

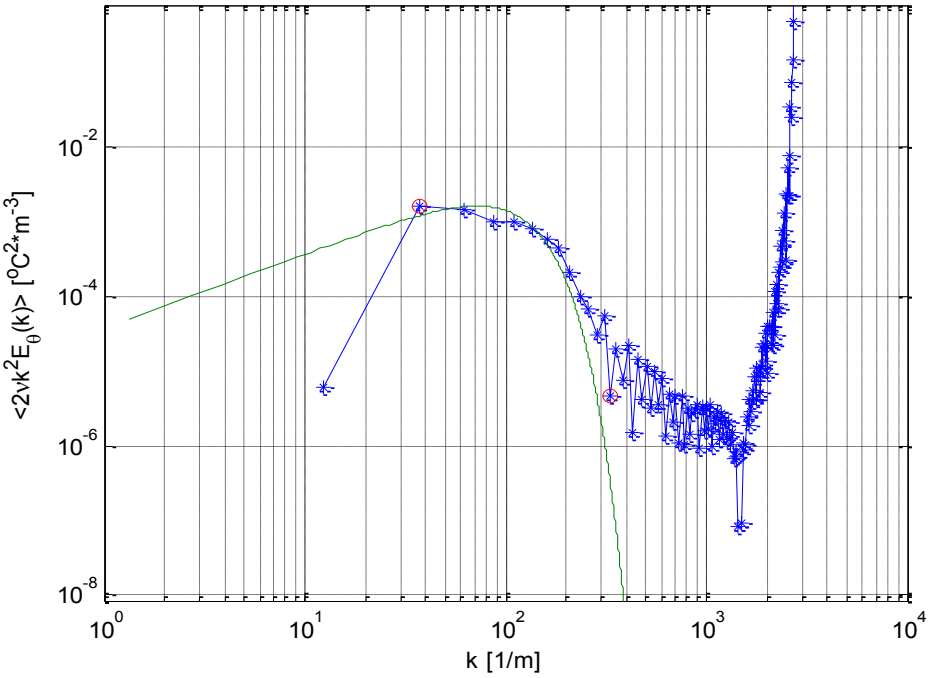


(a)

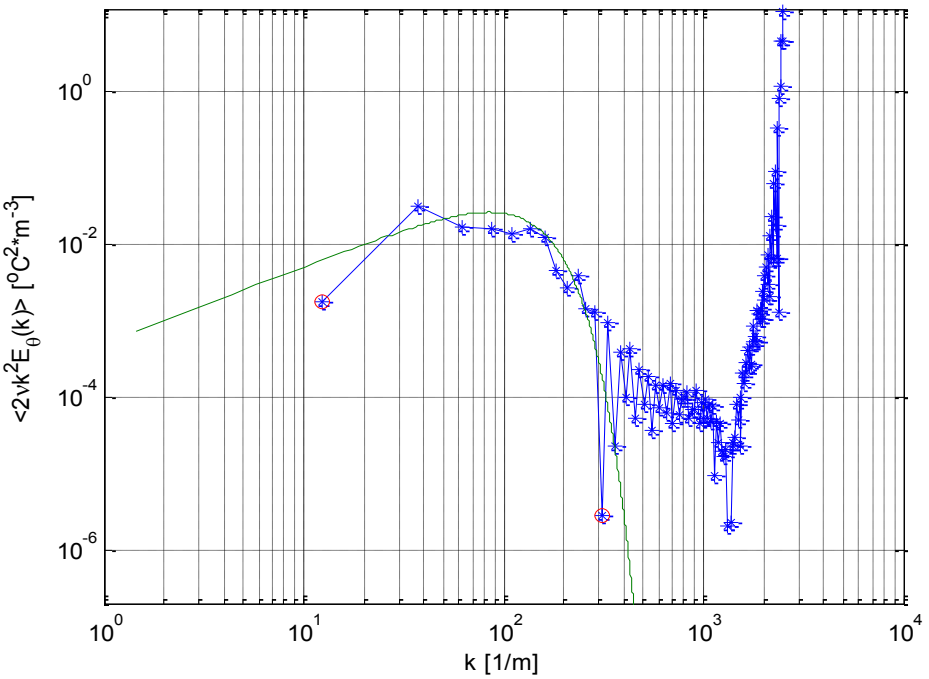


(b)

**Figure 4.5.** Continued on next page.

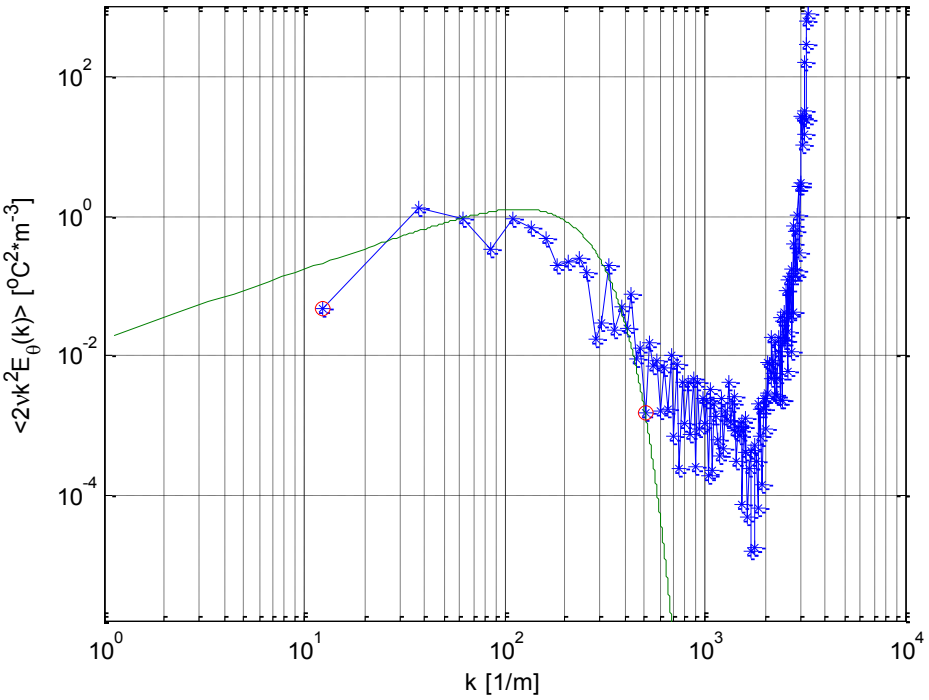


(c)

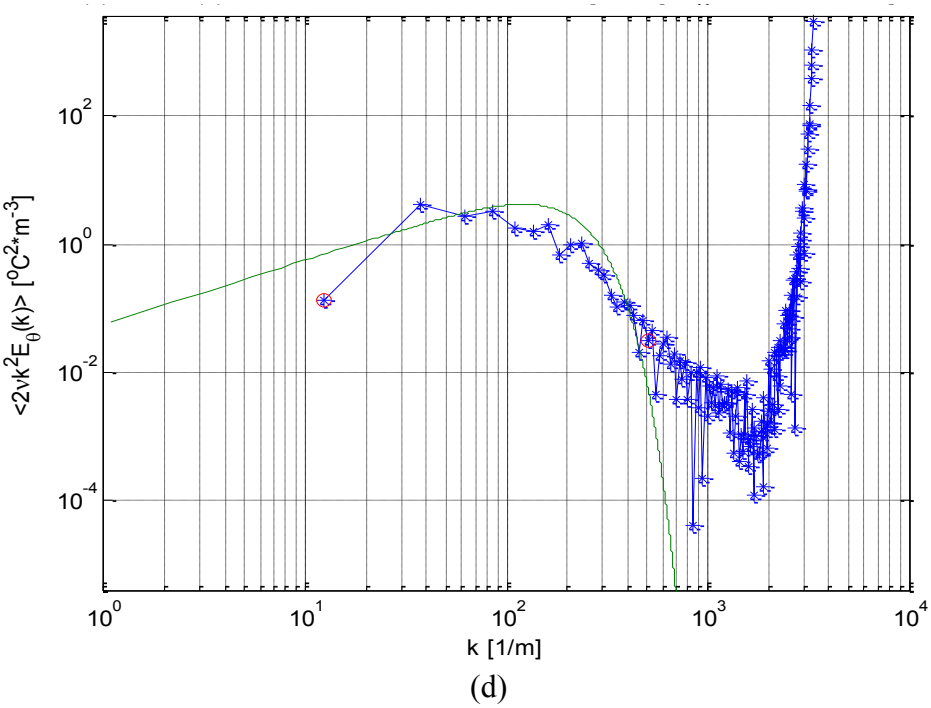


(d)

**Figure 4.5.** Measured one-dimensional temperature gradient spectra (blue line) and corresponding Batchelor spectra fit (green line) for (a) $Ra = 2.6*10^8$, (b) $8.2*10^8$, (c) $1.9*10^9$, and (d) $3.3*10^9$.

A summary of the TD rates over the range of turbulent strengths observed in the convective tank is provided in Figure 4.6 (blue circles). Also plotted in Figure 4.6 (red asterisks) are the initial guesses of the TD rate, as determined from taking the spatial gradient of the temperature transect using equation 4.1a. The standard deviation on each estimate is indicated by the error bar. While both estimates indicate the increase in temperature dissipation rate with increasing Rayleigh number, obviously there is significant discrepancy between the two estimates. This is due, in part, to the limited resolution of temperature fluctuations by the profiling thermistor, and the high levels of noise inherent in the measurement. While there was a time delay between measurement profiles to allow any wake induced by the thermistors to subside, the length of this delay could also have some affect on the estimates.

The peak of the fitted dissipation spectra shown above in Figure 4.5 is determined by the corresponding Batchelor wavenumber, $k_B$. Thus, the Batchelor wavenumber corresponding to each fit was then used to calculate the corresponding turbulent kinetic energy dissipation rates from equation 4.9. These TKED estimates are summarized in Figure 4.7 along with the TKED rates determined from PIV measurements for comparison. In general, the TKED rates obtained from PIV and thermistor profiling are in good agreement, with the thermistor estimate falling within one standard deviation of the PIV estimates, except for the lowest measurement. The difference at the weaker turbulent strength is likely due to difficulty in fitting the peak of the measured spectra at this Rayleigh number.

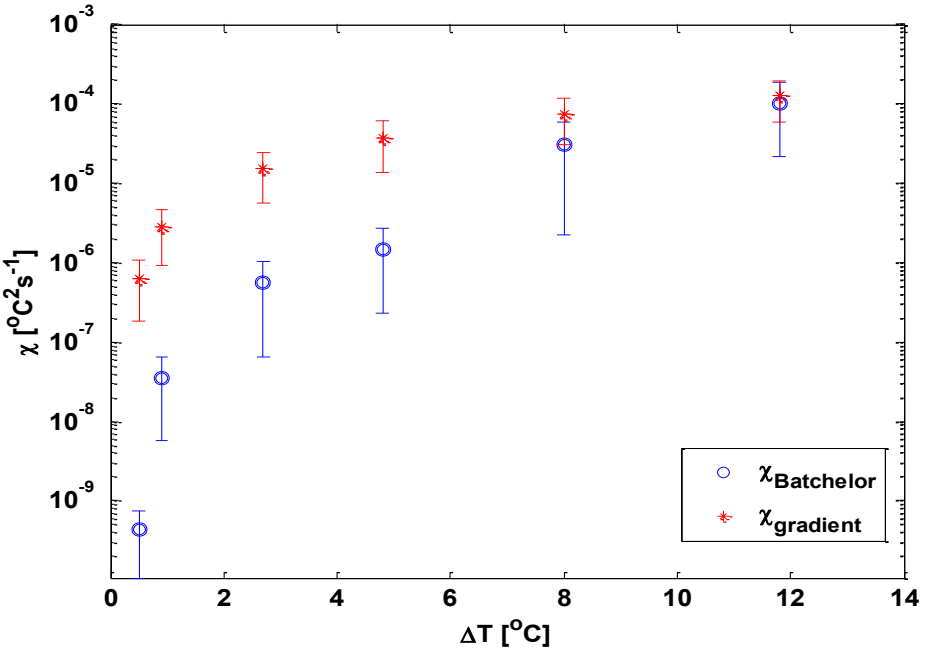


(a)

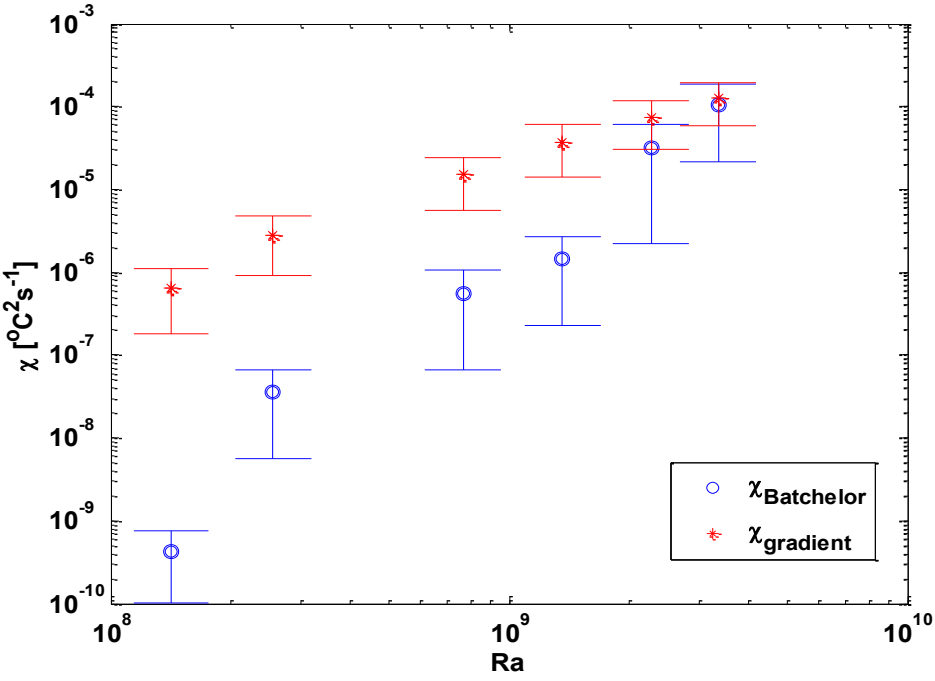


(b)

**Figure 4.6.** Summary of experimental TD rate, $\chi_\theta$, obtained from fitting theoretical Batchelor spectra to the measured temperature dissipation spectra (blue circles), and first estimate of $\chi_\theta$, obtained from the spatial gradient of temperature fluctuations given by equation (4.1a) (red asterisks) as a function of (a) tank temperature difference, $\Delta T$, and (b) Rayleigh number, $Ra$. Error bars denote one standard deviation of the mean TD rate.

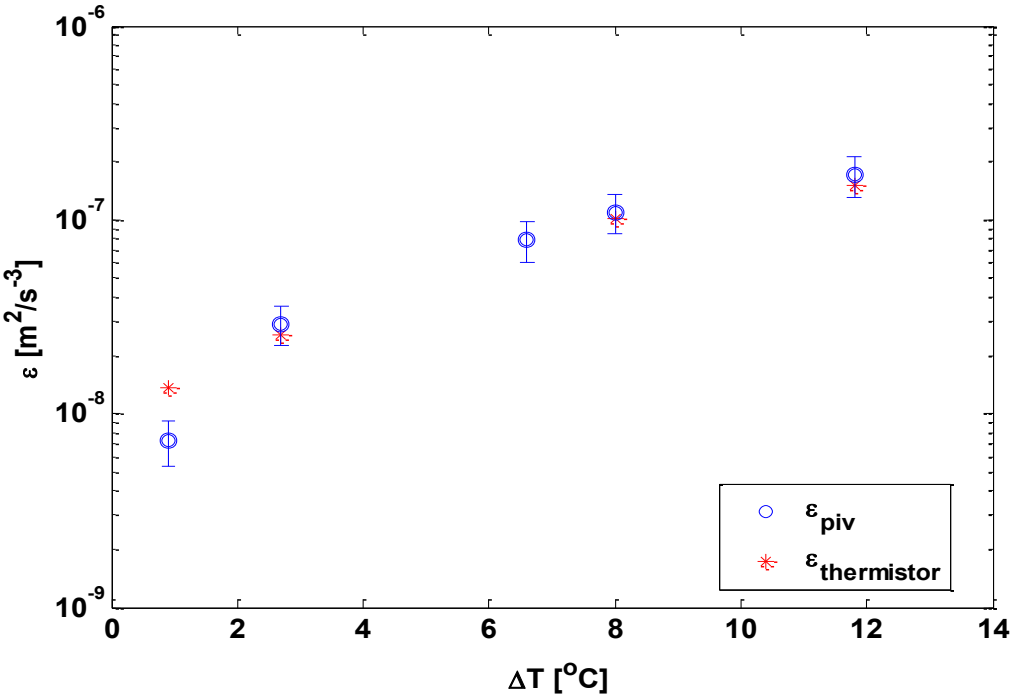


(a)

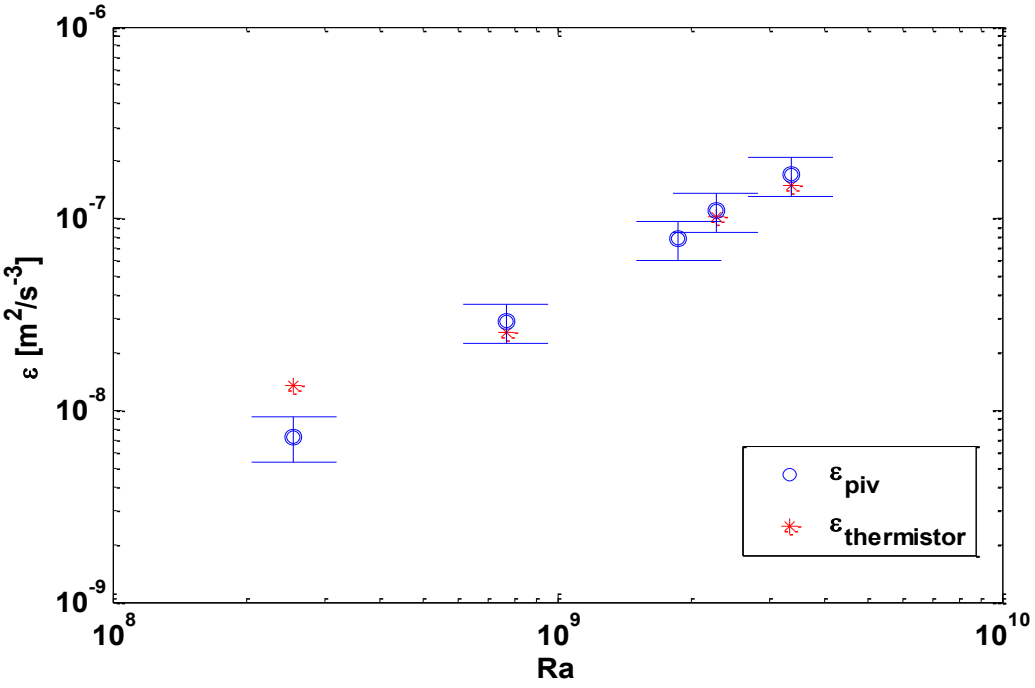


(b)

**Figure 4.7.** Summary of experimental TKED rate, $\varepsilon$, obtained from both PIV measurements (blue circles), and estimated from Batchelor curve fitting of the measured temperature gradient spectra (red asterisks) as a function of (a) tank temperature difference, $\Delta T$, and (b) Rayleigh number, $Ra$.

Figures 4.6 and 4.7 summarize the characterization of the turbulent flow within the Rayleigh-Bénard convective cell, with the temperature dissipation rate ranging from $2*10^{-9}$ to $4*10^{-4}$, and the kinetic energy dissipation rate ranging from $7*10^{-9}$ to $2*10^{-7}$ over a range of convective turbulent strengths with *Ra* between $2*10^{8}$ and $3*10^{9}$. Both the temperature dissipation and turbulent kinetic energy dissipation rates increase with increasing turbulent strength, demonstrating a near linear relationship with the non-dimensional Rayleigh number on a log-log scale.

## Chapter 5: Depolarization from Turbulent Flow

### 5.1 Background

For polarimetric applications, turbulent scattering has another important feature: turbulent scattering in the near-forward direction has been theoretically postulated to lower the polarization degree of the optical beam under the assumption of negligible absorption (Strohbehn 1968). While a single scattering event will often not depolarize a linearly polarized light beam, the multiple forward scattering events resulting from propagation through turbulence are enough to result in depolarization of the light beam (Kim and Moscoso 2001). The likely physical mechanism responsible for light beam depolarization on turbulence is described in Kim and Moscoso (2001). In particular, the mechanism for depolarization of linearly polarized light may be attributed to the randomization of the directional vector of the beam after several scattering events. In other words, the orientation of the plane containing the incident and scattered direction vectors of the first scattering event will be slightly perturbed after a few scattering events from turbulence, since the light will not always be scattered along the same plane. As the light continues to propagate, these perturbations will continue so that after several more scattering events, the orientation of these scattering planes will become randomized. Since the polarization direction is referenced to these scattering planes, the polarization direction will also become randomized, resulting in depolarization of the beam (Kim and Moscoso 2001).

The amount of linear depolarization is quantified by the depolarization rate, $\gamma$. Physically, the depolarization rate is the rate at which power from one polarization state is transferred into the orthogonal state. Measurements of the depolarization rate, $\gamma$, were

made for a range of turbulent strengths, corresponding to a range of temperature differences, $\Delta T$, across the Rayleigh-Bénard convective tank. This range of turbulent strengths is characterized by turbulent parameters in the ranges $10^{-9} < \varepsilon < 10^{-7}$ $m^2s^{-3}$ and $10^{-9} < \chi_\theta < 10^{-4}$ $^oC^2s^{-1}$, as described in Chapters 3 and 4. The turbulent scales determined by these parameters are important for optical measurements, as they determine the size of the index of refraction inhomogeneities, which scatter light in the near-forward direction. The ubiquitous nature of these turbulent inhomogeneities results in significant multiple forward scattering events at near-forward angles in the more energetic portions of the water column.

## 5.2 Depolarization Rate from Polarized Diffractometer

### *5.2.1 Method*

As described in Chapter 2, the polarized diffractometer setup allows for simultaneous observations of both the co- and cross-polarized powers of the HeNe laser beam up, as shown in Figure 2.12, for various strengths of turbulent flow. Care was taken to reduce the ambient light field by performing all measurements in a darkened room and minimizing ambient light sources from outside the room as well as from other instrumentation inside the room. A background image for each run was also measured to account for the presence of any remaining ambient light and background noise in the absence of the laser beam. The mean background image was obtained in the same manner as the measurement images, but without the laser. After subtracting the background measurement from the irradiance image obtained with the CCD camera, each

of these images was split in half to provide two images, one of the co-polarized irradiance, and one of the cross-polarized irradiance. To account for the absorptive filters used to match intensities of $P_C$ and $P_X$ on the CCD, the irradiances of each image were multiplied by the optical density of the filter used in obtaining the image. These optical densities were provided by the manufacturer. The irradiances of these two images were then summed over all pixels to provide respective measurements of the total irradiances of the two beams, $P_C$ and $P_X$, which were used to determine the depolarization rate, $\gamma$, as described in Section 5.2.3. The mean depolarization rate, $\bar{\gamma}$, was then calculated from time series of $\gamma$ composed from results provided by each image.

### *5.2.2 Exposure Time and CCD Calibration*

In order to minimize noise contamination in the depolarization measurements, the total background noise from the CCD, or total dark current, as a function of exposure time was investigated. As shown in Figure 5.1, it was found that the dark current remained constant with exposure time below about $10^{-3}$ seconds, but for longer exposure times, began to grow with exposure time. Thus, CCD exposure times were kept between $10^{-5}$ to $10^{-3}$ seconds. Absorptive filters were then used in the path of the laser beam in order to adjust the intensity of both beams to approximately the same maximum value, kept as high as possible to allow for a higher signal to noise ratio, while avoiding saturation at the intensity maximum.

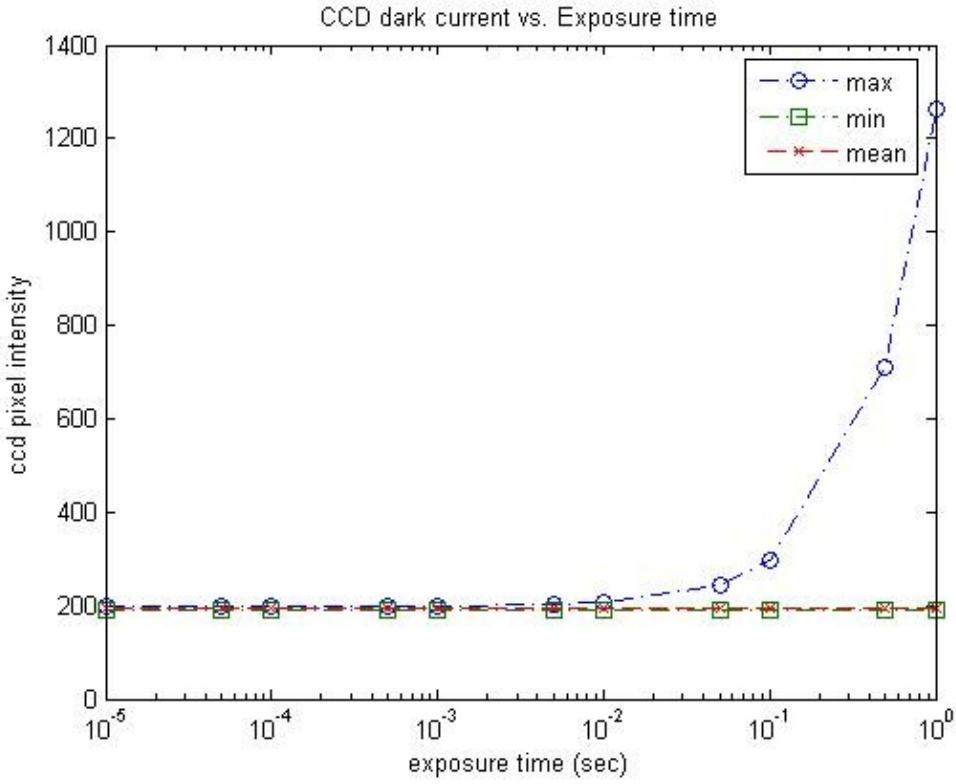


**Figure 5.1.** Measurement of the CCD dark current as a function of exposure time, in raw counts. While the mean noise level is constant in time, spikes in the noise occur at longer exposure times, thus the exposure times used in measurements were kept below $10^{-3}$ seconds.

Dark current noise contamination was also investigated on a per pixel basis in order to avoid image distortion due to CCD noise. An image of the CCD dark current noise per pixel, obtained with the camera cap closed, is shown in Figure 5.2, showing that while the difference in current noise between pixels is not large, spatial variation is still present. Since the dark curent noise and noise from background ambient light will both contaminate measurement images obtained with the CCD, and the dark current noise will be common to all images (both measurement and background), the CCD noise was not treated separately, but rather a series of background images were obtained for each

measurement run with the laser off and the CCD cap open, at the same exposure time as the measurement image. The average background image was then subracted from all measured images to account for background noise.

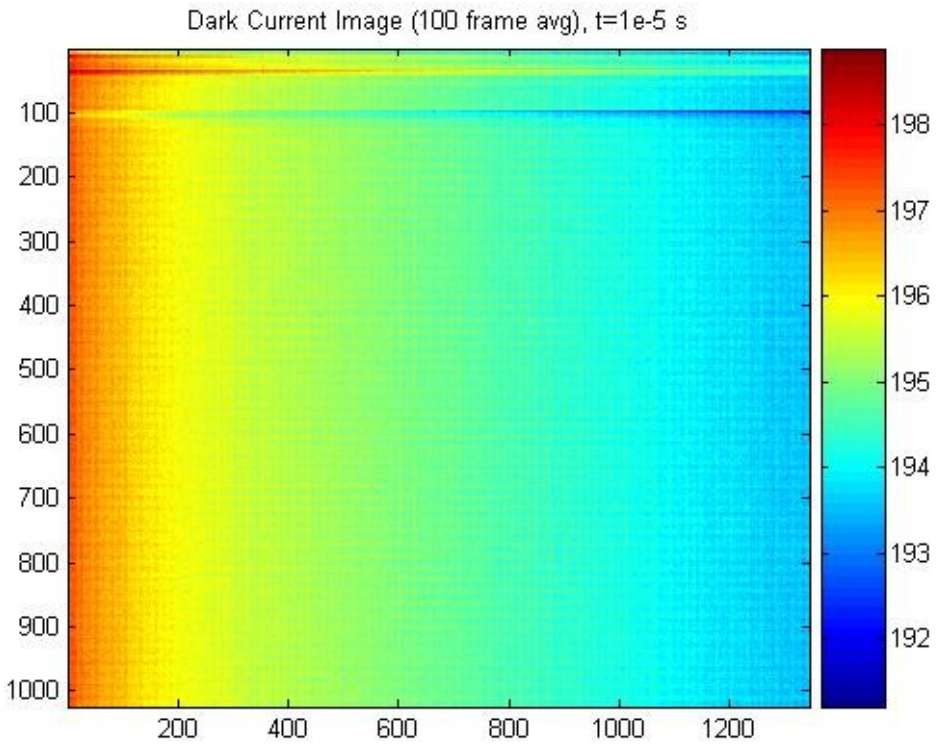


**Figure 5.2.** CCD Dark current image, showing the dark current per pixel in raw counts.

In order to calibrate the pixel response of the CCD, an incandescent bulb covered with a white diffusive coating was placed inside a box, whose interior walls were painted matte white. A window was cut in the side of the box, and a diffusive opal glass placed over the opening to create a uniform, diffuse light source spanning the field of view of the CCD camera. The calibration box was then placed directly in front of the CCD camera, as shown in Figure 5.3, and images of the incoming light from the box were obtained, giving the per pixel response of the CCD. The normalized calibration response

is shown in Figure 5.4. These differences in pixel readings are taken into account in the error analysis discussed in Section 5.2.4.

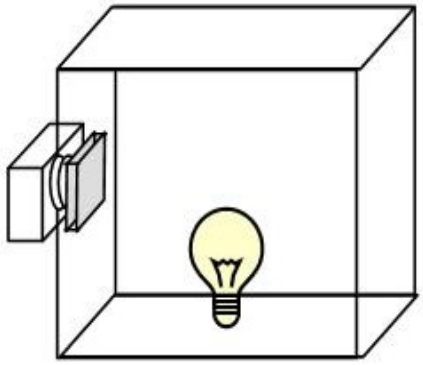

**Figure 5.3.** Setup for radiometric calibration of CCD: a white incandescent light bulb is placed inside a box whose inner walls are painted matte white. A window to the box is covered with a diffuse opal glass to create a diffuse, uniform light source spanning the field of view of the CCD camera, which is placed just in front of the opal glass window.

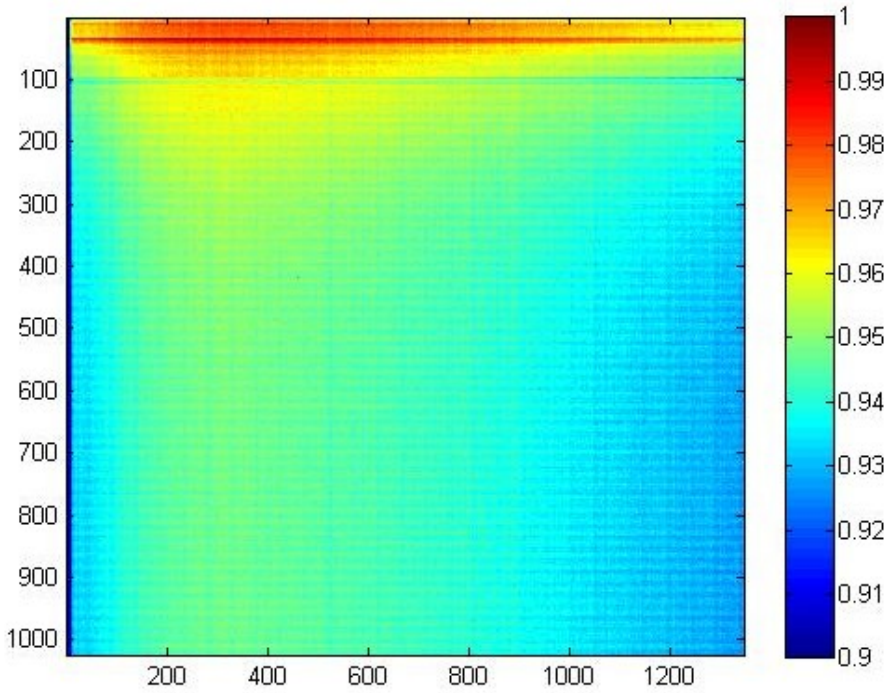


**Figure 5.4**. Normalized radiometric calibration image for the CCD camera.

### *5.2.3 Depolarization Rate*

The depolarization of the beam may be quantified by the depolarization rate, $\gamma$, which is the rate at which power is transferred between polarization states. This polarization characteristic can be obtained from lidar measurements, for which there are several definitions in the literature (Churnside 2008, Asano and Sato 1980, Bohren and Huffman 1983, Rojas-Ochoa *et al*. 2004). Given that the work presented here is oriented toward lidar applications, this work follows a definition used by Churnside (2008), where the power of an initially linearly polarized beam propagating through the water column is described by the following set of equations:

$$\begin{aligned} \frac{dP_C}{dz} &= -\alpha P_C + \gamma P_X \\ \frac{dP_X}{dz} &= -\alpha P_X + \gamma P_C \end{aligned} . \tag{5.1}$$

Here, $P_C$ and $P_X$ are the power of the beam in the co-polarized and orthogonally-polarized states, respectively, $z$ is the propagation depth, $\alpha$ the beam attenuation, and $\gamma$ the depolarization rate.

For a general case where the initial beam consists of both polarization states: $P_C = P_{CO}$ and $P_X = P_{XO}$ at $z = 0$, the solution to 5.1 is given by

$$\begin{aligned} P_C &= P_{CO} e^{-\alpha z} \cosh(\gamma z) + P_{XO} e^{-\alpha z} \sinh(\gamma z) \\ P_X &= P_{CO} e^{-\alpha z} \sinh(\gamma z) + P_{XO} e^{-\alpha z} \cosh(\gamma z) \end{aligned} . \tag{5.2}$$

Thus, as the initial beam propagates through the depolarizing medium, the intensity of both polarization states decays exponentially with depth scaled by the beam attenuation, $\alpha$, and the intensity of a particular state grows or decays as the beam is depolarized into the orthogonal polarization state. Thus, if one measures the power in

each polarization state at a given depth, it is possible to back out the depolarization rate of the propagation medium. By solving (5.2) for the depolarization rate, $\gamma$, one obtains:

$$\gamma = \frac{1}{2z}\left[\ln\left(\frac{P_{CO} - P_{XO}}{P_{CO} + P_{XO}}\right) + \ln\left(\frac{P_C + P_X}{P_C - P_X}\right)\right]. \tag{5.3}$$

The rate of depolarization thus depends upon the propagation depth, the initial degree of polarization of the beam, and the strength of the cross-polarized component of the beam relative to the co-polarized component.

Assuming an initially polarized beam such that $P_{CO} >> P_{XO}$, as in the case of a polarized lidar, and the case for the experiment presented here, the depolarization rate expressed in equation 5.3 may be simplified to

$$\gamma = \frac{1}{2z}\ln\left(\frac{P_C + P_X}{P_C - P_X}\right), \tag{5.4}$$

with the powers $P_C$ and $P_X$ from equation 5.2 similarly simplified to

$$\begin{aligned} P_C &= P_{CO}e^{-\alpha z}\cosh(\gamma z) \\ P_X &= P_{CO}e^{-\alpha z}\sinh(\gamma z) \end{aligned}. \tag{5.5}$$

The behavior of $P_C$ and $P_X$, with increasing depth, $z$, for two cases of varying depolarization strength is shown in Figure 5.5. Here, the assumed value of the beam attenuation coefficient, $\alpha = 0.1$ m$^{-1}$, corresponds to a typical open ocean value. Similarly, the values of the depolarization rate, $\gamma = 6\times10^{-3}$ (green lines) and $5\times10^{-4}$ m$^{-1}$ (blue lines), correspond to that observed for turbulent temperature and energy dissipation rates measured within the oceanic mixed layer. While these results are depth dependent and the experiment presented here is of a fixed depth, this illustrates the expected behavior of polarized light propagation in the ocean. The solid lines (overlying each other) show the

behavior of $P_C/P_{CO}$, which is nearly identical for the two cases. The dash-dotted lines show the behavior of $P_X/P_{CO}$, which is zero initially, and increases as light is scattered out of $P_C$ into $P_X$, undergoes exponential decay from attenuation, but is distinguished at a smaller rate than $P_C$, as its value gradually approaches that of $P_C$. The rate at which $P_X$ approaches $P_C$ is determined by the depolarization rate, $\gamma$.

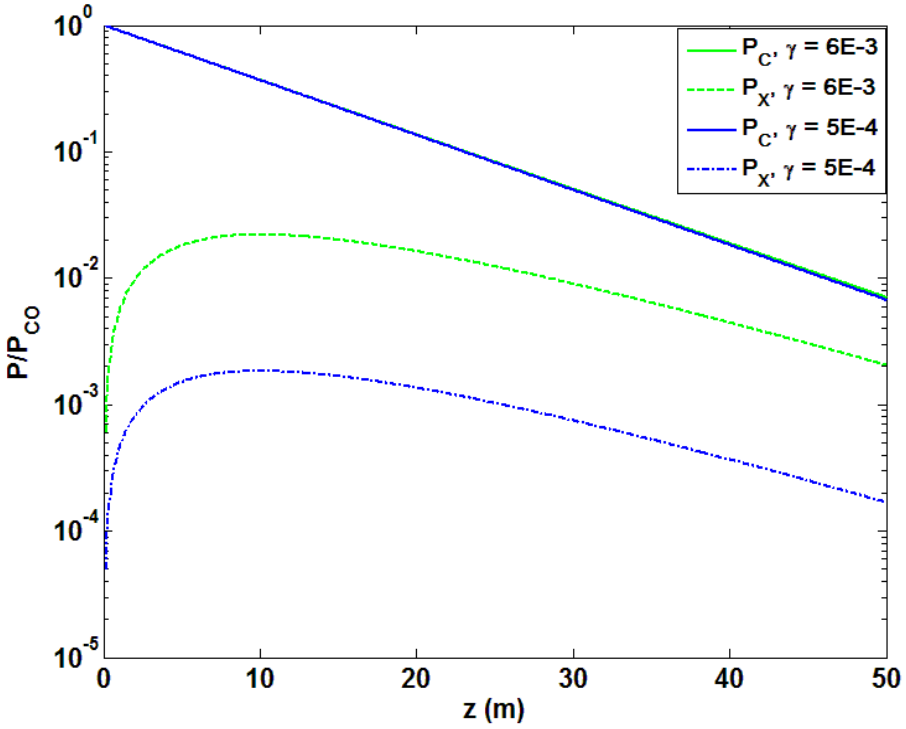


**Figure 5.5.** Depth dependence of the normalized co-polarized, $P_C$, (solid line) and cross-polarized, $P_X$, (dashed and dash-dotted lines) power of an initially polarized beam, with beam attenuation $\alpha = 0.1$ m$^{-1}$ and depolarization rate: $\gamma = 6\times10^{-3}$ (green lines) and $5\times10^{-4}$ m$^{-1}$ (blue lines), representative values of the oceanic mixed layer. Note that $P_C$ is nearly indistinguishable between the two cases.

Thus, by measuring the power in the orthogonal polarization states, $P_C$ and $P_X$, the depolarization rate may be obtained from equation 5.4.

### *5.2.4 Depolarization Rate Error Analysis*

The error on the calculated depolarization rate was found from measurement errors and further investigation of equation 5.3. Substituting $R_O = \frac{P_{CO}}{P_{XO}}$ and $R = \frac{P_C}{P_X}$ into equation 5.3,

$$\gamma = \frac{1}{2z}\left[\ln\left(\frac{R_O - 1}{R_O + 1}\right) + \ln\left(\frac{R+1}{R-1}\right)\right] \tag{5.6}$$

Taking the total derivative of 5.6 and dividing by γ, an expression can be obtained for the relative error on γ:

$$\frac{d\gamma}{\gamma} = \frac{1}{\gamma}\left(\frac{\partial\gamma}{\partial R_O}dR_O + \frac{\partial\gamma}{\partial R}dR\right). \tag{5.7}$$

Thus,

$$\frac{d\gamma}{\gamma} = \frac{2R_O}{\left(R_O^2 - 1\right)\left[\ln\left(\frac{R_O - 1}{R_O + 1}\right) + \ln\left(\frac{R+1}{R-1}\right)\right]}\frac{dR_O}{R_O}$$

$$- \frac{2R}{\left(R^2 - 1\right)\left[\ln\left(\frac{R_O - 1}{R_O + 1}\right) + \ln\left(\frac{R+1}{R-1}\right)\right]}\frac{dR}{R} \tag{5.8}$$

For the case of an initially polarized beam, $P_{XO} = \delta P_{CO}$, where $\delta << 1$, and substituting for $R_O = \frac{P_{CO}}{P_{XO}} = \frac{1}{\delta}$:

$$\left|\frac{d\gamma}{\gamma}\right| < \underbrace{\left|\frac{2\delta}{\left(1-\delta^2\right)\left[\ln\left(\frac{1-\delta}{1+\delta}\right)+\ln\left(\frac{R+1}{R-1}\right)\right]}\right|}_{A}\frac{dR_O}{R_O} + \underbrace{\left|\frac{-2R}{\left(R^2-1\right)\left[\ln\left(\frac{1-\delta}{1+\delta}\right)+\ln\left(\frac{R+1}{R-1}\right)\right]}\right|}_{B}\frac{dR}{R}. \quad (5.9)$$

Performing a coefficient analysis, A and B are expanded in a Taylor series about $\delta \to 0$:

$$A(\delta \to 0) = \frac{2\delta}{\ln\left(\frac{R+1}{R-1}\right)} + O\left(\delta^2\right) \quad (5.10a)$$

$$B(\delta \to 0) = \frac{-2R}{\left(R^2-1\right)}\left[\frac{1}{\ln\left(\frac{R+1}{R-1}\right)} + \frac{\delta}{\ln^2\left(\frac{R+1}{R-1}\right)} + O\left(\delta^2\right)\right] \quad (5.10b)$$

Substituting (5.10) into (5.9), to first order of $\delta$,

$$\left|\frac{d\gamma}{\gamma}\right| < \left|\frac{2\delta}{\ln\left(\frac{R+1}{R-1}\right)}\right|\frac{dR_O}{R_O} + \left|\frac{-2R}{\left(R^2-1\right)}\left[\frac{1}{\ln\left(\frac{R+1}{R-1}\right)} + \frac{\delta}{\ln^2\left(\frac{R+1}{R-1}\right)}\right]\right|\frac{dR}{R}. \quad (5.11)$$

For the present experiment, $\delta = O(10^{-7})$, so (5.11) simplifies to

$$\left|\frac{d\gamma}{\gamma}\right| < \left|\frac{-2R}{\left(R^2-1\right)\ln\left(\frac{R+1}{R-1}\right)}\right|\frac{dR}{R}, \quad (5.12)$$

From which the relative error on $\gamma$ can be estimated from measurement of $P_C$, $P_X$, and their associated errors. For the present experiment, the relative error on $\gamma$ was found to be less than 10%.

## 5.3 Measured Depolarization Rates

### *5.3.1 Averaged Depolarization Rates*

The experimentally observed values of the average depolarization rate, $\bar{\gamma}$, for clean water, over a range of turbulent flow strengths are shown in Figure 5.6 (a) as a function of Rayleigh number, and as a function of a representative product of turbulence parameters in Figure 5.6 (b). It should be noted that the scales of turbulent flows responsible for linear light depolarization are within the temperature viscous-dissipation range (Strohbehn 1968). Strohbehn (1968) shows that the variance of the depolarized light component, $\overline{|P_X|^2}$, can be expressed as: $\overline{|P_X|^2} \sim \int_0^\infty k^3 E_{3\theta}(k) dk$, where $E_{3\theta}(k)$ is the three dimensional temperature spectrum. This suggests that depolarization depends on the details of the temperature spectra between the Batchelor length scale, $\eta_B$, and the smallest existing length-scales of the scalar field, since the Batchelor length scale determines the location of the peak of the temperature spectra, and is related to the TKED rate by equation 4.3: $\eta_B = \left( \nu D_T^2 / \varepsilon \right)^{1/4}$.

Following Hodara (1966), the mean depolarization of an initially linearly polarized light beam over the length of the tank, $d$, can be evaluated as

$$\bar{\gamma} \sim \Delta T' \left( d / \eta_B \right)^{1/2}, \tag{5.13}$$

where $\Delta T'$ is the temperature difference at the Batchelor length scale, $\eta_B$. Using the dissipation range scaling, $\Delta T'$ can be estimated as:

$$\Delta T' = \left( \chi_\theta \big/ \nu \right)^{1/2} \eta_B . \tag{5.14}$$

Combined with the previous expression, the depolarization rate may be expressed in terms of the relevant turbulent parameters:

$$\bar{\gamma} \sim \left( \frac{\chi_\theta d \eta_B}{\nu} \right)^{1/2} . \tag{5.15}$$

Here, $\chi_\theta$ is the turbulent temperature dissipation rate, as determined in Chapter 4, and $\eta_B$ is the Batchelor length scale corresponding to the location of the peak of the fitted spectra used to determine the TD rate. These results are summarized in Figure 5.6 (b).

These measurements indicate that within the measured range of turbulent parameters, $\chi_\theta$ and $\varepsilon$, the forward depolarization rate, $\gamma$, varies between values smaller than $10^{-5}$ $m^{-1}$ for energetic flows, to around $3\times10^{-3}$ $m^{-1}$ for relatively quiescent flows. Following Churnside (2008) (Table 1), oceanic lidar measurements of the forward scattering depolarization rate yielded values of $5\times10^{-4}$ $m^{-1}$ in the energetic part of the transect to $1.63\times10^{-3}$ $m^{-1}$ in the offshore (likely less energetic) transect. Although the signal observed by Churnside (2008) was attributed to the possible depolarization of oceanic particles, the results presented here were conducted on purified drinking water in the absence of oceanic particles, and yet were of similar magnitude to that observed by polarimetric lidar, thus the signal may be attributed to turbulence. The results presented here are consistent with oceanic lidar observations and suggest that turbulent water column properties may be playing a significant role in polarimetric lidar returns.

The simple dimensional argument presented here demonstrates that there exists a relationship between the smallest turbulent flow parameters and the depolarization rate.

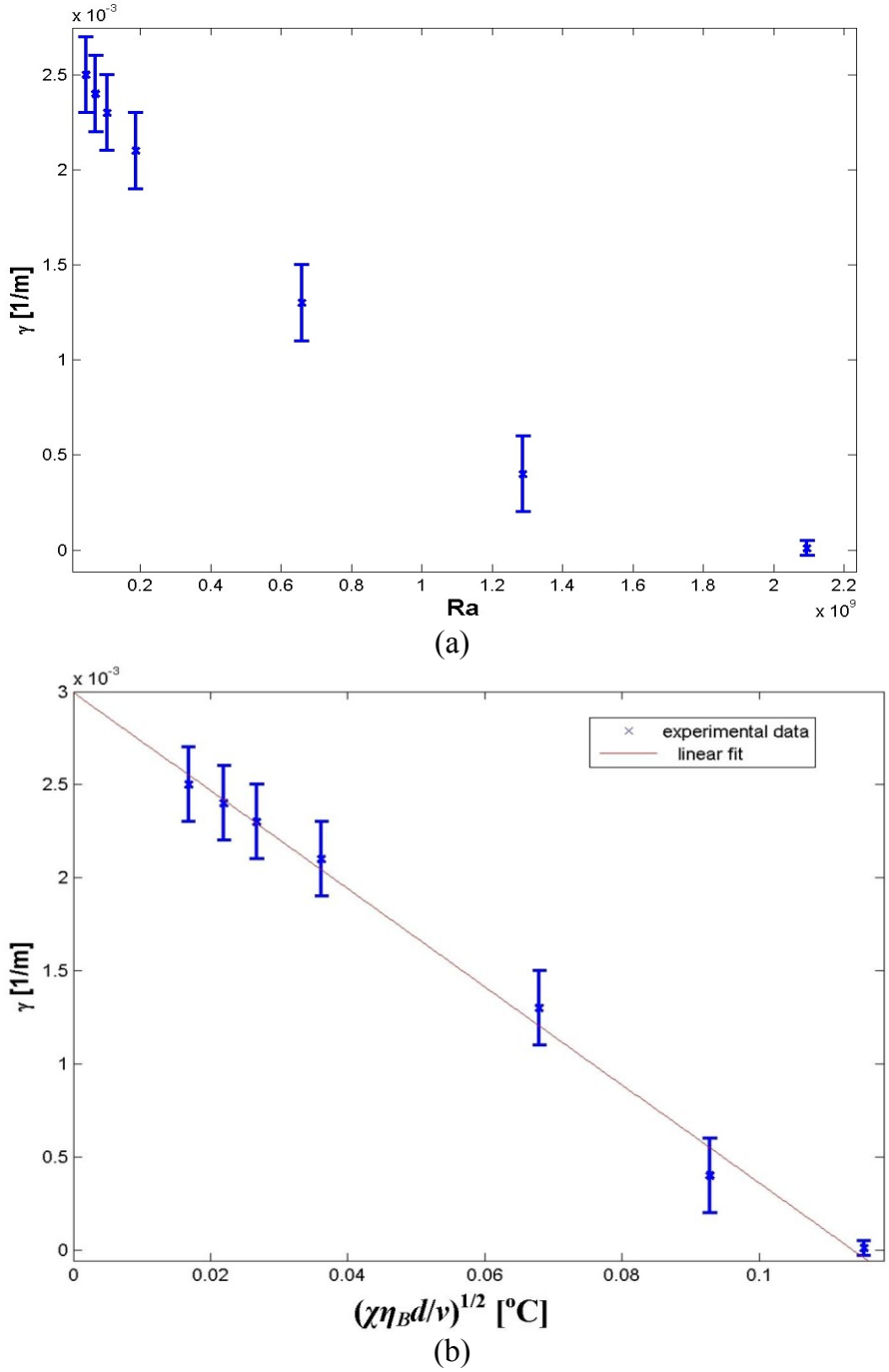


**Figure 5.6.** Experimentally measured mean depolarization rate, $\bar{\gamma}$, with error bars showing the standard deviation of the measurement, as a function of: (a) the Rayleigh number (x $10^9$) and (b) $(\chi d\eta_B/\nu)^{1/2}$, where $\chi$ is the thermal dissipation (TD) rate, $\nu$ the kinematic viscosity, and $\eta_B$ the Batchelor length scale of the turbulent flow. The line corresponds to a linear fit to the experimental data. The data were collected in a turbulent flow with pure water, over a range of turbulent strengths corresponding to values observed within the oceanic mixed layer.

As is demonstrated in Figure 5.6, as the turbulence strength increases, the depolarization rate decreases. This inverse relationship is likely the result of the direct proportionality between the depolarization rate and the Batchelor length scale, as evidenced in equation 5.15. As turbulence strength increases, the smallest length scales grow smaller (equation 4.3), and so too does the depolarization rate. While further study of the depolarization rate behavior under varying conditions is needed, the results presented here excitingly suggest that the depolarization rate may be a useful tool for inferring information about the small scale structure of a flow from non-invasive optical measurements. Clearly, a more detailed analysis is needed to account for parameters of the turbulent flow such as the temperature and energy spectra from within the viscous dissipation range.

### *5.3.2 Temporal Variation of Depolarization Rates*

As mentioned in Chapter 2, the cyclic variation of the optical parameters of the flow does not seem to match the frequency of the overturning circulation observed with the PIV. While the frequency of the core rotation observed in the velocity fields is on the order of minutes, the variation in the depolarization rate showed a much longer frequency, on the order of an hour, as shown in two time series of $\gamma$ in Figure 5.7, corresponding to one strong and one weaker case of turbulence, at a $\Delta T$ of (a) 1.6 $^{o}$C and (b) 11.7 $^{o}$C. This variation could be due to flow reversal or some other cyclic behavior of the flow not observed in the PIV velocity fields, as they were limited in the total acquisition length, and thus observations were carried for much shorter time periods. At

the present time, more measurements need to be conducted to determine the cause of this discrepancy between representative cyclic frequencies of the flow.

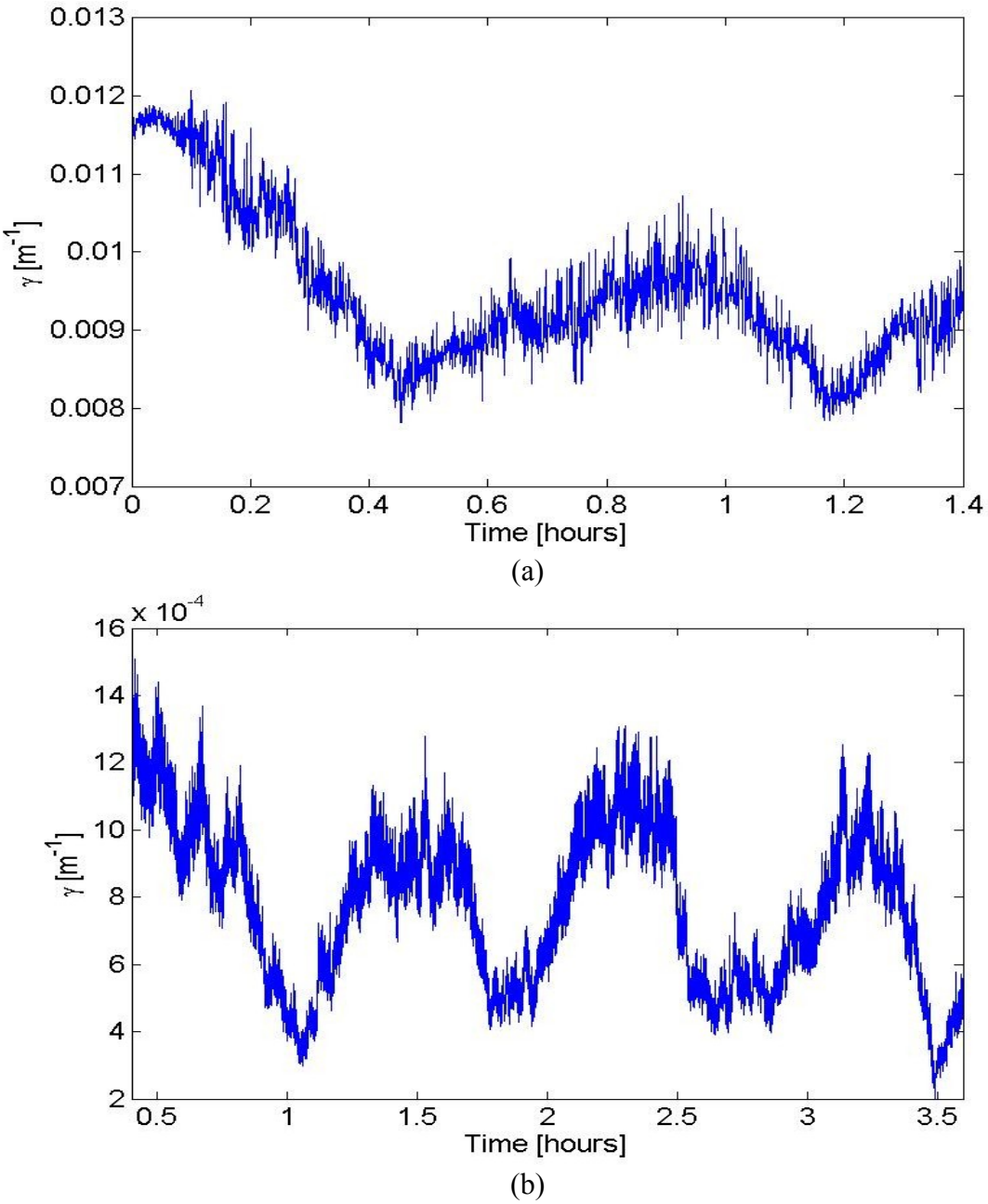


**Figure 5.7.** Time series of the depolarization rate, $\gamma$, for two turbulent strengths corresponding to *Ra* of (a) $4.5\times10^{8}$ and (b) $3.3\times10^{9}$.

## Chapter 6: Conclusions and Future Directions

The primary objective of the work presented here was to quantify the effects of turbulent near-forward scattering on depolarization of an initially polarized beam. In order to investigate this objective, measurements were made on a controlled turbulent flow in a Rayleigh-Bénard convective tank. Thus, the first half of the work consisted in characterizing the turbulent flow within the convective tank. For this purpose, Particle Image Velocimetry and profiling thermistors were employed to detail the large scale features of the flow, and characterize the universal small scales of the turbulent flow through determination of the turbulent kinetic energy dissipation (TKED) rate, and turbulent thermal dissipation (TD) rate. After characterizing the turbulent flow within the convective tank, the second half of the work focused on investigating the effects of turbulent near-forward scattering on depolarization, and thus employed a polarized diffractometer setup to observe the polarized near-forward scattering from the turbulent flow.

To characterize the turbulence within the convective cell, Particle Image Velocimetry was used to obtain the velocity, rms velocities, and skewness fields of the flow, depicting the quieter, low-velocity core near the tank center and higher velocity regions near the tank boundaries. With increasing turbulent strength, the higher velocity regions become more concentrated near the tank boundaries, with the quieter core dominating more of the bulk region, consistent with observations of Xia *et al*. (2003). The rms velocities demonstrated the relative local isotropy of the velocity flow fields, important for obtaining the dissipation rates of the flow. The PIV velocity fields were then used to compute the turbulent kinetic energy dissipation (TKED) rates over the

range of observed turbulent strengths, showing an increase from $10^{-9}$ to $10^{-7}$ $m^2s^{-3}$ over the range of Rayleigh numbers observed in the tank $2\times10^8 < Ra < 3\times10^9$. Profiling thermistors were then employed to measure the temperature fluctuations across a horizontal transect of the tank. From these temperature fluctuations, the one-dimensional thermal gradient spectra were obtained. In order to approximate the temperature dissipation rate, these dissipation spectra were fit with the theoretical Batchelor spectra, and integrated to obtain the TD rates characterizing the flow: $10^{-9}$ $^oC^2s^{-1}$ for lower *Ra* ($2\times10^8$), and increasing to $10^{-4}$ $^oC^2s^{-1}$ for Ra = $3\times10^9$. From the Batchelor fits, estimates of the TKED rate were also made to compare with those obtained from PIV measurements. The two sets of estimates were in good agreement, with the thermistor measurements lying within one standard deviation of the PIV measurements for all but the weakest turbulent strength. The set of measurements presented here provide a subset of the TKED and TD rates observed in the ocean, characterized by $10^{-10} < \varepsilon < 10^{-5}$ $m^2s^{-3}$ (Anis and Moum 1995, Thorpe *et al*. 2003), and $10^{-10} < \chi_\theta < 10^{-4}$ $^oC^2s^{-1}$ (Bogucki *et al.* 2007).

Having characterized the flow within the convective cell, observations were made of the depolarization rates over a range of characterized turbulent strengths. Interestingly, the depolarization rates demonstrated an inverse dependence on the turbulent strength, and a correspondingly inverse dependence on the smallest scale parameters of the flow. These are exciting results in terms of potential applications for deducing information about the small scale features of a flow from optical observations. The observed depolarization rates are also consistent with those obtained from polarized

lidar measurements in Churnside (2008). These results suggest that the depolarization of the near-forward scattered light by turbulence may be a significant factor in measuring the depolarization rate with a polarization-sensitive lidar. This is important because it suggests that optical measurements, such as *in situ* optical profilers or remote sensing instruments, may be useful in gaining information about the small scale structure of a scattering medium, lending new tools and methods for investigations of turbulence. In the case of lidar, this application could prove useful for providing non-invasive investigations of turbulence.

While these results suggest a strong importance of depolarization from multiple near-forward scattering that could affect oceanic optical measurements, further direct comparison is needed. It would be interesting to simultaneously gather polarimetric remote sensing and turbulent characterization measurements from the surface waters of the ocean to further confirm this relationship and to further investigate what information the polarimetric return may carry regarding the small scale features of the flow at the ocean surface.

**References**


Anis, A. and J. Moum., Surface wave-turbulence interactions. Scaling ε(z) near the sea surface. *Journal of Physical Oceanogr*aphy, 25, 2025-2045 (1995).

Asano, S. and M. Sato., Light scattering by randomly oriented spheroidal particles. *Applied Optics,* 19, 962-974 (1980).

Baldi, S. and M. Yianneskis., On the direct measurement of turbulence energy dissipation in stirred vessels with PIV. *Industrial and Engineering Chemical Research,* 42, 7006-6016 (2003).

Berthon, J. -F.., E. Shybanov, M. E. G. Lee, and G. Zibordi., Measurements and modeling of the volume scattering function in the coastal northern Adriatic Sea. *Applied Optics,* Vol. 46, No. 22, 5189-5203 (2007).

Bogucki, D. J., J. A. Domaradzki, C. Anderson, H. W. Wijesekera, R. V. Zaneveld, and C. Moore., Optical measurement of rates of dissipation of temperature variance due to oceanic turbulence. *Optics Express,* 15, 7224-7230 (2007).

Bogucki, D. J., J. A. Domaradzki, R. E. Ecke, and C. R. Truman., Light scattering on oceanic turbulence. *Applied Optics,* 43, 5662-5668 (2004).

Bogucki, D. J., J. A. Domaradzki, D. Stramski, and J. R. Zaneveld., Comparison of near-forward light scattering on oceanic turbulence and particles. *Applied Optics,* 37, 4669-4677 (1998).

Bogucki, D. J., J. Piskozub, M. -E. Carr, and G. D. Spiers., Monte Carlo simulation of propagation of a short light beam through turbulent oceanic flow. *Optics Express,* 15, 13988-13996 (2007).

Bohren, C. F. and D. R. Huffman., *Absorption and Scattering of Light by Small Particles*. Wiley*,* (1983).

Churnside, J. H., Polarization effects on oceanographic lidar. *Optics Express,* 16, 1196-1207 (2008).

Daya, Z. A., and R. E. Ecke., Does turbulent convection feel the shape of the container? *Physical Review Letters,* Vol. 87, No. 18, 29 Oct (2001).

Deardorff, J. W., and G. E. Willis., Investigation of turbulent thermal convection between horizontal plates. *Journal of Fluid Mechanics,* Vol. 28, Part 4, 675-704 (1967).

Dillon, T. M. and D. R. Caldwell., The Batchelor spectrum and dissipation in the upper ocean. *Journal of Geophysical Research*, Vol. 85, No. C4, 1910-1916 (1980).

Domaradzki, J. A. and R. W. Metcalfe., Direct numerical simulations of the effects of shear on turbulent Rayleigh-Bénard convection. *Journal of Fluid Mechanics,* 193, 499-531 (1988).

Doron, P., L. Bertuccioli, J. Katz, and T. R. Osborn., Turbulence characteristics and dissipation estimates in the coastal ocean bottom boundary layer from PIV data. *Journal of Physical Oceanography*, 31, 2108-2134 (2001).

Fincham, A. M. and G. R. Spedding., Low cost, high resolution DPIV for measurement of turbulent fluid flow. *Experiments in Fluids,* 23, 449-462 (1997).

Gregg, M. C., Uncertainties and limitations in measuring ε and $\chi_T$. *Journal of Atmospheric and Oceanic Technology*, Vol. 16, 1483-1490 (1999).

Grossman, S. and D. Lohse., Thermal convection for large Prandtl numbers. *Physical Review Letters*, 86, 15, 3316 (2001).

He, X., Tong, P., and K.-Q Xia., Measured thermal dissipation field in turbulent Rayleigh Bénard convection. *Physical Review Letters*, 98,14, 144501 (2007).

Helland, K. N., Atta, C. W. V., and G. R. Stegen., Spectral energy transfer in high Reynolds number turbulence. *Journal of Fluid Mech*anics, 79, Part 2, 337-359 (1977).

Hielscher, A., A. Eick, J. Mourant, D. Shen, J. Freyer, and I. Bigio., Diffuse backscattering Mueller matrices of highly scattering media. *Optics Express,* 1, 441-453 (1997).

Hodara, H., Laser wave propagation through the atmosphere. *Proceedings of the IEEE,* 54, 368-375 (1966).

Hu, C., G. W. Kattawar, M. E. Parkin, and P. Herb., Symmetry theorems on the forward and backward scattering Mueller matrices for light scattering from a nonspherical dielectric scatterer. *Applied Optics,* 26, 4159-4173 (1987).

Hussain, A. K. M. F., Coherent structures – reality and myth. *Physics of Fluids,* 26, 10, October (1983).

Jaffe, J. S., Monte Carlo modeling of underwater-image formation: validity of the linear and small-angle approximations. *Applied Optics,* 34, 5413-5421 (1995).

Jerlov, N. G., *Optical Oceanography*. Elsevier, Amsterdam (1968).

Kármán, T. von, Progress in the statistical theory of turbulence. *Journal of Marine Research,* 7, 252 (1948).

Kim, A. D. and M. Moscoso., Influence of the refractive index on the depolarization of multiply scattered waves. *Physical Review E,* 64, 026612-1-026612-5 (2001).

Krishnamurti, R., On the transition to turbulent convection. Part 1. The transition from two- to three-dimensional flow. *Journal of Fluid Mechanics,* Vol. 42, Part 2, 295-307 (1970).

Kundu, P. K. and I. M. Cohen., *Fluid Mechanics*. Elsevier*,* Amsterdam (1987).

Lueck, R. G., F. Wolk, and H. Yamazaki., Oceanic velocity microstructure measurements in the 20$^{th}$ century. *Journal of Oceanography,* 58,153-174 (2002).

Luketina, D. A., and J. Imberger., Determining turbulent kinetic energy dissipation from Batchelor curve fitting. *Journal of Atmospheric and Oceanic Technology,* 18, 100-104 (2001).

Mobley, C. D. *Light and Water: Radiative transfer in natural waters*. Academic Press, New York (1994).

Morel, A., and H. Loisel., Apparent optical properties of oceanic water: dependence on the molecular scattering contribution. *Applied Optics*, Vol. 37, No. 21 (1998).

Nikolaenko, A. and G. Ahlers., Nusselt number measurements for turbulent Rayleigh Bénard convection. *Physical Review Letters*, 91, 8, 084501 (2003).

Pao, Y. H., Structure of turbulent velocity and scalar fields at large wavenumbers. *Physics of Fluids*, 8, 1063 (1965).

Petzold, T.J., Volume scattering functions for selected ocean waters. UC San Diego: Scripps Institution of Oceanography (1972).

Rojas-Ochoa, L. F., D. Lacoste, R. Lenke, P. Schurtenberger, and F. Scheffold., Depolarization of backscattered linearly polarized light. *Journal of the Optical Society of America A,* 21, 1799-1804 (2004).

Saarenrinne, P. and M. Piirto., Turbulent kinetic energy dissipation rate estimation from PIV velocity vector fields. *Experiments in Fluids [Suppl.]*, S300-S307 (2000).

Saarenrinne, P., M. Piirto, and H. Eloranta., Experiences of turbulence measurement with PIV. *Measurement Science and Technology*, 12, 1904-1910 (2001).

Spinrad, R. W. and J. Brown., Effects of asphericity on single-particle polarized light scattering. *Applied Opt*ics, 32, 6151-6158 (1993).

Strohbehn, J. W. and S. F. Clifford., Polarization and angle-of-arrival fluctuations for a plane wave propagated through a turbulent medium. *IEEE Transactions on Antennas and Propagation*, Vol. AP-15, No. 3, May (1967).

Strohbehn, J. W., Line-of-sight wave propagation through the turbulent atmosphere. *Proceedings of the IEEE,* 56, 1301-1318 (1968).

Styles, Richard., Laboratory evaluation of the LISST in a stratified fluid. *Marine Geology,* 227, 151-162 (2006).

Sullivan, J. M., M. S. Twardowski, P. L. Donaghay, and S. A. Freeman., Use of optical scattering to discriminate particle types in coastal waters. *Applied Optics*, Vol. 44, No. 9, 1667-1680 (2005).

Tennekes, H. and J. L. Lumley., *A First Course in Turbulence*. The MIT Press, Cambridge (1972).

Thorpe, S. A., Recent developments in the study of ocean turbulence. *Annual Reviews of Earth and Planetary Sciences,* 32, 91-109 (2004).

Thorpe, S. A., T. R. Osborn, J. F. E. Jackson, A. J. Hall, R. G. Lueck., Measurements of turbulence in the upper-ocean mixing layer using Autosub. *Journal of Physical Oceanography,* 33, 122-145 (2003).

Tritton, D. J., *Physical Fluid Dynamics.* Oxford University Press, New York, 359-377 (1988).

Wang, J., and K. Q. Xia., Spatial variations of the mean and statistical quantities in the thermal boundary layers of turbulent convection. *European Physical Journal B*, 32 127-136 (2003).

Xi, H. -D., and K. –Q. Xia., Flow mode transitions in turbulent thermal convection. *Physics of Fluids,* 20**,** 055104 (2008).

Xia, K. –Q., C. Sun, and S. –Q. Zhou., Particle image velocimetry measurement of the velocity field in turbulent thermal convection. *Physical Review E,* 68, 066303 (2003).

Yang, P., H. Wei, G. W. Kattawar, Y. X. Hu, D. M. Winker, C. A. Hostetler, and B. A. Baum., Sensitivity of the backscattering Mueller matrix to particle shape and thermodynamic phase. *Applied Optics* 42, 4389-4395 (2003).

Zhou, Q., C. Sun, and K. -Q. Xia., Experimental investigation of homogeneity, isotropy, and circulation of the velocity field in buoyancy-driven turbulence. *Journal of Fluid Mech*anics 598, 361-372 (2008).

Zocchi, G., E. Moses, and A. Libchaber., Coherent structures in turbulent convection, an experimental study. *Physics A* 166 387-407 (1990).

## VITA

Sarah Woods was born in Franktown, Colorado in July 1982 to Harry and Rose Marie Woods. After attending primary and secondary school in Franktown and Parker, Colorado, she graduated high school, Salutatorian, in 2000. In 2004, she graduated with honors from Colorado State University, receiving her Bachelor's of Science degree in Electrical Engineering, with a concentration in Optoelectronics, and a minor in Mathematics. During her undergraduate studies, she was awarded College of Engineering Sophomore of the Year Award, and was recognized for her service and achievements by Tau Beta Pi, Eta Kappa Nu, and Golden Key honor societies, of which she actively participated and held leadership roles. She also served as a Spanish and mathematics tutor and a veterinary hospital equine aid.

In Fall 2004 she began graduate study at the Rosenstiel School of Marine and Atmospheric Science (RSMAS) at the University of Miami in Southern Florida. She was awarded a High Pass on her comprehensive exam, allowing her to bypass a Master's degree, and succeed in defending her dissertation for Doctor of Philosophy in Applied Marine Physics in December 2009. During her tenure at RSMAS, she served on the Marine Science Graduate Student Organization, the Student Travel Fund, and was recognized for her service and achievements by Alpha Epsilon Lambda honor society.